TOWARDS SINGLE-MOLECULE NANOMECHANICAL MASS SPECTROMETRY

Thesis by
Mehmet Selim Hanay

In Partial Fulfillment of the Requirements
for the Degree of
Doctor of Philosophy

California Institute of Technology
Pasadena, California
2011
(Defended June 1, 2011)

Acknowledgement

This thesis was made possible with the help of numerous people. First and foremost I would like to thank my thesis advisor Prof. Michael Roukes for his continuous support during my graduate studies. Often times I would go to his office demoralized by the challenges of the experiment, and leave his office with hope, ideas and high motivation. I also had the good fortune of learning many non-academic skills working with him and his group.

I want to thank Akshay Naik for practically teaching me the profession of experimental physics. Without him, much of the work in this thesis would not have occurred. He has always led by example during our work together and the shortcomings presented in this thesis should be attributed to my lack of learning. I want to thank Wayne Hiebert, a truly kind person, for his mentoring during the early phase of my studies in the Roukes Group. We learnt many things from his design of the setup for the first generation experiments. I feel lucky to have worked with two talented graduate students while in the Roukes group, Caryn Bullard and Scott Kelber. I am also indebted to Caryn for her help with the language.

I have worked and exchanged ideas with many other people at Caltech: Igor Bargatin, Derrick Chi, Philip Feng, Ed Myers, Matt LaHaye, Junho Suh, Rassul Karabalin, Matt Matheny, Benjamin Gudlewski, Steve Stryker, Woochang Lee, Prof. John Sader, Jie Xiang, Xinchang Zhang, Blake Axelrod, Warren Fon, Jessica Arlett, Guillermo Villanueva and the rest of the Roukes group and alumni during these years. Furthermore, I want to thank the KNI staff especially Bophan Chhim and Melissa Melendes for their support in our fabrication projects. On the logistics side, I want to thank Su Naing, Loly Ekmekjian, Mary Sikora, Exie-Marie Leagons and Sandra Durkee for enabling us to focus on science better. I want to thank Prof. Hideo Mabuchi and Michael Armen for my first research experience at Caltech.

I enjoyed our collaboration with CEA LETI and I would like to thank Phillipe Andreucci, Sébastien Hentz, Eric Colinet, Laurent Duraffourg and Pierre Puget. I especially thank Sébastien for his

thorough investigation of the multimode mass error work, Eric for his enthusiasm and many useful techniques he contributed to the overall effort, and Laurent for many useful discussions we had during the LETI-Caltech workshops. I also acknowledge the contribution of Kamil Ekinci in the early stages of this collaboration, and his various suggestions during the early NEMS MS meetings.

I also acknowledge the help of Prof. Jack Beauchamp and Mona Shahghouli with the electrospray ionization. I appreciated the feedback I got from my candidacy committee: Prof. Scott Fraser, Prof. Jack Beauchamp and Prof. Gil Refael. I am also indebted to my thesis committee members -Prof. James Eisentein, Prof. Michael Cross and Prof. Scott Fraser- for their time.

Although PhD is an advanced stage in academic training, it is built upon a foundation acquired at previous institutions. In this respect, I want to acknowledge my previous mentors and teachers, especially Prof. Burak Erman, Prof. Ali Alpar, Prof. Ataç İmamoğlu, Prof. Yusuf Leblebici, Prof. Albert Erkip, Prof. Uğur Sezerman, Prof. Hüseyin İşçi, Prof. Cihangir Tanyeli, Prof. Osman Yavuz Ataman, Prof. Özdemir Doğan, Prof. Ali Usanmaz, Prof. Mustafa Demirplak, other numerous professors at Sabanci University and METU Chemistry Department, Meral Aytekin, Fevzi Konca, Cahit Arpacık, Celal Arpacık and Nezahat Yarol. I also want to thank Sabanci and Ford Foundations for their support during my education.

I would like to thank my close friends and my girlfriend at Caltech for the bright things they brought into my life. Finally, I thank to my family for their unconditional support through these years – especially considering the fact that I attended grad school against their strong, and possibly wise, advice.

Abstract

We present an initial attempt to perform mass spectrometry (MS) of single proteins and gold nanoparticles with nanoelectromechanical systems (NEMS). Mass spectrometry, the identification of molecules based on their masses, is one of the most important techniques in proteomics research currently. NEMS devices, with their exquisite sensitivities, low costs, and abilities to detect neutral molecules, offers a promising paradigm for performing mass spectrometry.

In our first-generation experiments, protein molecules, and gold nanoparticles were ionized by electrospray ionization (ESI) and transported to a NEMS chip, through a differential vacuum system, by hexapolar ion guides. NEMS was transduced by magnetomotive technique and the fundamental mode of the flexural resonance was monitored. Species landing on the NEMS are weighted through the change in the frequency of the resonator. Two protein species (66 kDa and 200 kDa) and 5 nm gold nanoparticles were analyzed with this technique, with mass resolution level of 15 kDa.

A method to remove the position dependency of the frequency shift was developed employing two different modes of a nanomechanical beam. The uncertainties of mass and position values are calculated as a function of the frequency noise of the first and second modes of the beam.

In our second-generation experiments, the first and second flexural modes of a doubly-clamped beam were tracked in real time. Nanoparticles and biospecies are again produced through ESI and transported through ion optics. The adsorption of 10 nm GNPs and IgM protein (950 kDa) were observed. Mass values for these events are obtained with the multimode analysis technique and shown to be consistent with the expected values.

Table of Contents

List of Illustrations

List of Tables

List of Abbreviations

ag	…..	Attogram, i.e. 10^{-18} g
Da	…..	Dalton, unit of mass. 1 Da=1/12^{th} of the mass of a C^{12} atom.
DCB	…..	Doubly-Clamped Beam
ESI	…..	Electrospray Ionization
LNA	…..	Low-Noise Amplifier
NEMS	…..	Nanoelectromechanical System(s)
MS	…..	Mass Spectrometry
PDF	…..	Probability Density Function
PLL	…..	Phase-Locked Loop (circuitry to track the frequency of NEMS)
yg	…..	Yoctogram, i.e., 10^{-24} g
zg	…..	Zeptogram, i.e., 10^{-21} g

CHAPTER 1:

INTRODUCTION AND BACKGROUND

1.1 Motivation in Short

This thesis describes an initial attempt to weigh and identify single biomolecules, by monitoring their effect on the mechanical properties of nanoscale devices. On the one hand, techniques to identify biomolecules by measuring their masses —*Mass Spectrometry*— plays an indispensable role as an analytical tool for molecular-biology research, especially in proteomics and metabolomics. On the other hand, nanoscale devices offer unprecedented sensitivities for various types of measurements. Thus, we wanted to utilize nanoscale sensors to develop a novel analytical tool —the nanomechanical mass spectrometer— for biological research. To further explain our motivation, we will briefly describe the main themes of our work: mass spectrometry and nano-electromechanical systems (NEMS).

1.2 Mass Spectrometry

Mass spectrometry is the generic name for the techniques used to identify molecules by measuring their molecular masses. Almost always, these techniques measure the mass-to-charge ratio of an ionized species. Once this ratio is measured, the mass can be inferred, as there are certain ways to determine the charge on the molecules. Unlike this kind of conventional mass spectrometry, NEMS based mass spectrometry can measure the mass of the molecule by mechanical means without any need for ionization. Some of the conventional mass spectrometry techniques are described in section (1.3).

To put the mass spectrometry into perspective, we need to consider the current state of molecular biology. It has been a decade since the human genome project was successfully completed. Today, it is almost a standard procedure to determine the genetic code of an organism. The advances in genomics have been possible because of the self-replication feature of nucleic acids. This property of self-replication was capitalized after the discovery of enzymatic procedures and the development of high-throughput analytical tools. With these techniques, miniscule amount of genetic material can be amplified several orders of magnitude in a relatively short time. Thus one important class of biomolecules, nucleic acids, can now be identified and sequenced efficiently.

Although genetic material contains literally all the information required for life, it is not the end of the story of biology. The biochemical reactions coded in the genes are carried out by proteins. Even though proteins are synthesized from nucleic acids, it is still important to identify proteins directly. Firstly, genes contain static information, i.e., the possible types of proteins. But they do not reveal the amount of each protein as conditions change. They do not describe the interactions among proteins. Furthermore, proteins can be modified after they are synthesized from nucleic acids, and these modifications affect the function of a protein significantly. Summing up, genes contain all the information but not all of the knowledge for life, as we cannot understand their content without invoking the proteins.

As a result, high-throughput techniques for protein identification are critical for biology research [1]. Unlike nucleic acids, proteins do not have the capability to self-replicate. Furthermore, they are more diverse in their structure and building blocks. Therefore

developing the technology to identify proteins is a more challenging task. Currently, the forerunner of the techniques for protein identification is mass spectrometry.

Proteins are composed of subunits called amino-acids. There are twenty different types of natural amino-acids, each one with a different molecular mass. Thus, when the mass of an amino acid is known, it can be identified. When a protein containing hundreds of amino acids needs to be analyzed, it is fragmented into smaller pieces – until the structure of each segment can be identified uniquely. Combining the information from each of these constituents, the overall structure of a protein can be deduced. Incidentally, this technique is called protein fingerprinting or bottom-up mass spectrometry. Alternatively, one can measure the total mass of a protein to identify it from a library of known proteins. This approach is called top-down mass spectrometry. Our experiments fall into the latter category.

Mass spectrometry is a different concept than mass sensing. *Spectrometry* indicates the identification of a species or the discrimination of a species from others. Mass sensing, however, deals with the amount of mass without any concern about the chemical identification or composition of the material. Most of the mass measurements in micromechanics or nanomechanics are mass sensing, rather than mass spectrometry. We believe our work is one of the pioneers for the mass spectrometry with mechanical structures.

1.3 Brief Description of Conventional† Mass Spectrometry

Since we aim to develop a novel mass spectrometer, it would be instructive to describe the alternative techniques, i.e. conventional mass spectrometry. The term *conventional mass spectrometry* refers to the set of techniques which infer the mass of charged molecules by measuring their mass-to-charge (m/z) ratios using electromagnetic means. We will briefly summarize the most prevalent methods. More information and historical perspective can be found in the excellent references such as [2],[3] . Comparison of these methods with NEMS MS can be found in the final chapter.

In **Time-of-Flight** Mass Spectrometry (TOF MS), the ions are accelerated under a potential difference and their transit time along a certain distance is measured. From this measurement of flight-time, one can calculate the m/z ratio of the ions. This method is a relatively high throughput, high resolution method.

In **Quadrupole Mass Spectrometry** (Q-MS), ions are dispatched into a flight tube surrounded by four metallic rods. RF and DC voltages are applied to these rods. When the frequency and the amplitudes of these voltages are tuned carefully, only the ions with a certain m/z value can be transmitted, as the others will not sustain stable trajectories along the path. A detector at the end of the flight tube measures the current due to the ions with selected m/z value. By changing the electrical parameters, transmitted m/z value can be swept and the spectrum of the species can be obtained. This is a high throughput, low resolution technique.

† Although the word, *conventional*, hints at stagnancy, the truth is mass spectrometry is a very active area of research. We have been using this word with its meaning closer to *commonplace* rather than *orthodox*.

In **Fourier Transform Ion Cyclotron Resonance Mass Spectrometry** (FTICR MS), ions in a constant magnetic field are excited to circular motion by oscillatory electric fields. Each ion circles at a certain frequency, the cyclotron frequency, based on its m/z value. The motion of the ionic cloud induces a voltage on the readout electrodes. This induced voltage can be decomposed into its Fourier components to determine the cyclotron frequencies and hence the m/z values of the ions composing the sample. This is a low throughput, very high resolution technique.

1.4 Nano-Electromechanical Systems (NEMS)

Nanoelectromechanical systems (NEMS) are electrically controllable mechanical structures with at least one dimension smaller than one micrometer.

First created in 1995 [4], these systems have been employed for basic research in the quantum properties of mechanical objects [5, 6] and nonlinear science [7, 8]. On the more applied side, nanomechanical systems have been used as mass sensors [9-11] gas sensors [12] and biosensors [13].

Our work focused on the flexural, resonant motion of doubly-clamped beams or cantilevers[‡]. This motion can be described as a harmonic oscillator for small displacements. Like all harmonic oscillators, NEMS dynamics has both potential energy and kinetic energy components. The potential energy component originates from the elastodynamic response of the mechanical beam, i.e. the beam flexure. The kinetic energy arises from the

[‡]We want to create on-chip components as they can be multiplexed. Hence freely moving or rotating objects, like microparticles on optical tweezers, were out of question. Thus our devices are always clamped on one side. The mechanical motion at the nanoscale becomes tiny and hard to detect; that is why we strive to work on resonance, where the motion and readout signal is maximal. Flexural motion can be actuated through very simple device geometries; hence we worked with flexural motion. It may be possible to find a better nanomechanical system to perform mass spectrometry: maybe we have not thought hard enough yet.

motion of the beam. The scaling factor for the kinetic energy, *the effective mass*, is a certain fraction of the physical mass of the beam. The relative strengths of the potential and kinetic energy components determine the resonance frequency of NEMS vibrations. In our experiments, this resonance frequency is measured continuously. When a particle lands on NEMS; the effective mass of the resonator increases by the extra mass of the particle and the resonance frequency changes abruptly. We detect this change in frequency and deduce the mass of the particle based on the amount of the frequency change.

If we consider the three properties defining NEMS, we can see why it is situated well for mass spectrometry purposes:

1) *Mechanical structure:* As described above, the essence of mass sensing depends on the measurement of the resonance frequency of the mechanical structure. Furthermore, this mechanical origin distinguishes NEMS based sensing from other techniques based on the *m/z* measurements.
2) *One dimension smaller than 1μm*: Our signal scales as the ratio of the added mass to the mass of the beam. To maximize this signal we need a light structure. Hence the smaller the mechanical structure, the larger the effect (of course, we assume the measurement noise does not degrade by going to smaller devices.) That is why we really need to go beyond microelectromechanical systems (MEMS) which have orders of magnitude larger effective masses compared to NEMS.
3) *Electrical Control*: A single NEMS device is a very small entity by itself. It has a very small cross-section to capture proteins. For practical applications many NEMS resonators, each individually controlled, should be used in the same chip. By using

the tools developed in microelectronics, we can integrate the control system with NEMS. This way, NEMS arrays can be controlled, increasing the capture efficiency of the technique and decreasing the marginal cost of production.

1.5 Motivation in Detail

Like most scientific work, our primary motivation to work on NEMS mass spectrometry was curiosity. An experiment like this was never done before. A single molecule would land on a mechanical structure, the mass of the structure would change abruptly, which would change the resonance frequency of motion; and at the outside world, we would detect this process as a frequency jump and obtain information about the mass of the protein. Not all the steps of this process have been fully understood, and it was not clear at the onset that this experiment would work – although in hindsight there does not seem to be any physical reason. It is still a pleasure for me, and for my collaborators, to watch the NEMS frequency in real-time with the anticipation of a sudden jump event, signaling the arrival of a protein molecule.

Our second and more practical motivation was to initiate a project that may result in the development of a useful tool for biological and environmental applications. The conventional mass spectrometry field is already a very developed enterprise with stunning achievements; however the basic principle of our method is truly different than the ones already developed. Therefore we believe that our paradigm could enhance and compliment current techniques. More specifically NEMS-based MS offers, or will offer, the following benefits:

1) Mass measurement of neutral species

2) Higher dynamic range for mass measurements
3) Lower costs
4) Higher throughput.

These practical considerations will be more thoroughly discussed in the last chapter of the thesis, along with a description of ultimate NEMS MS system as envisioned today. Suffice it to say that, performing molecular mass measurements in a novel way seemed to be a worthwhile effort for doing basic science and for developing technology.

1.6 History of Nanomechanical Mass Sensing

The efforts in our group to weight ultra-small amount of matter started with the ultrahigh vacuum system built by Kamil Ekinci. In a paper published in 2004 [9], they measured an ensemble of gold atoms with a resolution of 2.5 attograms (i.e. 2.5 10^{-18}g). In this experiment, the flux of gold atoms was shuttered to differentiate the effect of mass accretion. Mass flux was independently calibrated with a quartz crystal microbalance positioned closer to the source. This work suggested the possibility of weighting individual molecules.

Noise processes in nanomechanical resonators were extensively investigated in 2002 by Cleland and Roukes, [14]. The formalism presented in the paper was applied to mass sensing applications in a paper by Ekinci, Yang and Roukes [15] in 2004. In this theoretical paper, it was shown that the intrinsic noise processes in NEMS would allow the detection the mass of a single Hydrogen atom (defined as 1 Dalton = 1.66 10^{-24}g). In

recent years however we seem to be trailing behind this theoretical expectation and further work must be done to understand the fundamental limits on mass sensitivity.

Mass sensitivity performance was increased even further by Jack Yang *et. al*, [11] in a paper published in 2006. In this experiment, a gas nozzle was used to deliver a pulsed beam of N_2 molecules or Xe atoms, and operational mass sensitivity of 20 zeptogram was obtained (1 zeptogram=10^{-21} gram). This was two orders of magnitude advancement compared to the work published two years before [9] , and it came about through the use of smaller devices.

Within this setting, Dr. Wayne Hiebert joined the group around 2003 to set up a system to deliver the protein molecules. He designed the differential pumping system, together with the electrospray ionization system to produce protein ions and hexapolar ion guide to transport the ions. When I joined in the group in January 2005, the initial designs were completed and we started to assemble the system.

1.7 Recent Literature on NEMS-Based Mass Sensing

We want to mention two areas of research in recent years, as they relate to our research. One area of progress was the extraction of the mass information from multiple mechanical modes to nullify the effect of particle's position on the beam. When I started to work on the NEMS MS, position-dependency was still an open problem and we came up with the idea of multimode mass detection in mid-2005 during a discussion after one of the Ph/EE 118 classes. The idea was recorded in the lab notebook, in e-mail communications and as a patent application. (The patent application was received by the

Caltech Technology Transfer office, but was not pursued further. However, in 2008 we issued a patent on several ideas related to NEMS MS including the multimode mass detection [16].)

While developing the ideas of multimode mass detection, we were concurrently working on the experimental effort to detect individual protein molecules, and we viewed the multimode technique as one of the components of the overall effort. Consequently we focused our efforts to solve the more immediate technical problems, rather than to publish a quick paper with multimode detection. A few years after we conceived the idea, a group in Denmark developed a similar multimode detection scheme [17]. They have performed experiments with MEMS cantilevers, using four or more modes sequentially, usually measuring microparticles weighting about femtograms (10^{-15} g). They showed a proof of principle in a different setting and at a much heavier scale than we work (10-100 zg i.e. 10^{-20}-10^{-19}). Of course, the physics should be the same at every scale. For the practical goal of identification of biomolecules however, one needs to work below attogram (10^{-18} g) levels.

Another thrust of progress has been on using carbon nanotubes to measure very small masses [18], [19], [20]. Here the extreme lightness of carbon nanotubes offers a breakthrough in mass sensitivity. However in these experiments, it is very difficult to distinguish individual mass accretion events. For instance [19] claims to detect individual gold atoms. However, the method relies on depositing many identical atoms for a period of time. After enough statistics from identical atoms are obtained, a Shot-noise analysis is performed to figure out the unit of mass accretion. Obviously, this mode of analysis

cannot be extended to a real world sample, which includes many different types of molecules.

1.8 Overview of the Following Chapters

In chapter 2, we will describe our first experiment to weigh [§] individual protein molecules. In this experiment, we used only the fundamental mode of a doubly-clamped beam. The frequency shift for each protein adsorption events depends not only on the mass of the protein, but also on where it is adsorbed along the length of the beam. Mass information is obtained by collecting many events and processing them statistically to get rid of the effect of landing position.

In chapter 3, we tackle the problem of removing the position dependency by using the first two flexural mechanical modes of a doubly-clamped beam. In this section, we also show how the frequency instability is translated into uncertainties for mass and position values.

Motivated by this framework, in chapter 4 we present the NEMS MS experiment using two modes of a doubly-clamped beam. Here, we also report a more compact setup compared to the first experiment. We show some preliminary data, partially suggesting that the multimode detection works.

[§] Although the word *weigh* implies the measurement of gravitational force on an object, we actually measure the inertial mass. Throughout the thesis, the verb *to weight* will be used as an acronym for "to measure the inertial mass", for brevity and the lack of a better word.

In the concluding chapter, chapter 5, we evaluate the state of NEMS MS, identify the shortcomings, describe the ultimate systems we strive to achieve, and compare the current and possible versions with that of conventional mass spectrometry.

We also include many appendices. Due to the nature of our experiments, we had to cover many side tracks and we include some of these in these appendices, so that they do not interfere with the flow of the main ideas.

CHAPTER 2:

SINGLE-MODE NEMS MASS SPECTROMETRY**

2.1 Introduction

In 2004, our group increased the mass sensitivity of nano resonators to zeptogram levels [9] [11], a milestone suggesting the feasibility of weighing individual protein molecules. We wanted to actualize this prospect of weighing proteins and prove that individual protein molecules can be detected and measured with nanomechanical systems.

In this chapter, we will review the physics of NEMS and the mechanism of mass sensing. We will use the Euler-Bernoulli beam equation to obtain NEMS dynamic and then determine how mass landing on the device changes the resonant frequency of the device. Later, we will describe the experimental setup in detail. We will mention how we create and transport the protein ions. Later, we will present the frequency jump data obtained from proteins and nanoparticles and analyze this data using statistical methods.

2.2 Flexural Vibrations of a NEMS Beam

In this section, we will review the basic equations describing the flexural vibrations of NEMS beams. Our goal is to start from the Euler-Bernoulli beam equation and arrive at the harmonic oscillator model of mechanical modes, a model that enables us to calculate the effect of mass accretion on the resonance frequency. We will extensively use this

** The work presented in this section has been performed with Akshay Naik and Wayne Hiebert. Furthermore, Philip Feng has provided crucial technical assistance.

relationship between mass accretion and resonance frequency in this thesis, so it is important to see how the harmonic oscillator model is derived from the equation of motion.

To summarize the mathematics that will follow: we will first solve the Euler-Bernoulli beam equation using separation of variables and modal expansion, state the orthogonality condition of the modes, project the general equation of motion on a specific mode and obtain the harmonic oscillator description for that mode. Many previous works include this derivation in detail [21, 22]: we include it here for completeness of discussion and consistency of notation.

We will derive the equations of motion for a beam with length **l**, thickness **t**, and width **w** (Figure 1). It is made of a material with density **ρ** and Young's modulus **E**. The motion we want to study is the out-of-plane flexural motion of the beam. Referring to the coordinate system of Figure 1, the beam extends along the x-direction and vibrates along the z-direction.

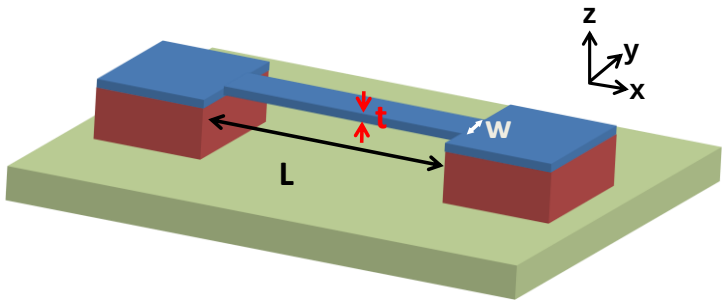

Figure 1: NEMS beam coordinates

$u(x, y, z, t)$ describes the vertical displacement of the point originally located at (x, y, z) on the beam. The vertical displacement of a point depends most strongly on its axial

location along the length of te beam, since the beam is slender[††]. Therefore we can write: $u(x,y,z,t) \approx u(x,t)$. Using $u(x,t)$ as the dynamical variable, the Euler-Bernoulli equation of motion can be written as:

$$EI\frac{\partial^4}{\partial x^4}u(x,t) - T\frac{\partial^2}{\partial x^2}u(x,t) + \rho S\frac{\partial^2 u(x,t)}{\partial t^2} = 0 \qquad (1)$$

Here, the first term describes the bending moment of the beam, and $I \equiv wt^3/12$ denotes the areal moment of inertia of the beam. The second term describes the effect of tension with T representing the axial stress on the beam. The third term is the inertial term and $S \equiv wt$ is the cross-sectional area of the beam.

In our experiments, the bending term dominates the tension term. Hence we will neglect the effect of tension for now, and return to it in the last section of the next chapter. With tension neglected, the equation of motion becomes:

$$EI\frac{\partial^4}{\partial x^4}u(x,t) + \rho S\frac{\partial^2 u(x,t)}{\partial t^2} = 0 \qquad (2)$$

Using separation of variables and modal expansion, we can write a solution for $u(x,t)$ in the following form:

$$u(x,t) = \sum_{n=1} \phi_n(x) q_n(t) \qquad (3)$$

Here, n denotes the mode number,

$\phi_n(x)$ is the mode shape, normalized so that $\max[\phi_n(x)] = 1$.

[††] As the beam has a slender geometry, any transverse variation of the displacement field would result in large amounts of stress, inconsistent with the stress-free boundary conditions. Therefore, we can neglect any weak dependence on transverse coordinates to first order.

The term $q_n(t)$ is the time-dependent solution and contains the amplitude information as well as the temporal dependence.

Inserting this form for the dynamical variable(3), into the equation of motion, (2) yields:

$$EI \sum_{n=1} A_n q_n(t) \frac{\partial^4 \phi_n(x)}{\partial x^4} + \rho S \sum_{n=1} A_n \phi_n \frac{\partial^2 q_n(t)}{\partial t^2} = 0 \tag{4}$$

For each mode n, the equation above can be written as:

$$\frac{EI}{\rho S} \frac{\frac{\partial^4 \phi_n(x)}{\partial x^4}}{\phi_n(x)} = -\frac{1}{q_n(t)} \frac{\partial^2 q_n(t)}{\partial t^2} = cnst. \equiv \omega_n^2 \tag{5}$$

Solving the time dependent part yields:

$$\frac{\partial^2 q_n(t)}{\partial t^2} = -\omega_n^2 q_n(t) \ \rightarrow q_n(t) = A_n \sin(\omega_n t + \theta_n) \tag{6}$$

Now rearranging the the spatial part, we get:

$$\frac{\partial^4 \phi_n(x)}{\partial x^4} = \frac{EI}{\rho S} \omega_n^2 \ \phi_n(x) = \beta_n^4 \phi_n(x) \ \ with \ \ \beta_n^4 \equiv \left(\frac{EI}{\rho S}\right)^{\frac{1}{4}} \sqrt{\omega_n} \tag{7}$$

Finally we obtain the solutions:

$$\phi_n(x) = \gamma_{n1} \cos(\beta_n x) + \gamma_{n2} \sin(\beta_n x) + \gamma_{n3} \cosh(\beta_n x) + \gamma_{n4} \sinh(\beta_n x) \tag{8}$$

The coefficients γ_{ni} are determined by the boundary conditions and the normalization condition: $\max[\phi_n(x)] = 1$. Furthermore, imposing the boundary conditions will yield both the wavelengths (β_n) values, and also the eigenfrequencies (ω_n) through equation (7). The boundary conditions for the doubly-clamped beam (DCB) are that the displacement and its first spatial derivative vanish at the clamping points: $\phi_n(x = 0) = \phi_n(x = \ell) = 0$ and $\phi_n'(x = 0) = \phi_n'(x = \ell) = 0$. The mode-shapes and the wavelengths for the first several modes of the DCB and the cantilever are given in Table 1.

So far we have solved for the eigenfrequencies and mode shapes of the flexural motion in NEMS beams. We have not explicitly shown that the modes thus found are indeed orthogonal to each other. Two modes are orthogonal if the two different mode shapes are multiplied with each other and the product is integrated over the length of the beam, and the integral turns is zero: $\int_{x=0}^{x=\ell} \phi_n(x)\phi_m(x)dx = 0 \; if \; n \neq m$. The algebra of the proof can be found in references like [22] .The proof is lengthy, although it is straightforward.

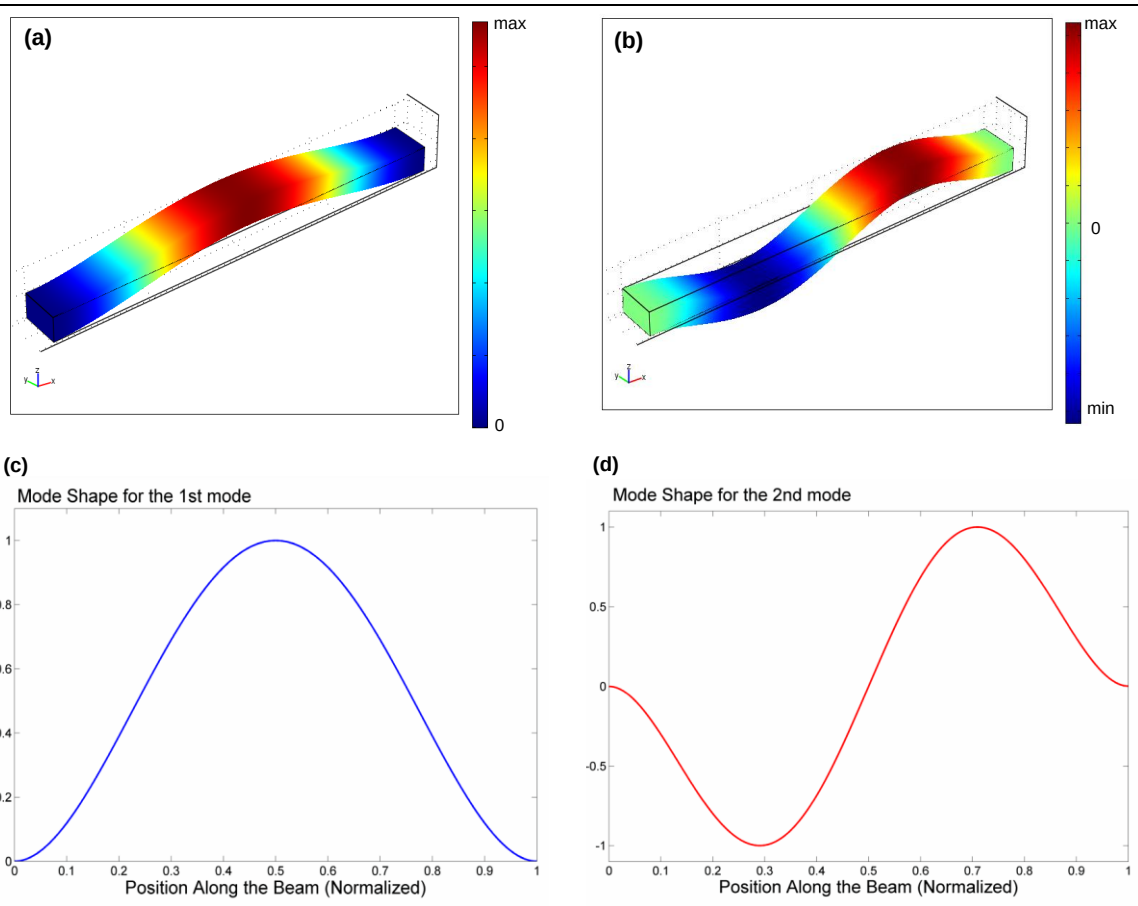

Figure 2: Mode shapes for the first two modes

(a) Mode 1, the colormap is proportional to the vertical displacement
(b) Mode 2, the colormap is proportional to the vertical displacement
(c) The mathematical function describing the first mode
(d) The mathematical function describing the second mode

$\boldsymbol{\phi_n(x) = A_n \times \left[(1-\epsilon_n)[cosh(\beta_n x) - cos(\beta_n x)] + [sin(\beta_n x) - sinh(\beta_n x)]\right]}$			
n, Mode Number	A_n: Norm. Coeff.	ϵ_n	β_n : Wavevector
1	0.6294	$1.780941\ 10^{-2}$	4.7300
2	0.6623	$-7.767082\ 10^{-4}$	7.8532
3	0.6608	$3.355100\ 10^{-5}$	10.9956
4	0.6609	$-1.449896\ 10^{-6}$	14.1372

Table 1: Mode Shapes & Coefficients for the Doubly-Clamped Beam

Harmonic Oscillator Model and Effective Mass

Now we consider a beam excited in a single mode (general case does not change the result below, due the orthogonality of the modes).

$$EI\ q_n(t)\frac{\partial^4\phi_n(x)}{\partial x^4} + \rho S\frac{\partial^2 q_n(t)}{\partial t^2}\phi_n(x) = 0 \qquad (9)$$

Multiplying the above equation with the mode shapes, $\phi_n(x)$ and integrating over the length of the beam yields:

$$EI\ q_n(t)\int_{x=0}^{x=\ell}\phi_n(x)\frac{\partial^4\phi_n(x)}{\partial x^4}dx + \rho S\ddot{q}_n(t)\int_{x=0}^{x=\ell}\phi_n(x)\phi_n(x)dx = 0 \qquad (10)$$

We will perform integration by parts twice on the integrand in the first term:

$$\int_{x=0}^{x=\ell}\phi_n(x)\frac{\partial^4\phi_n(x)}{\partial x^4}dx = \phi_n(x)\frac{\partial^3\phi_n(x)}{\partial x^3}\Big]_{x=0}^{x=\ell} - \int_{x=0}^{x=\ell}\frac{\partial\phi_n(x)}{\partial x}\frac{\partial^3\phi_n(x)}{\partial x^3}dx \qquad (11)$$

The first term on the right hand side is equal to zero, because of the boundary conditions of the DCB $\{\phi_n(0) = 0, \phi_n(\ell) = 0\}$ or cantilever $\left\{\phi_n(0) = 0, \frac{\partial^3\phi_n(x)}{\partial x^3} = 0\Big|_{x=\ell}\right\}$. Now we perform integration by parts on the second term of the right hand side of (11):

$$\int_{x=0}^{x=\ell}\phi_n(x)\frac{\partial^4\phi_n(x)}{\partial x^4}dx = -\frac{\partial\phi_n(x)}{\partial x}\frac{\partial^2\phi_n(x)}{\partial x^2}\Big]_{x=0}^{x=\ell} + \int_{x=0}^{x=\ell}\frac{\partial^2\phi_n(x)}{\partial x^2}\frac{\partial^2\phi_n(x)}{\partial x^2}dx \qquad (12)$$

Again the first term on the right hand side is equal to zero because of the boundary conditions for DCBs and cantilever. Thus we can rewrite (11) as:

$$\int_{x=0}^{x=\ell} \phi_n(x) \frac{\partial^4 \phi_n(x)}{\partial x^4} dx = \int_{x=0}^{x=\ell} \left(\frac{\partial^2 \phi_n(x)}{\partial x^2} \right)^2 dx \tag{13}$$

With this result, equation (10) becomes:

$$EI\, q_n(t) \int_{x=0}^{x=\ell} \left(\frac{\partial^2 \phi_n(x)}{\partial x^2} \right)^2 dx + \rho S \ddot{q}_n(t) \int_{x=0}^{x=\ell} \phi_n(x)^2 dx = 0 \tag{14}$$

It can be rewritten as:

$$q_n(t) \times \underbrace{EI \int_{x=0}^{x=\ell} \left(\frac{\partial^2 \phi_n(x)}{\partial x^2} \right)^2 dx}_{k_{eff}} + \ddot{q}_n(t) \times \underbrace{\rho S \int_{x=0}^{x=\ell} \phi_n(x)^2 dx}_{M_{eff}} = 0 \tag{15}$$

$$q_n(t) k_{eff} + \ddot{q}_n(t) M_{eff} = 0 \tag{16}$$

Equation (16) above is the harmonic oscillator model for the vibrational mode. In this model the time dependent term for the oscillation amplitude, $q_n(t)$, becomes the dynamical variable of interest. The first term above describes a restoring force and indeed originates from the restoring potential of the elastodyamic response of the beam. The second term above describes an inertial term, and it indeed originates from the inertia of the beam.

Writing $q_n(t) = A_n \sin(\omega_n t + \theta_n)$, we obtain the resonance frequencies as:

$$\omega_n = \sqrt{k_{eff}/M_{eff}} = \sqrt{\frac{EI}{\rho S}} \left(\frac{\int_{x=0}^{x=\ell} \left(\frac{\partial^2 \phi_n(x)}{\partial x^2} \right)^2 dx}{\int_{x=0}^{x=\ell} \phi_n(x)^2 dx} \right)^{1/2} \tag{17}$$

2.3 Shift in the Resonance Frequency Due to Mass Loading

We are now in a position to discuss how the resonance frequency of a resonator changes as a point-mass is added to it. The simplest approach is to add the point mass to the effective mass of the resonator, as the two start to oscillate together:

$$M_{eff} \rightarrow M_{eff} + \Delta m \tag{18}$$

Hence the resonance frequency changes to:

$$\omega = \sqrt{\frac{k_{eff}}{M_{eff}}} \rightarrow \omega' = \sqrt{\frac{k_{eff}}{M_{eff} + \Delta m}} \approx \sqrt{\frac{k_{eff}}{M_{eff}}}\left(1 - \frac{1}{2}\frac{\Delta m}{M_{eff}}\right) \tag{19}$$

We have used the first two terms of the Taylor series in the last step ($\Delta m \ll M_{eff}$). Taking the difference between the new and original frequencies, we obtain the frequency shift:

$$\omega - \omega' \equiv \Delta\omega = -\frac{1}{2}\frac{\omega}{M_{eff}}\Delta m \tag{20}$$

The prefactor, $-\frac{1}{2}\frac{\omega}{M_{eff}}$, is called the responsivity of the NEMS, as the change we want to measure (additional mass, Δm) gets scaled with this prefactor to form the physical quantity we can read out (the frequency shift Δf).

The treatment above is a first order approximation: we only added the mass of the analyte to the effective mass of the resonator, somewhat intuitively. We need to deal with this problem more rigorously. Furthermore, this first-order result does not contain any dependency on the position of the particle. However, frequency shift actually depends on where the particle lands along the length of the beam. We need to figure out this

dependency to interpret our experimental results and find ways to overcome the position dependency, a prerequisite for performing single-shot mass measurements.

In the reminder of this section we will calculate the position dependent frequency shift in two different, but equivalent ways. In the first method, we will use energy formalism. In the second way, we will use Newton's second equation. Our starting point for both cases will be the harmonic oscillator model of the beam described by equation (16). The energy method is more straightforward to use; whereas, the force method may later be incorporated with the equation of motion for a nonlinear beam to compute the frequency change in cases where NEMS is driven beyond the linearity threshold.

Energy Method

The restoring force and inertia terms in the harmonic oscillator in equation (16) above can be converted into potential energy and kinetic energy forms, respectively:

$$U = \frac{1}{2} k_{eff} q^2 \quad T = \frac{1}{2} M_{eff}\, \dot{q}^2 \tag{21}$$

Here U denotes the potential energy term, and T denotes the kinetic energy terms. When a particle lands on the beam at position a, it will start to oscillate with the beam as shown in Figure 3. At any point in time, the particle's vertical displacement will be: $p(t) = q(t)\phi(a)$. Thus the particle will increase the kinetic energy of the system by its own kinetic energy: $T_{particle} = \frac{1}{2}\Delta m\, \dot{p}^2 = \frac{1}{2}\, \Delta m\, \phi(a)^2\, \dot{q}^2$. Hence the system will now be described by:

$$T_{system} = T_{beam} + T_{particle} = \frac{1}{2}\left(M_{eff} + \Delta m\, \phi(a)^2\right) \dot{q}^2 \qquad U = \frac{1}{2} k_{eff} q^2 \tag{22}$$

For this quadratic system, the resonance frequency will be:

$$\omega' = \sqrt{\frac{k_{eff}}{M_{eff} + \Delta m\, \phi(a)^2}} \approx \sqrt{\frac{k_{eff}}{M_{eff}}}\left(1 - \frac{1}{2}\frac{\Delta m}{M_{eff}}\phi(a)^2\right) \quad (23)$$

$$\Delta\omega = -\frac{1}{2}\frac{\omega}{M_{eff}}\Delta m\, \phi(a)^2 \quad (24)$$

Thus the frequency shift is scaled by the squared value of the mode shape at the landing point of the particle.

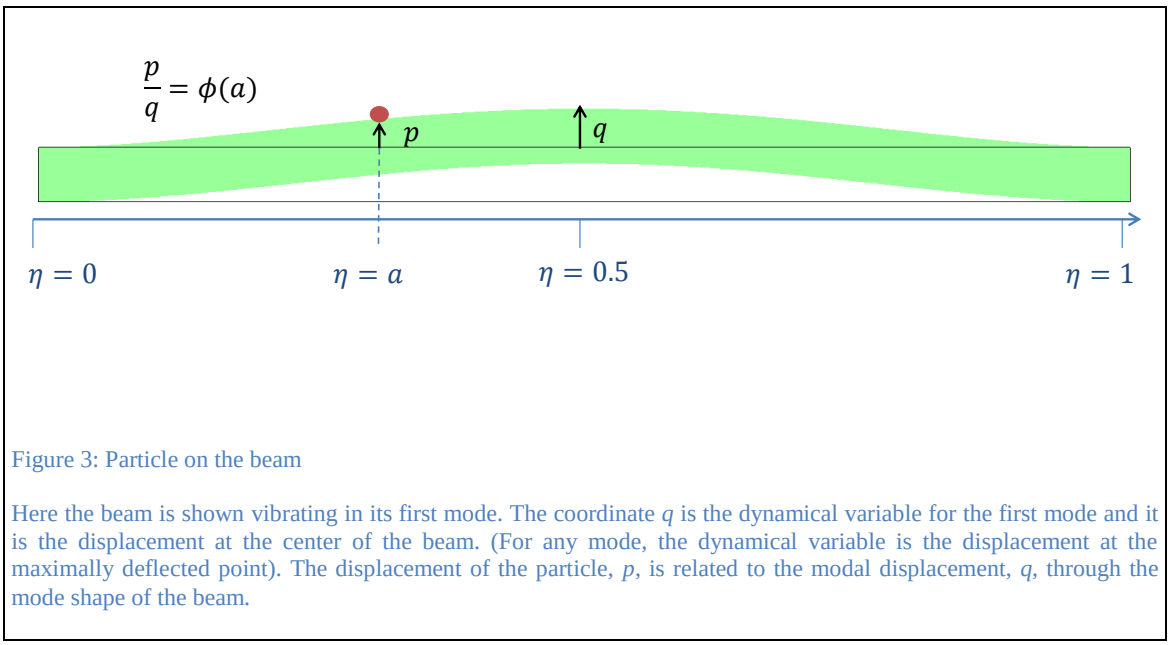

Figure 3: Particle on the beam

Here the beam is shown vibrating in its first mode. The coordinate *q* is the dynamical variable for the first mode and it is the displacement at the center of the beam. (For any mode, the dynamical variable is the displacement at the maximally deflected point). The displacement of the particle, *p*, is related to the modal displacement, *q*, through the mode shape of the beam.

Force Method

Alternatively, we can treat the beam as an isolated system, and calculate the force exerted by the particle on the beam. We will incorporate this force into the equation of motion for the beam to find the resonance frequency.

As mentioned above, the vertical displacement of the particle is $p(t) = \phi(a)q(t)$ and thus the acceleration of the particles is: $\ddot{p} = \phi(a)\ddot{q}(t)$.This acceleration is caused by a vertical force on the particle by the beam: $F_{on-particle} = \Delta m\phi(a)\ddot{q}(t)$. Obviously, the

force on the beam due to the particle is the opposite of this force: $F_{on-beam} = -\Delta m\phi(a)\ddot{q}(t)$. We can convert this force to a one dimensional force density:

$$f_{on-beam} = -\Delta m\, \phi(a)\ddot{q}(t)\delta(x-a) \tag{25}$$

here $\delta(x)$ is the (Dirac) delta function. We use the force density to match the dimensionality of the Euler-Bernoulli equation. We can plug this force density term into the equations of motion:

$$EI\, q(t)\frac{\partial^4\phi(x)}{\partial x^4} + \rho S\frac{\partial^2 q(t)}{\partial t^2}\phi(x) = f(x) \tag{26}$$

$$EI\, q(t)\frac{\partial^4\phi(x)}{\partial x^4} + \rho S\frac{\partial^2 q(t)}{\partial t^2}\phi(x) = -\Delta m\, \phi(a)\ddot{q}(t)\delta(x-a) \tag{27}$$

Now we proceed as before, by multiplying the above equation with the mode shapes, $\phi(x)$ and integrating over the length of the beam:

$$\begin{aligned} EI\, q(t)\int_{x=0}^{x=\ell}\phi(x)\frac{\partial^4\phi(x)}{\partial x^4}dx + \rho S\ddot{q}(t)\int_{x=0}^{x=\ell}\phi(x)^2 dx \\ = -\Delta m\phi(a)\ddot{q}(t)\int_{x=0}^{x=\ell}\phi(x)\delta(x-a)dx \end{aligned} \tag{28}$$

On the left hand side, we end up with the effective spring constant and effective mass terms, as before. On the right hand side, we can use the sampling property of the delta function to evaluate the integral, $\int \phi(x)\delta(x-a)dx = \phi(a)$ yielding:

$$k_{eff}q(t) + M_{eff}\ddot{q}(t) = -\Delta m\phi(a)^2\ddot{q}(t) \tag{29}$$

Rewriting (29) yields:

$$k_{eff}q(t) + (M_{eff} + \Delta m\phi(a)^2)\ddot{q}(t) = 0 \tag{30}$$

We can now find the shift in resonant frequency:

$$\omega' = \sqrt{\frac{k_{eff}}{M_{eff} + \Delta m\, \phi(a)^2}} \approx \sqrt{\frac{k_{eff}}{M_{eff}}}\left(1 - \frac{1}{2}\frac{\Delta m}{M_{eff}}\phi(a)^2\right) \tag{31}$$

$$\Delta\omega = -\frac{1}{2}\frac{\omega}{M_{eff}}\Delta m\, \phi(a)^2 \tag{32}$$

as before.

2.4 Effects of Position Dependency on the Experiments

Since the frequency shift is a function of both the mass and the position of the particle, it is not possible to weigh a particle using only a single mode. In the next chapter, we will tackle this problem by using multiple modes. However, with single mode measurements we can still obtain useful information about the mass of a species by collecting many events of the same species and removing the position dependency using statistics. It is reasonable to assume that the particles arriving on the beam have the same probability of landing anywhere on the beam. So when we consider an ensemble of particle landing events, the landing position will be a uniformly distributed variable. Using this assumption of uniform distribution, we can calculate a histogram for the frequency shift caused by a specific mass. Once we obtain this histogram, we can use it as a generic *form*

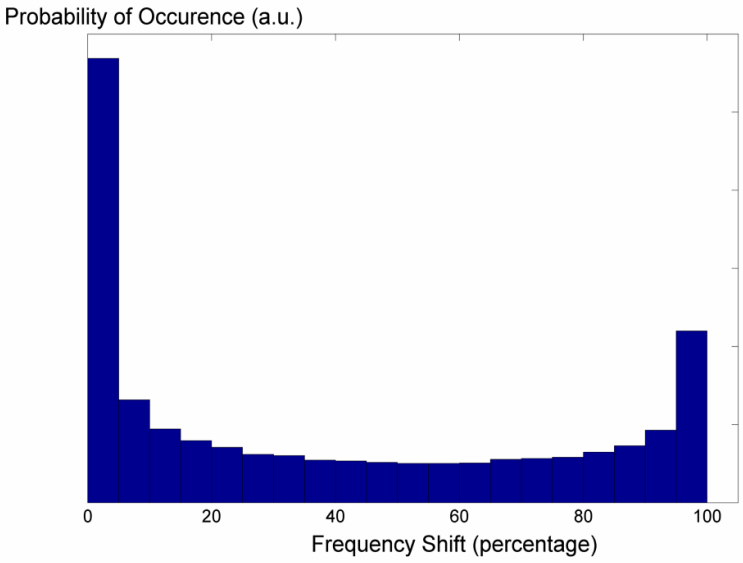

Figure 4: Expected histogram for frequency shift due to a constant mass

factor and interpret our experimental results. Figure 4 shows the generic histogram calculated by Monte Carlo simulations and distributed into twenty bins. The main feature of this histogram is its bicuspid shape. This type of histograms will be used in the analysis section to interpret the data.

2.5 Experimental Setup

We employ proven methodologies from state-of-the-art mass spectrometry to build a novel MS system using NEMS mass sensors. Components include a room-temperature, atmospheric pressure electrospray ionization (ESI) system for creating protein ions or charged nanoparticles, a differential vacuum system, the RF hexapole ion optics to guide the charged analytes to the detector, and the NEMS mass detector stage. These components are assembled to form a hybrid system

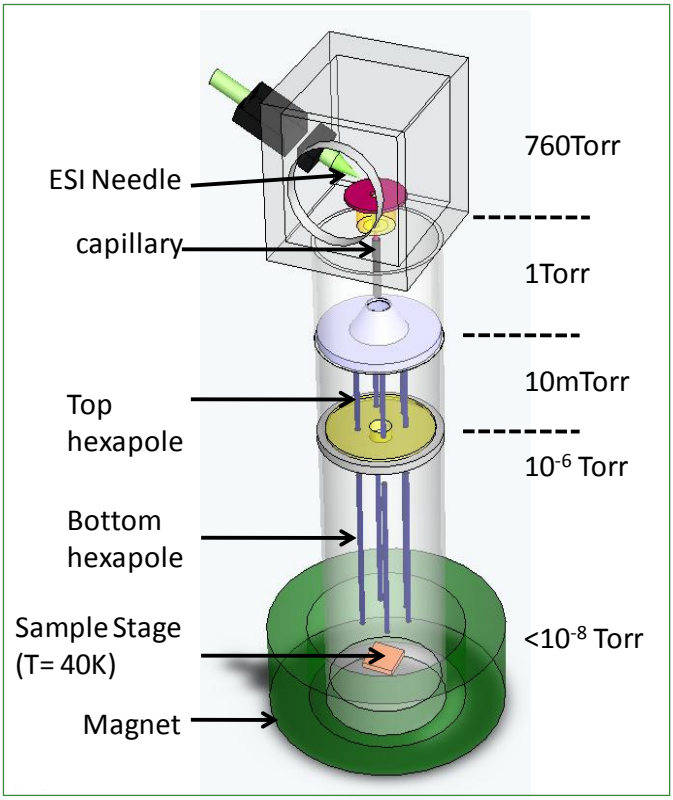

Figure 5: Experimental setup[‡‡]

[‡‡] Illustration Credit: Akshay Naik

comprised of both custom built and commercial instrumentation. Figure 5shows the experimental setup.

Figure 6 below is a montage of images depicting our first experimental prototype system for NEMS-MS enabling the introduction, transport, and mass measurements on individual proteins and nanoparticles. Protein ions or charged nanoparticles are produced using electrospray ionization (ESI) and delivered to a hexapole ion guide driven at radio frequencies (RF), which transports these species to the NEMS mass sensor with minimal *m/z* discrimination. The detection circuitry utilizes a bridge circuit to null the background near the NEMS resonance[9, 23, 24] and a frequency-modulated, phase-locked loop (FM-PLL) to track the NEMS resonant frequency in real time[11], as shown in Figure 8.

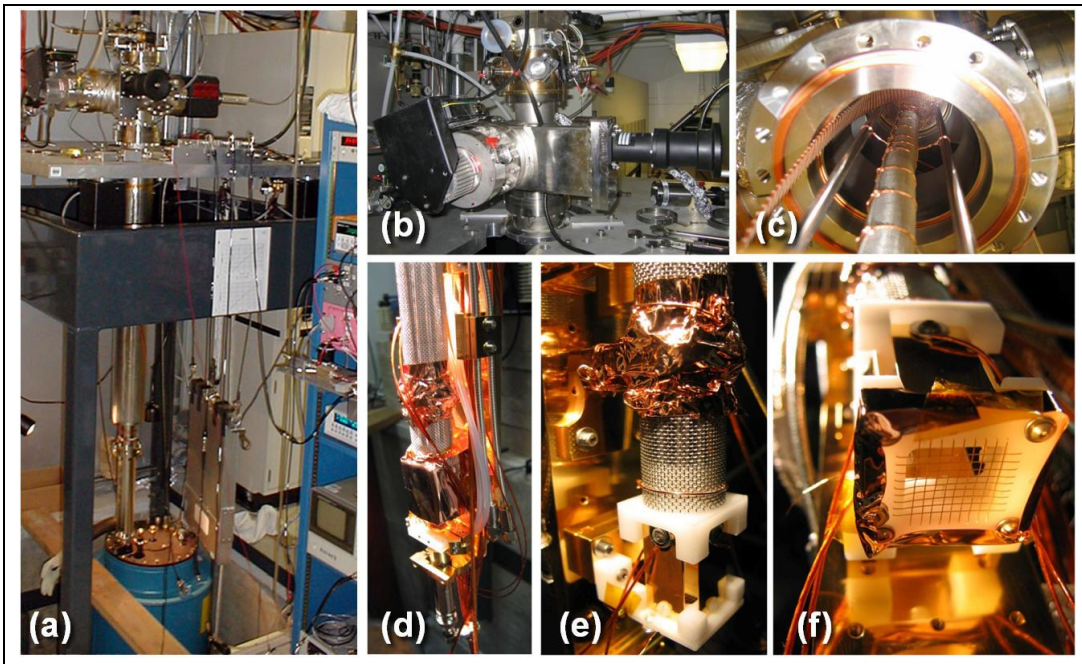

Figure 6: First generation NEMS MS system

(a) The cryostat, its vibration isolation & support system, and (in pit) the super-conducting magnet, and its dewar. (b) Electrospray ionization unit at top of system. (c) Hexapole ion guide from bottom. (d)(e) Sample stage region; progressive magnifications. (f) Hexapole ion guide; outlet detail

2.6 Creation and Transportation of Ions

Electrospray Ionization (ESI) and differential vacuum assembly

Protein ions and charged nanoparticles are produced using a commercial electrospray ionization (ESI) system (Varian). ESI is one of two well known "soft" ionization processes that can reliably bring large macromolecules from solution phase to vapor phase [2]**.** The other prevalent technique is *MALDI*, Matrix-Assisted Laser Desorption Ionization. See **Error! Reference source not found.** for the rationale behind the selection of ESI for our experiments.

These solutions were introduced using a syringe pump (Harvard Apparatus) and syringes (Hamilton) to the electrospray needle (Agilent) by direct infusion through standard MS components (Upchurch) to achieve typical flow rates of 4 μL/min. High-voltage sources (Emco) are used to bias the ESI needle at a constant voltage of ~2.5-3kV. Solvated analytes delivered to the needle are ejected out in the form of charged droplets, repelling each other due to Coulombic forces. The solvent within these droplets evaporates, reducing the volume yet preserving the charge of the droplets. Hence charge per volume increases, increasing the repulsive force within the droplets. The increasingly unstable microdroplets eventually undergo "Coulomb fission", fragmenting into offspring droplets. Repeated cycles of this process ultimately result in the formation of bare ionized proteins. Although the exact mechanism of protein ion formation from small droplets (< 20 nm) is still under debate [25], electrospray has become a well-established technique for producing proteins in vapor form.

Our ESI delivery system is built around a commercial sub-assembly (Varian 1200 LC/MS) and comprises the following components:

1) An ESI needle and gas sheath mounted in an outer chamber at atmospheric pressure and room temperature.

2) A 1st vacuum stage with a shield plate, counterflow gas path, capillary, and pumping port.

3) A 2nd vacuum stage including a skimmer, collisional-cooling hexapole (i.e. the "top hexapole"), and final high vacuum orifice. This sub-assembly is embedded in a custom 2nd stage vacuum chamber designed for about 10 mtorr base pressure for optimal collisional cooling of the ions [26, 27]. It is then attached to the top plate of the high-vacuum cryostat chamber housing the "bottom hexapole" (see below) and the NEMS sample stage.

All N2 gas, vacuum port, electronic, and fluidic connections, are retrofitted to external instrumentation.

Ion transport

In practice, electrospray ionization is performed at atmospheric pressure and room (or elevated) temperature, so that the solvent in the droplets can evaporate quickly to produce protein ions. The magnetomotive detection and the physiosorption process used in this first-generation NEMS-MS realization require the NEMS sensor to be maintained in high-magnetic field, high-vacuum, and low temperature conditions. Our experimental setup is built with commercially available cryogenic and differential pumping

components to enable these operating conditions. Our first-generation design requires placing the NEMS device about 2 m away from the ESI source. Since the capture area of the NEMS sensor is small, analyte ions created by electrospray must be transported efficiently through this 2 m path.

The transportation of ions from atmosphere to the first differential pumping stage is performed through the so called nozzle-skimmer configuration [28, 29], which produces a highly collinear, monochromatic beam of nitrogen molecules and protein ions. Further transportation of ions from this initial vacuum stage to the NEMS chip is achieved by a hexapole ion guiding system, having an outer radius of ~ 1.2 cm and length of ~ 2m. The hexapole configuration was chosen as a good compromise between good transmission efficiency and minimal *m/z* selectivity. This configuration consists of a two-stage hexapole ion guiding system. The top hexapole, operating in the 10 mTorr vacuum range, provides collisional cooling and trapping of the ions. The bottom hexapole plays a dual role. It acts as an ion pipe with broadband, high-efficiency transmission of ions over the 2 m path. It is also key in overcoming the magnetic mirror effect that would otherwise reflect the ions back along their initial path as they tried to enter the high magnetic field region[30, 31]. Both of the hexapoles are driven by a homemade RF oscillator [32, 33] that can supply AC voltages of up to $500V_{peak}$. In brief, the RF power supply is based on two vacuum tubes operating in a push-pull oscillator configuration, driving an LC load formed by a high-voltage inductor, the capacitive load of the hexapole rods and additional capacitors to tune the frequency of oscillation. The excessive length of the lower hexapole set an upper limit to the frequency that can effectively be applied by the voltage source, though it did not come into play with the large masses probed in this

experiment. The NEMS mass sensor is centered about 3 mm below the bottom end of the hexapole guide.

Parameter	Description	Typical Values
V_{needle}	Voltage on the electrospray needle	3.0 kV
V_{L4}	Voltage on the electrostatic lens between top and bottom hexapole	-20 V
V_{Shield}	Voltage on the shield (ESI counter electrode)	600 V
$V_{capillary}$	Voltage on the capillary	200 V
V_{top_hex}	DC offset voltage on the top hexapole	10 V
V_{bot_hex}	DC offset voltage on the bottom hexapole	0 V
f_{RF}	RF frequency of AC voltage applied to the hexapole	1.1 MHz, 450 kHz
V_{RF}	Amplitude of the RF voltage applied to hexapole	500 V
P_{int}	Pressure in the intermediate collisional focusing chamber	8 mTorr
T_{dry}	Temperature of the drying gas	180 ^{0}C
P_{dry}	Pressure of the drying gas	30 psi
P_{neb}	Pressure of the nebulising gas	15 psi
R	Protein solution flow rate	4 μl/min

Table 2: Typical values used during ESI and ion optics

2.7 NEMS Device: Fabrication, Transduction, and Temporal Response

The structural material for the ultrahigh frequency (UHF) NEMS devices in this work is a 100 nm thick single crystal 3-C silicon carbide (SiC) epilayer deposited on a silicon substrate through molecular beam epitaxy[34]. Thin-film metal conductors are defined by optical lithography to form wirebond pads and a lead-frame that each converge into a central, active region for each device. Each of these small chips is manually diced for subsequent individual processing. Electron-beam lithography is used to laterally define

what will become the nanometer scale NEMS features on the SiC epilayer. Thermal evaporation is used to deposit 40nm of Al followed by 5nm Ti on these patterns, and standard lift-off then defines the metallization layer. This metallization layer connects to the larger lead-frame, and also serves as a mask for the subsequent etching process. The masked SiC epilayer is etched in an Ar/NF_3 plasma created by an electron cyclotron resonance etching system. This dry etch step removes the SiC in unprotected regions and undercuts the silicon beneath the masked SiC, resulting in a fully suspended NEMS beams [35]. The completed ddvices depicted in Figure 7 and are geometrically characterized by a scanning electron microscope (SEM).

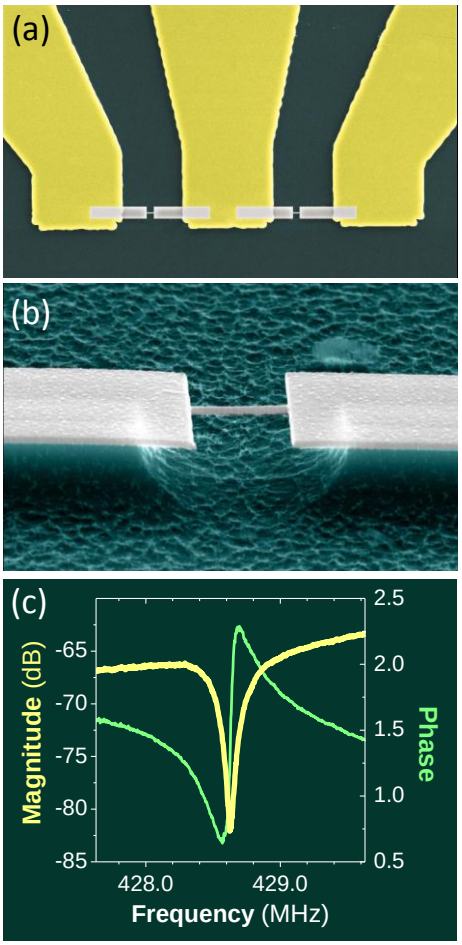

Figure 7: NEMS device

(a.b) Scanning electron micrographs showing one of the NEMS device used in the experiments. (c) Magnitude and phase of the UHF NEMS resonator's response displaying a fundamental mode resonance near 428MHz.

The NEMS mass sensor used in these measurements is a 100nm thick, doubly-clamped silicon carbide beam ~1.7μm long, ~120nm wide. In addition to its function as an etch mask, the topmost, thin-film metallization layer subsequently enables magnetomotive actuation and transduction[4].

We use network analyzer to obtain the resonance features like the frequency sweep shown in Figure 7c. A circuit diagram for this measurement is shown in Figure 8 (a). We use the circuitry shown on Figure 9 (b) to track the NEMS frequency in real time. Before each PLL run, we need to adjust and test the response time of the PLL. The mass loading event changes the frequency of the NEMS beam quasi-instantaneously (i.e. much faster than the other timescales involved). However the electronic circuitry cannot drive the frequency immediately to the correct value: it takes a certain amount of response time for the electronics to reach the correct frequency. This temporal response is determined by such factors as the lock-in time constant, sampling time, various feedback gains in the loop, the latency of the GPIB communication system etc. We modeled the temporal response of the electronic circuits, and we fit every jump to this model as a further check.

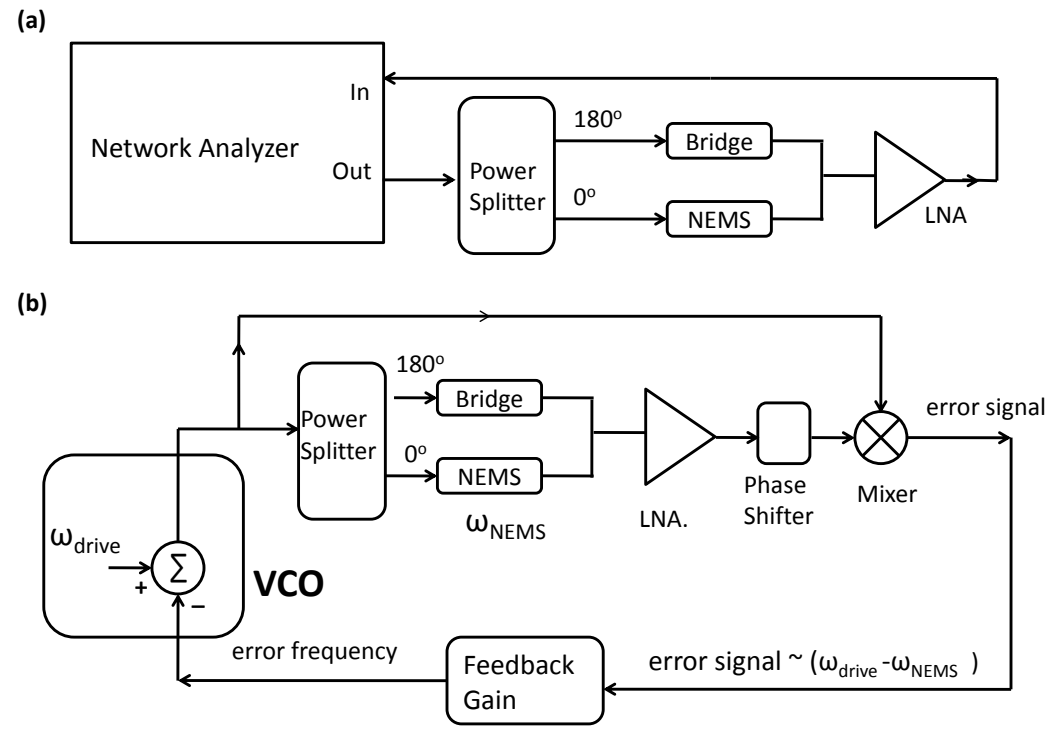

Figure 8: Measurement circuits

(a) For the open loop response (b) For the PLL operation.

2.8 Frequency Jump Data

We report here the first NEMS-MS spectra for proteins and nanoparticles as shown in Figure 9 . Our analyses are carried out by observing hundreds of frequency shifts per species in real time; each frequency shift is associated with an individual protein or nanoparticle adsorption event. Each ESI run is followed by a control run of equal duration during which the ESI solution pump is shut off to establish the frequency-fluctuation background. Given the ~250 Hz resolution in these measurements, we construct event probability histograms with 250 Hz bins, and reject false positives arising from frequency-fluctuation noise by discarding jumps smaller than 2σ (=500Hz).

To verify that the change in resonant frequency of the NEMS is due to mass loading from protein molecules or nanoparticles landing on the NEMS, we perform the following three distinct control runs while tracking the resonant frequency of the NEMS:

1) We turn off the syringe pump delivering the protein solution to the ESI needle and keep all ESI voltages and ion optics control voltages on. Proteins do not reach the ESI needle, hence protein ions should not be produced (beyond rare events arising from the dislodging of sparse protein residue accumulated within the needle, etc. – *i.e.* from previous NEMS-MS runs.)
2) We turn off the ESI needle voltage. All the other parameters are kept the same as for ESU injection during regular NEMS-MS operations. In this case although the protein solution is ejected from the ESI needle due to the flow pressure generated by the

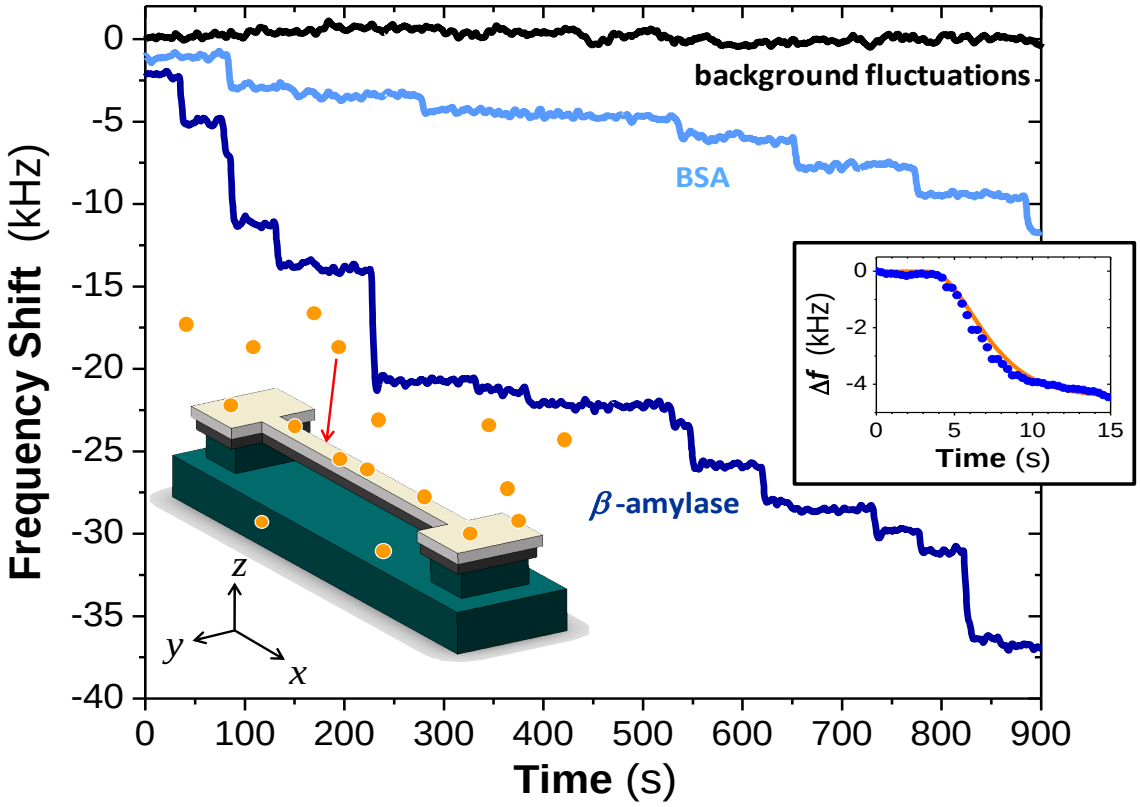

Figure 9: Real-time records of single-molecule adsorption events upon a NEMS mass sensor.

This raw experimental data shows the distinctly-different, precipitous resonance frequency shifts of the NEMS during ESI-induced adsorption of bovine serum albumin (BSA, 66kDa) and β-amylase (200kDa). Each frequency jump downward is due to an individual protein adsorption event on the NEMS mass sensor. The height of the frequency jump is a convolved function of the mass of the protein adsorbed, and its position of adsorption upon the NEMS. Right Inset: Raw data from a typical discrete event (blue dots), and a non-linear least square fit to the system's response (orange line) based on the temporal response function of the control loop. Left Inset: Schematic illustrating single-molecule adsorption events on a NEMS resonator, and the coordinate system used to define its position-dependent mass responsivity.

syringe pump and the nebulizing gas flow, the resulting droplets are not charged. Any proteins, if produced, will not be transported to the NEMS by the ion guide.

3) We run the ESI with the clean solvent devoid of analytes. Assuming that there are no leftover proteins in the ESI system (as described in the scenario for control run #1) we should see minimal change in the resonant frequency of the NEMS.

Figure 10 shows one such time record of the resonant frequency of the NEMS during the ESI of Bovine Serum Albumin (66kDa) and three different control runs. The resonant frequency of the NEMS changes radically during the ESI of BSA protein. The frequency change is composed of scores of frequency jumps similar to the ones shown in Figure 2. During the control runs, however, the change in resonant frequency is noticeably smaller which indicates that the mass loading is indeed due to the protein ions produced during ESI. We believe the mass loading of the NEMS during the ESI of the solvent is largely due to proteins leftover in the ESI system from previous runs. The resonant frequency changes during the other two control runs are minimal and compare well with the frequency fluctuations observed due to background gas molecules.

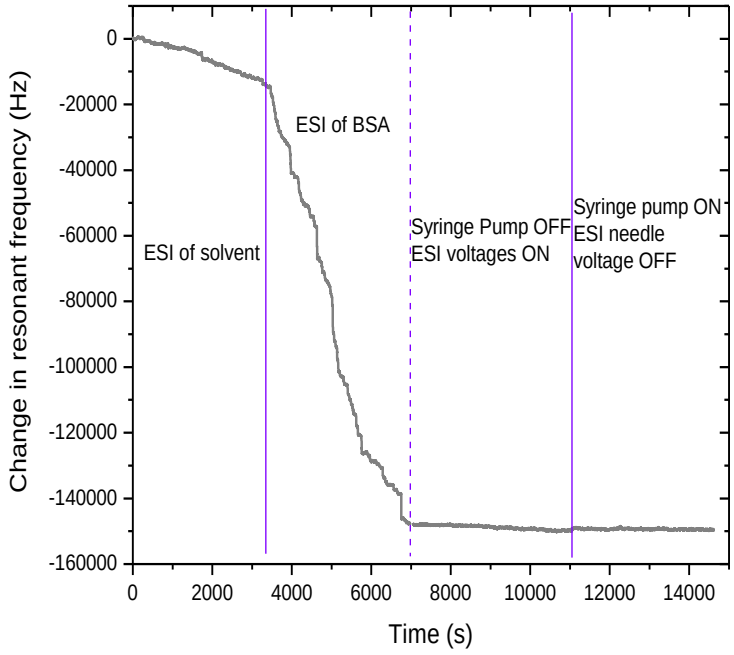

Figure 10: Control run

The response of the NEMS frequency during the control runs and the ESI of BSA.

2.9 Interpretation of the Data

Figure 11 (b) shows an experimental histogram constructed from data obtained by electrospraying a colloidal solution of nanoparticles. The Au nanoparticles used are characterized by the vendor as having average radius of 2.5nm and standard deviation "less than" 0.375nm (Sigma-Aldrich). What is ostensibly a small standard deviation in radius actually corresponds to a very large spread in nanoparticle mass; the advertised specifications translate to an average mass of ~780kDa and 1σ mass range from 480kDa to 1190kDa. This substantial dispersion, and our finite frequency-fluctuation noise, together conspire to significantly smooth the canonical bicuspid spectrum expected theoretically for the ideal case (Figure 11a).

Figure 11c shows the residues for a two-parameter least-squares fit of a theoretical event-probability curve to the experimental histogram data. The two fitting parameters are average nanoparticle radius and its dispersion; the theoretical curve incorporates the experimentally measured frequency shift resolution of $\delta f = 250$ Hz. With this approach, by recording just 544 individual nanoparticle adsorption events, we resolve an average nanoparticle radius of 2.15 nm, corresponding to an average mass of 490 kDa, with a standard deviation of nanoparticle radius of 0.5 nm.

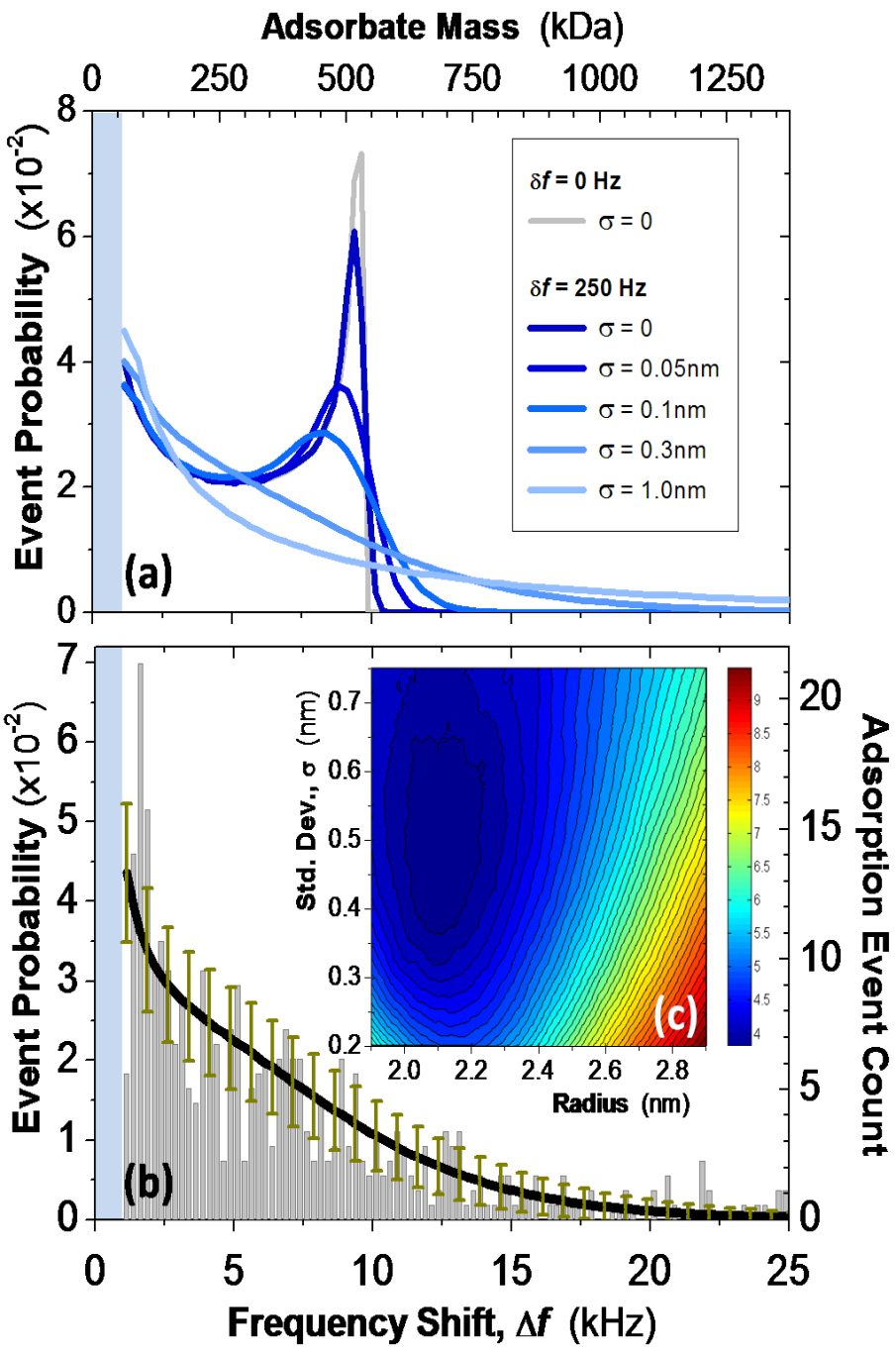

Figure 11: NEMS mass spectrometry of a gold nanoparticle dispersion
(a) Theoretically expected event probabilities versus frequency-jump amplitudes are shown for "nominal" 2.5 nm radius Au nanoparticles , delivered with an average flux uniformity that is distributed over a doubly-clamped beam having mass responsivity ~12Hz/zg. Traces show expected results for a monodisperse ensemble of particles, as well as for several dispersions (characterized by their radius standard deviations), for the cases of perfect (0Hz) and experimentally relevant (250 Hz) frequency resolutions. **(b)** Experimentally obtained histogram of adsorption event probabilities versus frequency-jump **amplitude for electrosprayed gold nanoparticles, and the expected curve for a average radius of 2.15nm and a radial dispersion of 0.375nm (black trace). Error bars (dark yellow) display the theoretically-expected deviations corresponding to 544 adsorption events, as registered in this experiment. (c)** Contour plot showing the residues for least-square fits to the experimental data using radius and radial dispersion as the fitting parameter. These data establish the average radius and size dispersion for the 544 nanoparticles measured.

Figure 12 shows NEMS-MS spectra obtained for a “nominally pure” solution of the protein bovine serum albumin (“BSA”, 66kDa). From the standpoint of MS, pure solutions of protein are the exception rather than the rule, and the NEMS-MS spectra of Figure 4 bear out this truism. Protein molecules can often aggregate in solution to form protein oligomers, and each distinct assemblage will produce its own characteristic bicuspid NEMS-MS histogram. A multi-component solution of such oligomers will thus superpose to produce a complex spectrum.

The presence of a family of oligomers has two significant effects on the shape of NEMS–MS histograms. First, the low-frequency shift cusps for each of the oligomers (occurring at the same, zero frequency shift) superpose to produce a single, prominent peak. Second, the high-frequency shift cusps of the oligomers, which occur at different frequency shifts corresponding to each specific component’s mass, become engulfed in the tails from other components. This tends to suppress their overall individual prominence.

Figure 12 illustrates event probabilities as a function of frequency shift for electrosprayed BSA ions that are transported to the NEMS sensor with a hexapole drive frequency of 1.1 MHz. For comparison, also shown are theoretically expected event probabilities for BSA oligomers, generated using the experimentally measured NEMS sensor’s mass responsivity of 12 Hz/zg and using a least-squares fit to the data—similar to that used for the gold nanoparticle dispersion, but here implemented to extract the spectral weights for the first five oligomers .The spectrum in Figure 12 shows clear peaks at 3,375 and 5,875 Hz, assigned to BSA trimers and pentamers, respectively. The broadly distributed spectral weight below 2 kHz arises from monomers and dimers. Note that this

full spectrum has been obtained by recording the individual adsorption of only 578 BSA molecules.

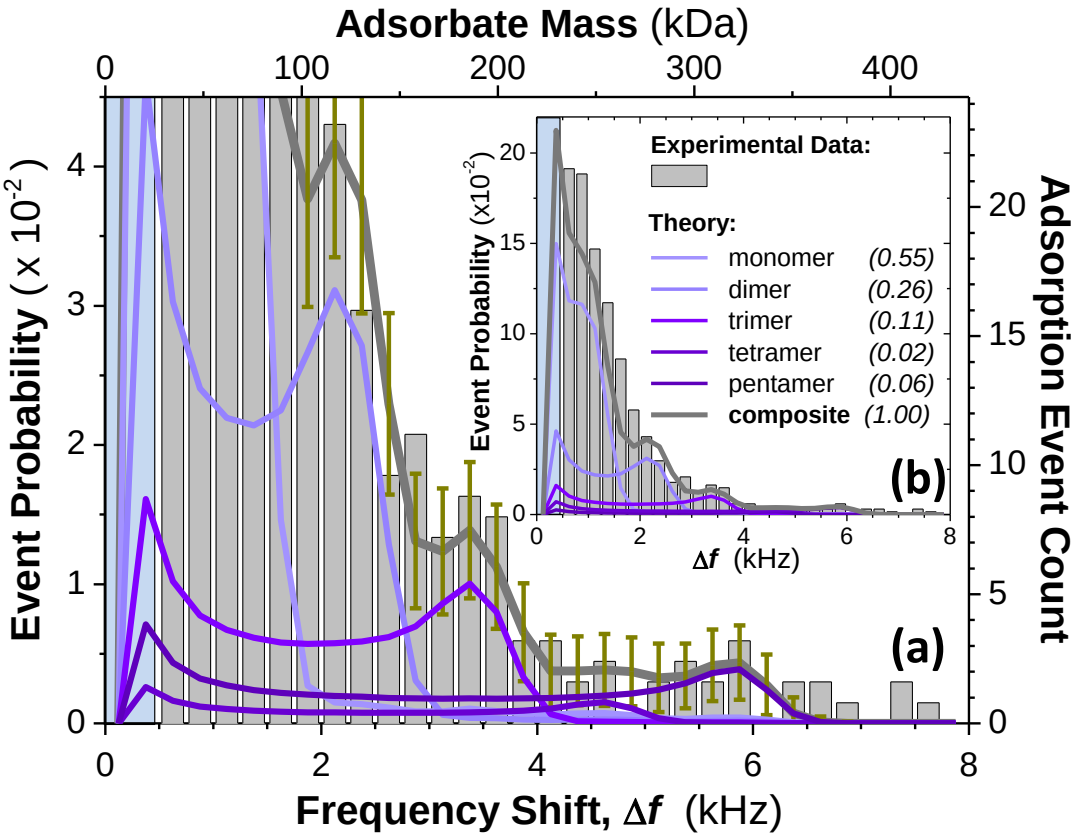

Figure 12: NEMS mass spectrometry of proteins.

NEMS-MS of bovine serum albumin (BSA) enabled by adsorption-event probability analysis. Experimentally obtained frequency-jump data are binned into 250Hz histograms commensurate with the experimental mass resolution. Applying a 2σ detection criterion, we reject data below 500Hz (blue-shaded regions; see text). (a) Expanded view of the low-event-probability region displaying a clearly detailed decomposition of the simultaneous contributions from oligomers. The theoretical composite curve (grey) is a weighted superposition of adsorption probabilities of the intact monomer and a family of its oligomers deterministically calculated by a least-squares process similar to that of Figure 3 (b) Full view of entire data set. The numerically-determined best-fit weighting coefficients for the composite curve are displayed in the legend.

CHAPTER 3:

MULTIMODE MASS DETECTION AND ERROR ANALYSIS FOR MASS MEASUREMENTS

3.1 Statement of the Problem

As mentioned in the last chapter, when a molecule lands on a NEMS resonator, it causes a frequency shift that depends not only on the mass of the molecule but also on the position of the molecule. This position-dependency prevents us from measuring the mass of a single molecule in one shot. Previously, we removed the position information and obtained the molecular mass by collecting many data points of the same species and assuming a uniform distribution for the landing position.

Ideally we want to perform single-shot mass measurements on each molecule reaching the device. To that end, we have developed a method that is sensitive only to the mass of the molecule. In this method, we track the resonance frequency of two flexural modes of a NEMS device and record the frequency shifts for each mode when a particle arrives. We combine the frequency shift data from each mode to obtain the mass information.

In this chapter we will show how to combine the multimode data to infer the mass of the particle. We can combine these multimode data most easily if we use a doubly-clamped beam. Therefore we will focused mostly on the doubly-clamped beam in this work. After

combining the frequency shift information to determine the mass, we will calculate the error in mass measurements due to the frequency instability of the resonator. Finally, we will investigate a few relevant cases in more detail.

3.2 Single-Shot Mass Sensing with Two Modes

In chapter 2, we derived the harmonic oscillator model of a nanomechanical beam and calculated the effective mass of a resonator. Furthermore, we calculated the frequency shift as a function of the landing position of the point mass in equation (32). In this section, we will show how we can combine the frequency shift information from two different modes of a DCB to obtain the added mass. We will assume that the frequency shift of a mode due to a particle landing does not change with the concurrent excitation of other modes. We will show the validity of this assumption, to first order, in subsection 3.7.3.

We will begin by rescaling the x-axis by a new parameter η, so that beam lies between η=0 and η=1, Figure 13(a). In these coordinates, the effective mass of a vibration mode is written as:

$$M_{eff} = \left[\int_{\eta=0}^{\eta\ 1} \phi(\eta)^2 d\eta\right] \times M_{total} = \beta\ M_{total} \qquad (33)$$

Here $\phi(\eta)$ denotes the mode shape as before and it is normalized so that $\max(\phi(\eta)) = 1$. (The mode shapes for the first two modes are given in Figure 2) The integrand in equation (33) has the numerical value of β_n for the nth mode.

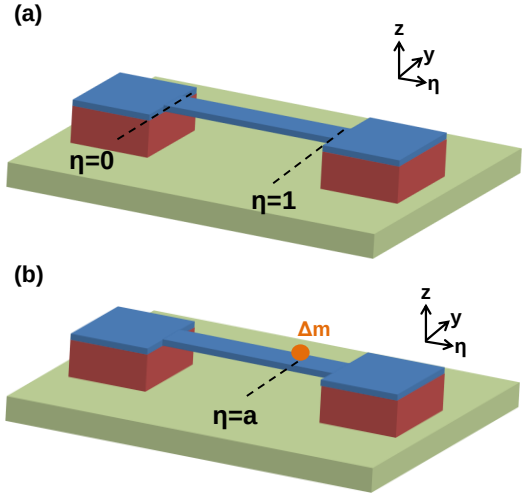

Figure 13: Beam in normalized coordinates

A molecule with mass Δm lands on the resonator at the longitudinal position η=a (Figure 13b). As shown before, the frequency shift caused by this molecule is given by:

$$\Delta f = -\frac{f_o}{2\beta M_{total}}\,\Delta m\;\phi(a)^2 \tag{34}$$

We define $\delta m \equiv \frac{\Delta m}{M_{total}}$ as the **normalized mass change** and $\delta f \equiv \frac{\Delta f}{f_o}$ as the **normalized frequency shift.** Also for convenience we define: $\alpha \equiv -2\beta$. Using these definitions and rearranging the terms we get:

$$\delta m\;\phi(a)^2 = \alpha\,\delta f \tag{35}$$

This equation (35) is valid for any particular mode in which we are interested. We can generalize this for the nth mode of the beam:

$$\delta m\;\phi_n(a)^2 = \alpha_n\,\delta f_n \tag{36}$$

Now we want to show that for a doubly-clamped beam, the added mass can be determined with only two modes. We start by writing these two equations explicitly:

$$\delta m\ \phi_1(a)^2 = \alpha_1\ \delta f_1 \tag{37}$$

$$\delta m\ \phi_2(a)^2 = \alpha_2\ \delta f_2 \tag{38}$$

Now we can eliminate δm by dividing equation (37) by equation (38) :

$$\frac{\phi_1(a)^2}{\phi_2(a)^2} = \frac{\alpha_1\ \delta f_1}{\alpha_2\ \delta f_2} \tag{39}$$

We define a new function $G(a) \equiv \frac{\phi_1(a)^2}{\phi_2(a)^2}$, and equation (39) becomes:

$$G(a) = \frac{\alpha_1\ \delta f_1}{\alpha_2\ \delta f_2} \tag{40}$$

If G(η) were an invertible function, i.e. if G^{-1} existed, then we could solve equation (40) for a:

$$If\ G^{-1}exist\ \rightarrow a = G^{-1}\left(\frac{\alpha_1\ \delta f_1}{\alpha_2\ \delta f_2}\right) \tag{41}$$

Once we solve for a, we can obtain δm by direct substitution above. The problem is whether or not $G(a)$ is invertible. A smooth function is invertible, if it is one-to-one and onto. To see how $G(a)$ behaves; we plot this function for DCB and cantilever in Figure 14 (a) and (b), respectively. Although in both cases the function is onto, it is **not** one-to-one in either case. Hence $G(a)$ is not an invertible function: G^{-1} does not exist and we cannot find a single value for the position, a. These statements hold true for any combination of two modes in a DCB or a cantilever. The bottom line is, we cannot determine the position of the adsorbate with only two flexural modes – we need at least three.

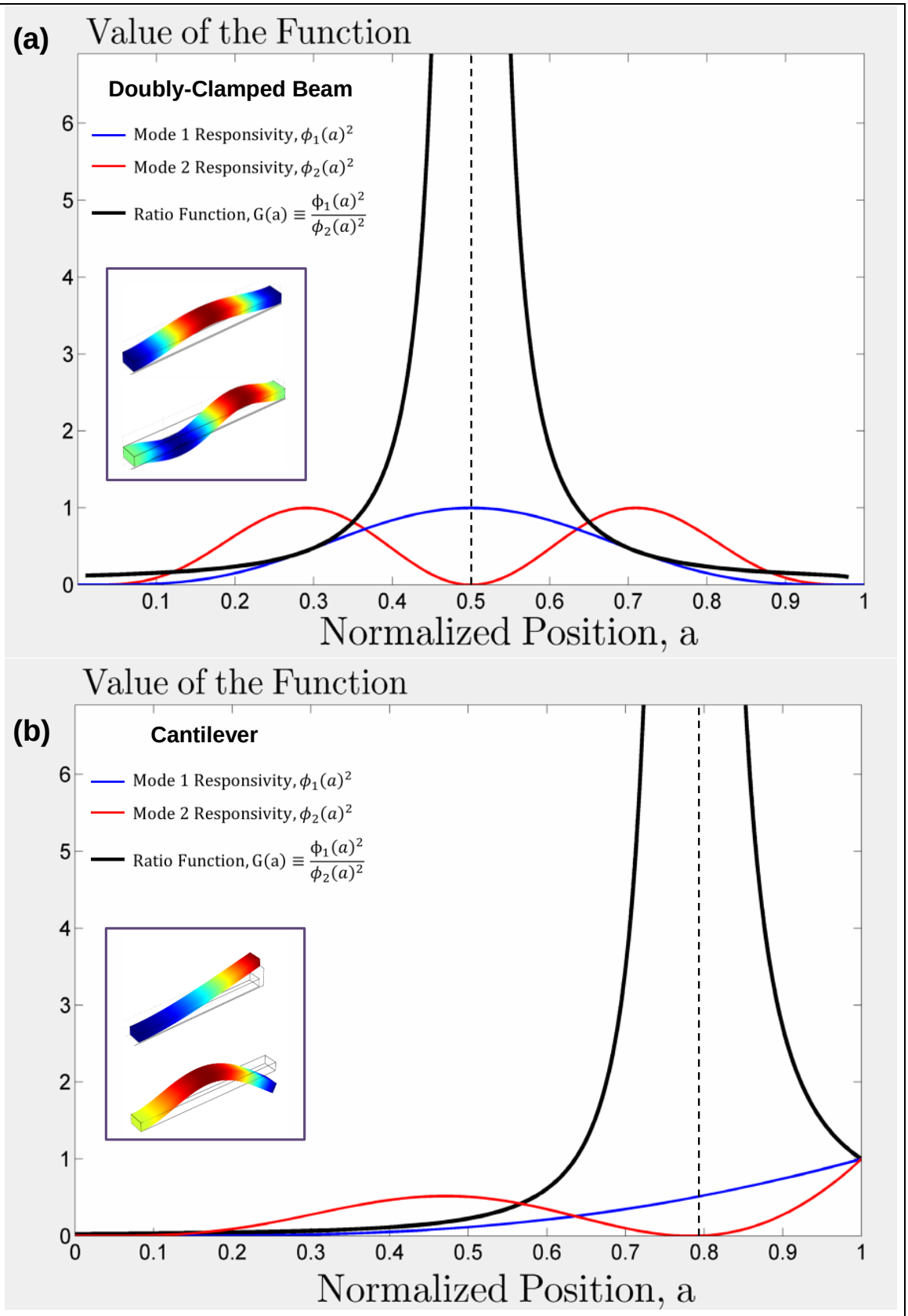

Figure 14: Ratio Function (G), and Responsivities for the first two modes. (a) Doubly-Clamped beam. (b) Cantilever

Although we cannot determine the position of the particle using only two modes, we can still determine its mass if we use a DCB, thanks to the symmetry of the structure. For a doubly-clamped beam, the function $G(a)$ is symmetric with respect to the midpoint of the beam (Figure 14a). Thus if we were to define a relation G^{-1}, we would obtain two values for the position for a given argument of G^{-1}:

$$a_{1,2} = G^{-1}\left(\frac{\alpha_1\,\delta f_1}{\alpha_2\,\delta f_2}\right) \tag{42}$$

Since the DCB is symmetric, these two position values are equidistant to the center of the beam, Figure 15(a). When we plug in these values to the responsivity functions we see:

$$\phi_1(a_1)^2 = \phi_1(a_2)^2 \tag{43}$$

$$\phi_2(a_1)^2 = \phi_2(a_2)^2 \tag{44}$$

Now we can use equation (37) to calculate the corresponding values for mass:

$$\delta m_1 = \frac{\alpha_1\,\delta f_1}{\phi_1(a_1)^2}\ and\ \delta m_2 = \frac{\alpha_1\,\delta f_1}{\phi_1(a_2)^2} \tag{45}$$

From equation (43), we have $\phi_1(a_1)^2 = \phi_1(a_2)^2$, so equation 45 is reduced to: $\delta m_1 = \delta m_2$, i.e. both values for the position yield the same value for the mass. Obviously the same conclusion can be reached by considering the equations for the second mode, instead of the first mode. To sum up, the information from two modes gives two *different but symmetric* position values, but these position values yield *the same mass value*. We can also write down the value of the mass in closed form for the DCB: $\delta m = \frac{\alpha_1 \delta f_1}{\left(\phi_1\left(G^{-1}\left({}^{\alpha_1\delta f_1}/_{\alpha_2\delta f_2}\right)\right)\right)^2}$

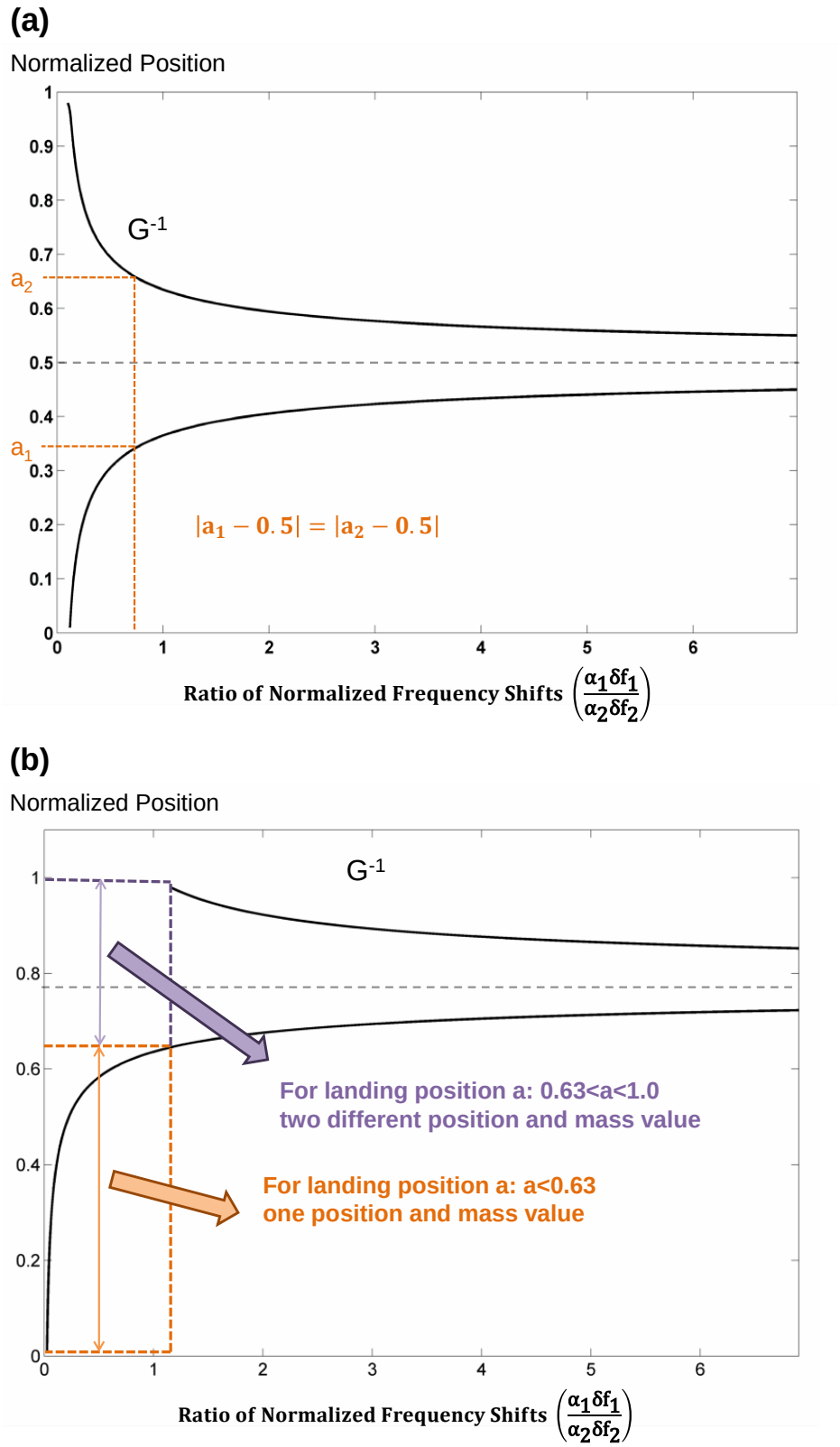

Figure 15: Inverse ratio functions, G^{-1}

(a) Doubly-Clamped Beam (b) Cantilever

Two-Mode Mass Detection: Beam and Cantilever Cases

The symmetry equations (43) and (44) hold for a doubly-clamped beam, but not for a cantilever. For this reason, two modes are sufficient for obtaining the mass information in the doubly-clamped beam case, but not in the cantilever case. For the beam case, the position variable still assumes two values (though they are symmetric with respect to the center). Thus for the doubly-clamped beam, we can obtain the mass of the particle and its distance to the center of the beam.

For the cantilever case, we cannot determine the mass of the particle from two frequency shifts alone because the mode shapes are not symmetric with respect to any point on the beam and there is no way to satisfy the equation $\phi_1(a_1)^2 = \phi_1(a_2)^2$ unless $a_1 = a_2$. Therefore, two different values for position are **guaranteed** to yield two different values for mass, in the case of cantilever. There is an exception when the particle lands between the clamping point and the first 63% of the length (i.e. $for\ 0 < a < 0.63$): then it is possible to use two-mode information to obtain the mass and position, as there is only one solution for the position within this range (Figure 15 b). However, this region is an insensitive region for cantilever measurements, as the mode shape (and displacement) is lower in this region. Finally, if we were to use three modes for the cantilever, it would be possible to infer the mass-position values along the device. However, the main concern is that higher modes are noisier, and the overall sensitivity level of the measurement suffers by using higher order modes.

3.3 Properties of the Mass-Position Transformation

We have shown that the frequency shift information from both modes, δf_1 and δf_2, can be used to calculate the mass δm of the particle, in addition to the two possible values for the longitudinal position, a_1 and a_2. We also have demonstrated that the two position values are equidistant to the center of the beam. In some sense, these two positions are equivalent to each other as far as the dynamics of the beam is considered. By symmetry, the physics does not change if the particle lands on the left or the right side of the center of the beam, as long as the landing positions are equidistant to the center. This symmetry would be a concern if we wanted to know where the particle had landed, but that goal is outside the scope of our work for now. We only need the distance of the particle to the center in order to calculate the quantity of interest, namely mass. Therefore, we can choose to work with only one of the two possible values of the position, as the other value would give the same result. For instance, we can narrow our attention to the first half of the beam, i.e. we work with the part of the beam extending between $0 < \eta < 0.5$. By selecting only one branch, we can treat the transformation, G, as a one-to-one transformation, from the frequency shift pair, $(\delta f_1, \delta f_2)$ to the mass-position pair $(\delta m, a)$, where a denotes the position value $(a_1 \; or \; a_2)$ whichever is smaller:

$$\mathrm{a} \equiv \min(a_1, a_2) \tag{46}$$

With this convention, we can summarize the transformation equations in the table below:

Transformation between the $(\delta f_1, \delta f_2)$ pair and the $(a, \delta m)$pair	
$\boldsymbol{\delta f_1} = \alpha_1\, \delta m\, \phi_1(a)^2$	$\boldsymbol{\delta f_2} = \alpha_2\, \delta m\, \phi_2(a)^2$
$\boldsymbol{a} = G^{-1}(\frac{\alpha_1\, \delta f_1}{\alpha_2\, \delta f_2})$	$\boldsymbol{\delta m} = \frac{\alpha_1 \delta f_1}{\left(\phi_1\left(G^{-1}\left(\alpha_1 \delta f_1 / \alpha_2 \delta f_2\right)\right)\right)^2}$

Using the equations above, we can visualize the transformations between different variables. These two frequency shifts define a two-dimensional plane; henceforth this plane will be denoted as the $|\delta f_1| - |\delta f_2|$ plane. For convenience we will use the absolute values of the frequency shifts when working in the $|\delta f_1| - |\delta f_2|$ plane. We will now determine how the position variable, a, changes in this plane. From the expression: $a = G^{-1}(\frac{\alpha_1\, \delta f_1}{\alpha_2\, \delta f_2})$ it is obvious that if both of the frequency shifts are multiplied by the same number, their ratios and the argument of the G^{-1}function will still be the same, so a will not change. Therefore the contours of constant position in the $|\delta f_1| - |\delta\, f_2|$ plane are straight lines passing through origin. The slope of these lines determines the value of a (Figure 16 (a)).

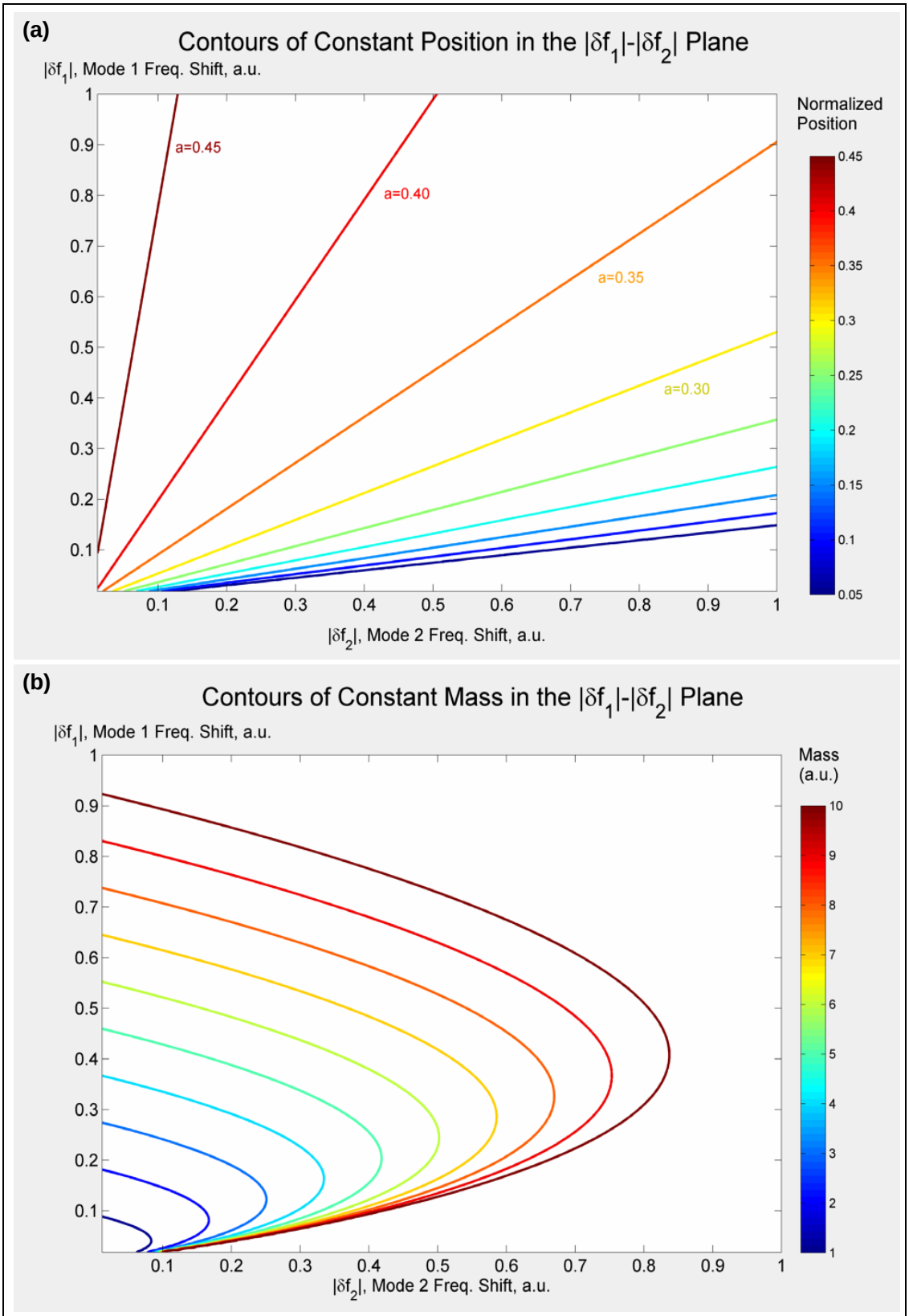

Figure 16: Contours in δf_1-δf_2 Plane

(a) Contours of constant position are straight lines passing through the origin.
(b) Contours of constant mass. The contour levels increase linearly.

Similarly, we can use the expression for mass to trace out the contours of constant mass in the $|\delta f_1| - |\delta f_2|$ plane. These contours are shown in Figure 16 (b).

We can also switch to the mass-position plane. The amount of frequency shift in this coordinate system is described by the original mass loading equations, (36). These contours are shown in Figure 17, for the first and second modes of a DCB.

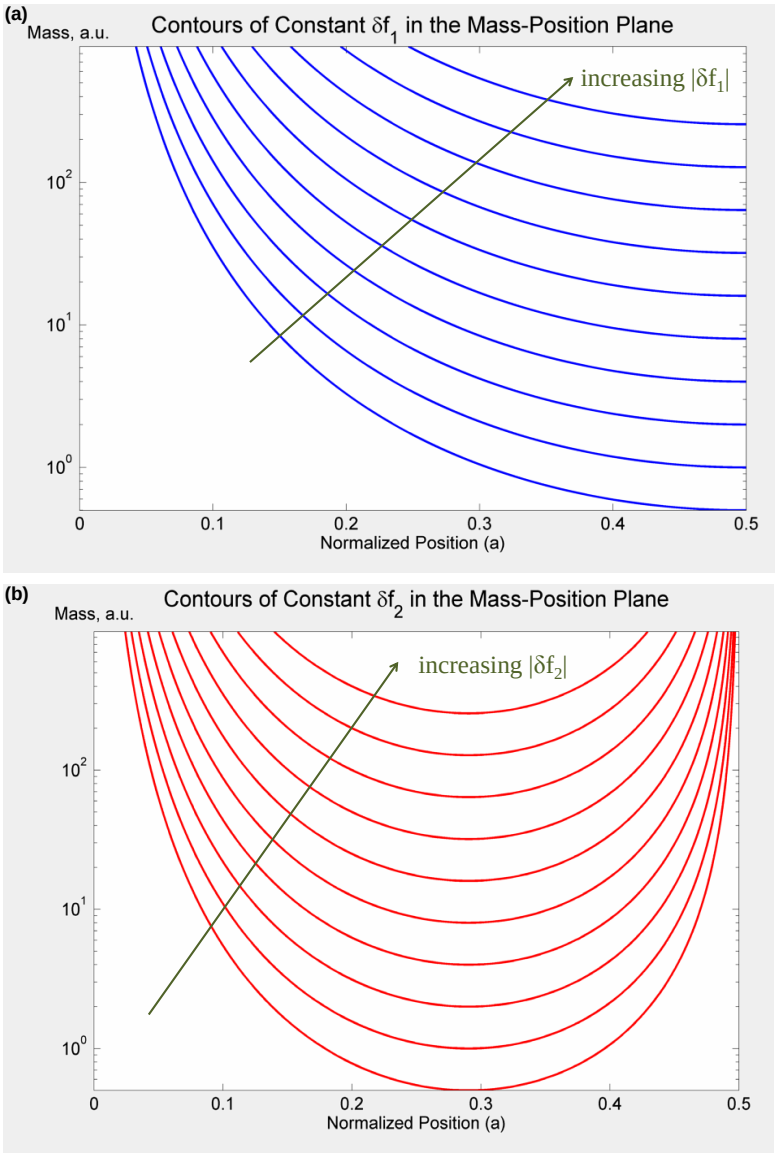

Figure 17: Frequency shift contours in mass-position plane

(a) Mode 1 and (b) Mode 2
Contour levels increase logarithmically: adjacent levels have factor of two differences. The mass axis is plotted logarithmically.

3.4 Modeling Frequency Noise

As shown in section 3.2, the mass of a particle can be determined by measuring the frequency shifts in the two modes of a DCB. We are interested to know not only the value of the mass, but also the error level in the determination of the mass. This uncertainty in mass depends on the frequency noise of the resonator. Therefore, we will first discuss how to model the frequency noise in a way suitable for mass-error calculations. In this section, we will first discuss the conventional measure of frequency noise, the Allan variance, and then discuss a broader measure for dispersion, the probability density for frequency noise.

First, we consider a discrete time-series measurement of NEMS frequency, f:

$$f[n]: the\ value\ of\ the\ measured\ frequency\ at\ time\ step\ n$$

During the measurement we took N samples. We can calculate the basic statistical quantities for this experiment, for instance the mean frequency, $\bar{f}$:

$$\bar{f} = \frac{1}{N}\sum_{n=1}^{n=N} f[n] \tag{47}$$

We can also calculate the standard deviation σ_{std}, and the standard variance σ_{std}^2 :

$$\sigma_{std}^2 = \sum_{n=1}^{n=N} \left(f[n] - \bar{f}\right)^2 \tag{48}$$

Usually we use the standard deviation to describe the dispersion of a statistical variable. However for frequency measurements, the standard deviation happens to be a poor measure to quantify dispersion, because it depends on the sample size (N) and it does not

converge for certain type of noise commonly encountered in experiments like Flicker Noise or Random Walk Noise [36].

A better measure to characterize the frequency noise is the Allan deviation. To calculate the Allan deviation, we first consider the fractional frequency difference, y[n]:

$$y[n] = \frac{f[n] - f_0}{f_0} \tag{49}$$

Here f_0 is the nominal frequency of the resonator. Thus the $y[n]$ parameters are similar to the frequency, they are normalized after a constant offset is subtracted. With this convention, the Allan variance σ_{Allan}^2 is defined as:

$$\sigma_{Allan}^2 \equiv \frac{1}{2(N-1)} \sum_{n=1}^{n=N-1} (y[n+1] - y[n])^2 \tag{50}$$

So to calculate Allan deviation, we use *the difference of the adjacent terms*, rather than *the difference from the mean*. In this way, drift terms in the noise power spectra do not cause the variance to blow up. Also the Allan deviation is normalized by the sample size, so that measurements with different numbers of data points can be compared directly.

The frequency stability of a resonator depends also on the timescale. For example, one resonator may be very stable for short periods of time, but it may drift strongly when observed at longer time scales. This kind of dependence on the time-scale can be incorporated into the Allan Variance as well. The Allan variance definition above is calculated for the fastest time scale, i.e. the sampling bandwidth, of the measurement.

If we want to calculate the Allan variance at a longer timescale, we can use two different techniques: non-overlapping and overlapping Allan variances. To calculate the non-overlapping Allan variance, we first slice the data into pieces having the size of the

relevant timescale (Figure 19a). Next, we calculate the average of each piece, and calculate the Allan variance for an ensemble composed of these averaged values. For instance, if the timescale of interest is τ, such that $\tau = q\, T_{Sampling}$ with q being some integer, then:

$$\sigma^2_{Allan}(\tau) = \frac{1}{2(M-1)} \sum_{m=1}^{M} \left(\overline{y[m+1]} - \overline{y[m]}\right)^2 \tag{51}$$

Here $\overline{y[m]}$ shows the average value of the fractional frequency difference, during the time interval denoted by m. Also $M = N/q$, since we slice a total of N data points into segments containing q data points.

The other method for calculating the Allan variance, the overlapping Allan variance, uses the data more efficiently. In this case the data is also sliced into pieces of the same size, however there are many more pieces as the pieces are allowed to overlap with each other. The important differences between the two types of Allan variances are: the non-overlapping variance has all of the elements statistically independent from each other, whereas the overlapping variance is a better estimator in some cases. We will work with the independent (non-overlapping) Allan variance for mathematical convenience.

As we saw above, the Allan variance is a scalar parameter that characterizes the frequency noise, but it does not contain all the information. We can represent more information if we work with the probability density function (**PDF)** of the frequency noise. The PDF of a statistical variable x is denoted as PDF_x, and defined as:

$PDF_x(x = x')dx'$:The probability of x having a value between x' and x'+dx' (52)

Our first goal is to estimate the PDF of the frequency noise from the experimental data. After measuring the fractional frequency difference, $y[n]$, we can try to fit the resulting ensemble within a typical PDF model. A Gaussian distribution seems to be sufficient to model the frequency noise in our experiments. As expected the variance in the Gaussian distribution has a value similar to the Allan variance.

For example, we consider the time trace of an actual measurement (04jan10ac.txt) in Figure 18 (a). The calculated fractional frequency differences are shown in figure Figure 18 (b). As can be seen there, the Gaussian fit is good, with the following parameters:

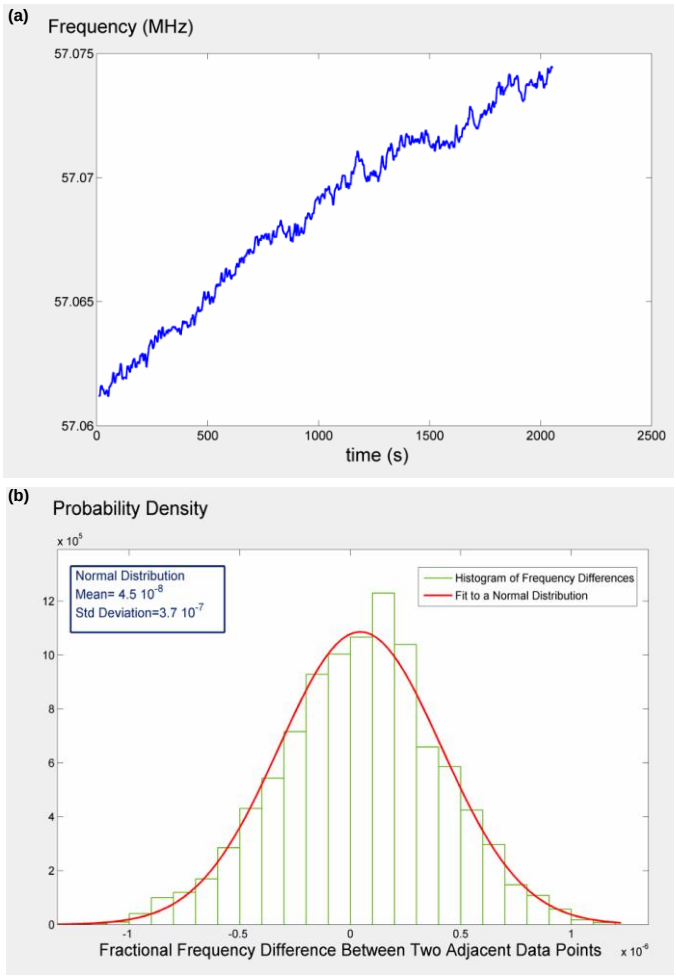

Figure 18: Modeling frequency noise

(a) Frequency vs. Time for a single mode PLL run
(b) The distribution can be fitted into a Gaussian. Note that the mean is positive as expected from the upward drift.

$$PDF_{\delta f}(\delta f = x)dx = \frac{1}{\sqrt{2\pi}} e^{\frac{(x-\mu)^2}{\sigma^2}} \text{ with } \mu = 4.5 \times 10^{-8} \text{ and } \sigma = 3.7 \times 10^{-7}$$

The PDF above is valid for the frequency instability at the fastest timescale (400 ms in this case). However when a protein landing event occurs, the PLL responds with a certain time scale, usually ten times the sampling time. Hence we need to use the PDF of the frequency stability at the PLL timescale. We need to proceed in a manner similar to the calculation of the non-overlapping Allan Variance: we can slice the data into segments of length equal to the PLL timescale, and use the averages of these segments for the PDF modeling.

Now we estimate the PDF of the frequency noise at the PLL timescale for the same example below. From independent measurements, the PLL response time is 9 seconds, corresponding to a span of 22 data points. Thus $\tau = 22 \times T_{sampling}$ and we need to slice the data into segments of width 22 and calculate the average frequency for each segment. The distribution of the frequency noise for this timescale seems to be a normal distribution as before, and the PDF is:

$$PDF_{\delta f}(\delta f = x)dx = \frac{1}{\sqrt{2\pi}} e^{\frac{(x-\mu)^2}{\sigma^2}} \text{ with } \mu = 9.8 \times 10^{-7} \text{ and } \sigma = 3.6 \times 10^{-6} \quad (53)$$

The mean value for the PDF at the PLL timescale is about 22 times the mean value of the PDF at the sampling bandwidth, as the former contains 22 data points of the latter. The above form passes the χ^2 test with a p-value of 0.86. Hence we can safely use the normal distribution to model this noise process.

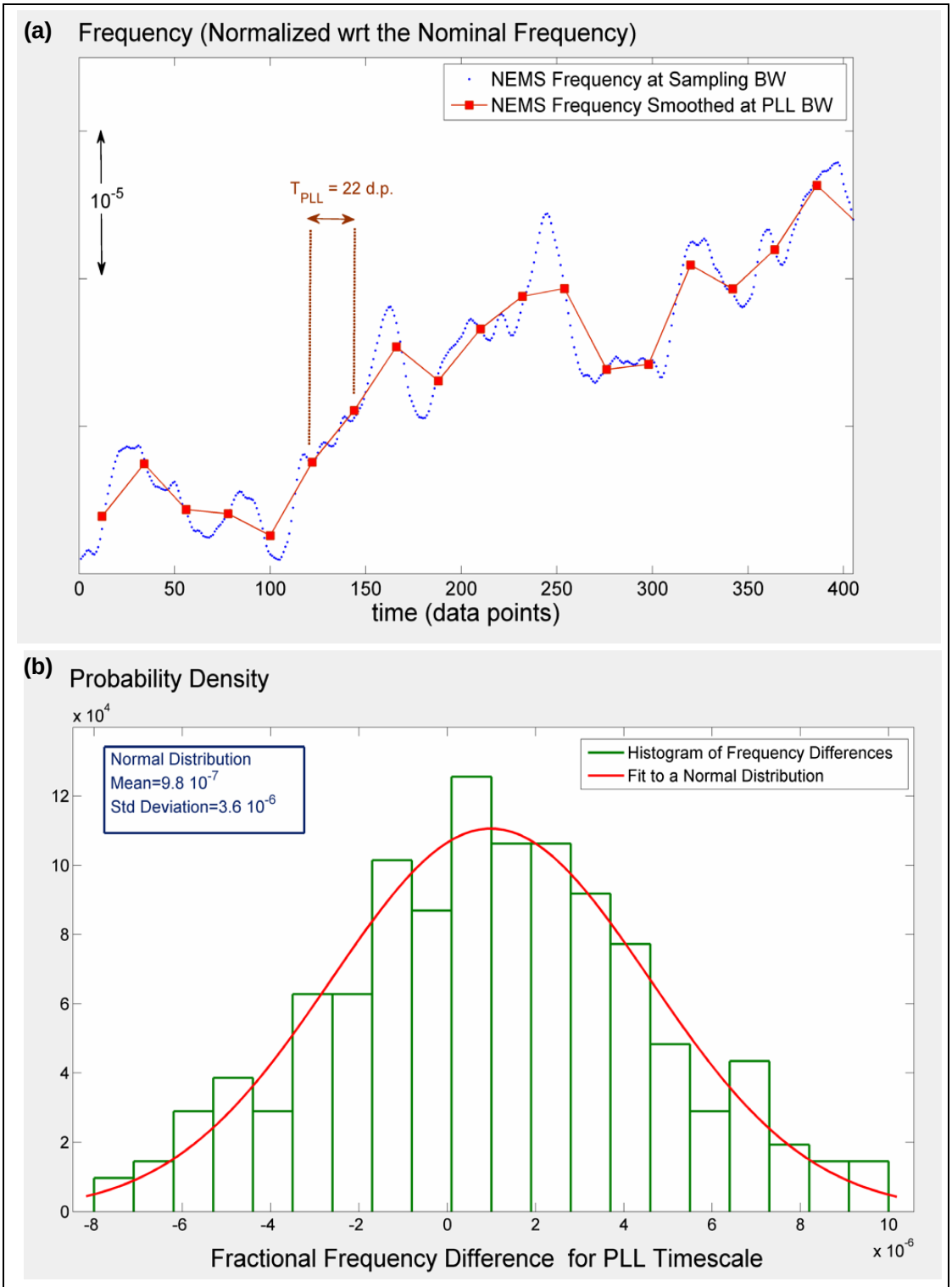

Figure 19: Frequency noise analyses at the PLL time scale

(a)Segmentation of the data into pieces with the timescale of PLL, and subsequent averaging
(b) Fitting of the PLL scale frequency variation to a normal distribution.

3.5 Frequency Jumps as Statistical Variables

In the last section, we modeled the frequency noise using probability density functions. In this section, we will shift our attention to the frequency jumps. We will model them as statistical variables by taking the frequency noise into account. Using this modeling, we will be able to calculate the mass errors in the next section.

Every frequency jump measurement should be reported with the frequency noise of the setup. To give an example with arbitrary numbers, we usually report frequency jumps in the format: $\boldsymbol{\Delta f = 750\ Hz \pm 50\ Hz}$, where $\boldsymbol{750\ Hz}$ is the magnitude of the frequency shift and $\boldsymbol{\pm 50\ Hz}$ is the frequency noise in the experiment, represented here as a simple number. However we will need to use a continuous, rather than a scalar, model for the frequency noise to calculate the uncertainties in mass. Hence we will first discuss how to incorporate the continuous noise model (the frequency noise PDF) into the representation of a frequency jump. Later, we will discuss how to represent the noise from two modes, jointly, using a two-dimensional probability density function. We will use this 2-D probability density to model a particle landing event with two-mode frequency jumps as a 2-D statistical variable.

When a particle lands on the beam, we measure a frequency shift. This *measured frequency shift* contains some amount of *frequency noise* that degrades the measurement. If there had been no *frequency noise*, then the *measured frequency shift* would have corresponded to the theoretical value of the frequency shift due to particle landing, which we refer as the *ideal frequency shift*:

$$\Delta f_{ideal} \equiv -\alpha\, \phi(a)^2\, \delta m \tag{54}$$

$$\Delta f_{measured} = \Delta f_{ideal} + \tilde{f}_{noise} \tag{55}$$

Again, Δf_{ideal} represents the frequency shift that would have been measured if there were no intrinsic or extrinsic noise in the setup. The term $\tilde{f}_{noise}$ denotes the frequency noise term in the measurement. We only know the statistical description of the frequency noise. Our best estimate for *the ideal frequency shift* ($\Delta f_{estimate}$) is:

$$\Delta f_{estimated} = \Delta f_{measured} - \tilde{f}_{noise} \tag{56}$$

This estimate for the frequency jump can be treated as a random variable (Figure 20).This random variable is centered at the measured frequency jump and has the same statistical distribution as the frequency noise; Figure 20 (b) illustrates this statement. The translation of the PDF illustrated in Figure 20 can be written mathematically as:

$$PDF_{jump}(\Delta f) = PDF_{noise}(\Delta f - \Delta f_{measured}) \tag{57}$$

Here $PDF_{jump}(\Delta f)$ denotes the probability distribution of the new statistical variable, *the frequency jump,* calculated at some value for frequency change, Δf. On the right hand side, $PDF_{noise}(\Delta f - \Delta f_{measured})$ denotes the probability distribution of the *frequency noise* calculated for the frequency change value of $\Delta f - \Delta f_{measured}$. The equation above simply states that when we measure a frequency shift, we can represent it statistically by translating the frequency noise PDF by the amount of the frequency shift. Notice that if the signal-to-noise ratio of the measurement is good, then this new random variable is sharply concentrated around the measured frequency shift. The main reason for such a

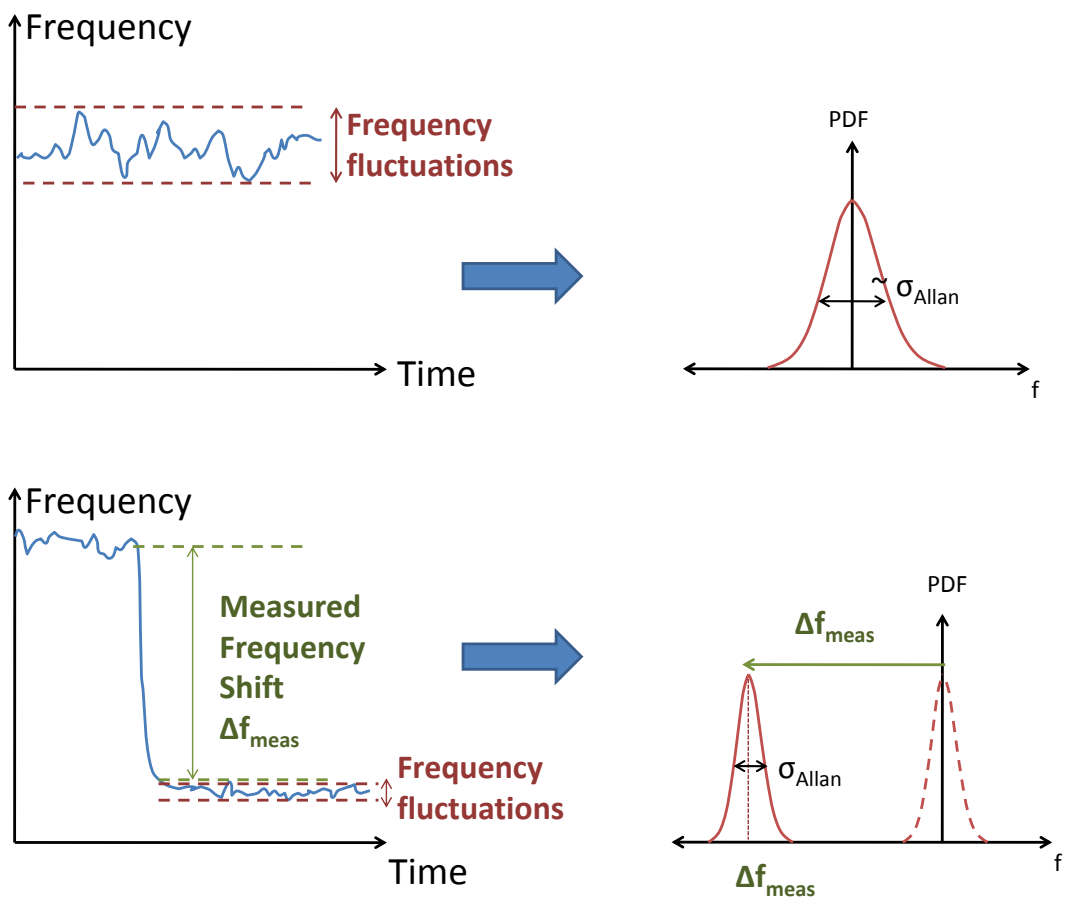

Figure 20: Frequency jump modeled as a random variable

Representation of the frequency noise and a frequency shift in the presence of noise. In (a), a time trace of frequency fluctuations is recorded and this is used to calculate the probability density function for the frequency noise. The width of this distribution is roughly the classic Allan variance for this mode. In (b), a frequency shift caused by particle landing is represented as a random variable, with its center determined by the frequency jump and a small spread due to frequency noise.

simple transformation is that we do not have any prior information about the statistical nature of the frequency jumps. This result can be obtained formally through the inverse probability theorem (i.e. Bayes' theorem) [37] and is shown in APPENDIX B:.

Representation of Two Variables

In this way, we can represent the frequency shifts as statistical variables. When we want to go from single-mode measurements to two-mode measurements, we will have to use

two different frequency noise statistics for these two modes. The statistical information of two variables can be represented with the *joint probability density function*, $JPDF$ defined as:

$$\boldsymbol{JPDF_{X,Y}(x = x', y = y')dx'\delta y'}\text{: The probability of}$$

$$x \text{ having a value between } x' and\ x' + dx', \textbf{AND}, y \text{ having a value between } y' and\ y' + dy'$$

If the frequency noise of the two modes were statistically independent from each other, then the joint PDF would simply be: $JPDF_{\delta f_1,\delta f_2} = PDF_{\delta f_1} \times PDF_{\delta f_2}$. However, there is usually some correlation between the frequency noises; therefore the JPDF needs to include this correlation. For the two mode data we obtained in our experiments, a bivariate Gaussian distribution works satisfactorily. A joint Gaussian distribution for the frequency noise of the two modes is described mathematically in the following form:

$$JPDF_{\delta f_1,\delta f_2}(\delta f_1, \delta f_2) = \frac{1}{2\pi\sigma_1\sigma_2\sqrt{(1-\rho^2)}} exp\left(-\frac{z}{2(1-\rho^2)}\right) \quad (58)$$

where

$$z \equiv \frac{(\delta f_1 - \mu_1)^2}{\sigma_1^2} - \frac{2\rho(\delta f_1 - \mu_1)(\delta f_2 - \mu_2)}{\sigma_1\sigma_2} + \frac{(\delta f_2 - \mu_1)^2}{\sigma_2^2} \quad (59)$$

Here δf_1 and δf_2 represent the normalized frequency shifts in the first and second modes respectively. μ_1 and μ_2 are the mean values for frequency fluctuations. The symbols σ_1 and σ_2 represents the standard variances of the two modes. The symbol ρ shows the correlation coefficient between the two variables.

We may illustrate the above formula by working out an example case. Figure 21 (a) shows the time trace of two modes. In this case, the two modes are highly correlated so the overall frequency behavior looks very similar for the two modes. The scattered dots

on Figure 21 (b) represent the fractional frequency noise in both of the modes, using a PLL time-window. The contour map shows the fit to a two-variable Gaussian.

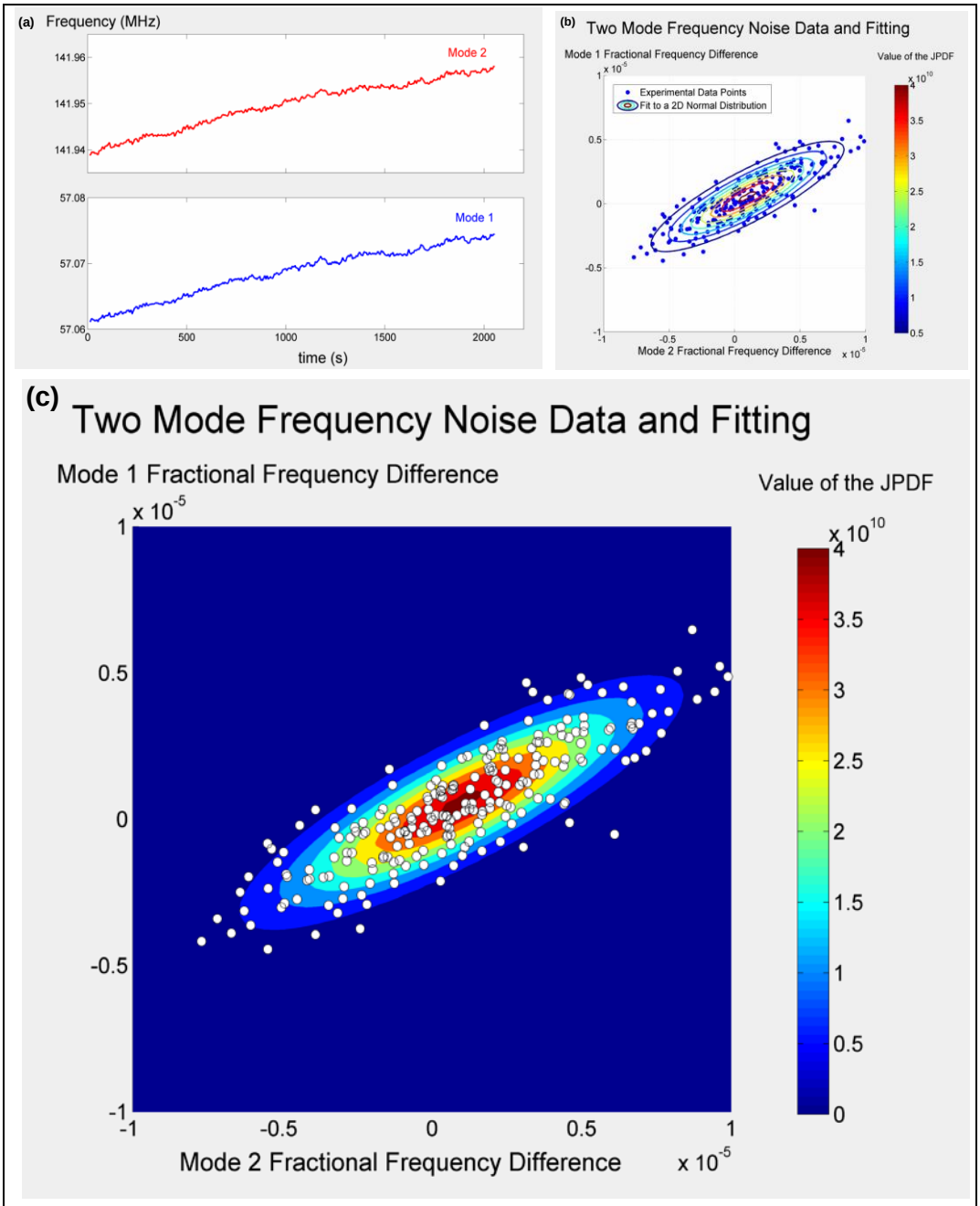

Figure 21: Two mode frequency noise modeling

(a) Time trace of the two modes.
(b) Fit of the two-dimensional frequency noise to a bivariate Gaussian joint probability density. Each scatter points show an experimental data point of the frequency noise. The contour lines show at various levels. The shape and orientation of the contours depend respectively on the relative noise levels of the modes and the correlation between the modes. The maximum of the fit is slightly away from the origin because of the systematic drift of the frequencies during the experiment.
(c) The same with (b), a different visualization is used to illustrate the scatter points better. The colormap shows different levels of the Gaussian fit.

The parameters of fitting in this particular run was :

$\mu_1 = 9.8 \times 10^{-7}$ $\mu_2 = 5.7 \times 10^{-7}$, $\sigma_1 = 3.5 \times 10^{-6}$, $\sigma_2 = 2.1 \times 10^{-6}$, $\rho = 0.91$

Once we have modeled the two-mode frequency noise with the JPDF formalism above, we can represent the frequency jumps using this JPDF, in a similar way we did for the single mode case. A frequency jump due to particle landing can be represented by a displacement of the noise JPDF by the vector formed by the two frequency shifts, as shown in Figure 22. Once we measure frequency shifts $\delta f_1'$ and $\delta f_2'$ then the JPDF describing this event has the same form as equation (58) with the substitutions:

$$\mu_1 \to \mu_1 + \delta f_1' \text{ and } \mu_2 \to \mu_2 + \delta f_2' \tag{60}$$

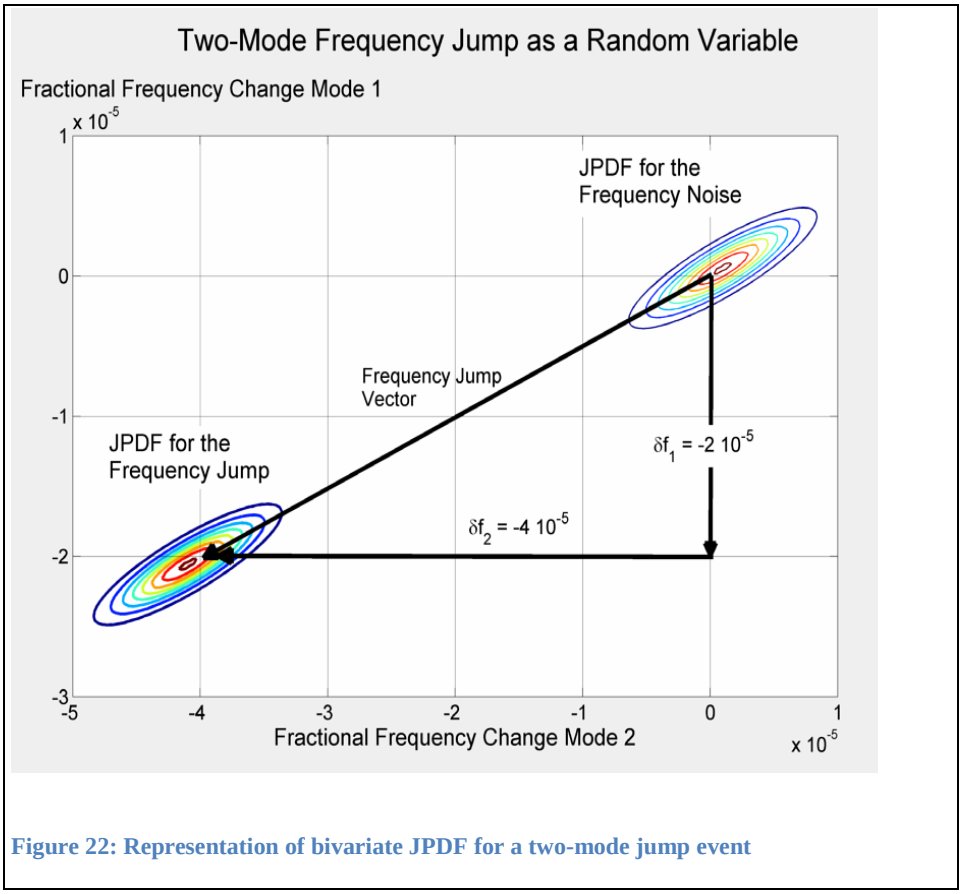

Figure 22: Representation of bivariate JPDF for a two-mode jump event

3.6 Mass-Position Error

So far we have covered how to model frequency noise and frequency jumps as statistical variables; we are now in a position to calculate the errors in the determination of the mass of a particle landing on the NEMS device. As we have seen previously there is a transformation between the frequency shifts and mass-position variables ($\delta f_1 - \delta f_2 \leftrightarrow \delta m - a$). We will utilize this relationship for calculating mass errors; as an added bonus, we will also be able to calculate the error in the position variable, a, as defined in (46).

First, we recall equation (40):

$$G(a) = \frac{\alpha_1\, \delta f_1}{\alpha_2\, \delta f_2} \Longrightarrow a = G^{-1}\left(\frac{\alpha_1 \delta f_1}{\alpha_2 \delta f_2}\right) \quad (within\ a\ domain\ where\ G(x) is\ invertible) \tag{61}$$

As mentioned previously, the function G(x) is not one-to-one generally, and it is not possible to find the inverse function of G(x) for the whole domain of transformation. Yet, we can define sub-domains where G(x) is invertible, and in this way we can obtain one solution for a mass-position pair in every sub-domain. If the nano-mechanical structure is a doubly-clamped beam, then the symmetry ensures that the solutions for the two sub-domains have the same mass values (and symmetric position values with respect to the center of the beam).

Once we select one of the sub-domains with which to work and determine the statistical description of the frequency shifts, we are ready to calculate the uncertainties for mass and position.

For a given frequency jump event, we know how to obtain a joint probability distribution function for the two modes, $PDF_{\boldsymbol{\delta f_1,\delta f_2}}(\delta f_1, \delta f_2)$. Now these two variables, δf_1 and δf_2, can be mapped into two variables, mass and position – δm and a. Thus, we expect to start with the JPDF for the frequency jumps and end up with the joint-PDF for mass and position, $JPDF_{\boldsymbol{\delta m,a}}(\delta m, a)$. This kind of transformation is called a bivariate PDF transformation[38] and is given by:

$$\mathrm{PDF}_{\mathbf{\delta m,a}}(\delta \mathrm{m}, \mathrm{a}) = |\mathbf{J}| \times \mathrm{PDF}_{\delta \mathrm{f}_1, \delta \mathrm{f}_2}(h_1(\delta m, a), h_2(\delta m, a)) \tag{62}$$

Here $h_1(\delta m, a)$and $h_2(\delta m, a)$are the functional forms for δf_1 and δf_2, respectively (e.g. $\delta f_1 = h_1(\delta m, a)$). Thus, from (37) and (38) we have: $h_1(\delta m, a) = \delta m\, C_1(a)^2 / \alpha_1$ and $h_2(\delta m, a) = \delta m\, C_2(a)^2 / \alpha_2$. **J** denotes the Jacobian matrix, and |**J**| is the positive determinant of the matrix:

$$|\mathbf{J}| = abs\left(\frac{\partial h_1}{\partial(\delta m)}\frac{\partial h_2}{\partial a} - \frac{\partial h_2}{\partial(\delta m)}\frac{\partial h_1}{\partial a}\right) \tag{63}$$

Using this formalism and previous results for the PDF of the frequency shifts, we can calculate the joint-PDF for the mass and position:

$$PDF_{\boldsymbol{\delta m,a}}(\delta m, a) = |\mathbf{J}| \times \frac{1}{2\pi\sigma_1\sigma_2\sqrt{1-\rho^2}} \exp\left(-\frac{\Gamma}{2(1-\rho^2)}\right) \tag{64}$$

$$|\mathbf{J}| = \frac{2\delta m}{\alpha_1\alpha_2}[C_1(a)C_2(a)]\left|\frac{\partial C_1}{\partial \eta}\right|_{\eta=a} C_2(a) - \left.\frac{\partial C_2}{\partial \eta}\right|_{\eta=a} C_1(a)\Bigg| \tag{65}$$

$$\Gamma = \frac{\left(\frac{\delta m C_1(a)^2}{\alpha_1} + \mu_1\right)^2}{\sigma_1^2} - \frac{2\rho\left(\frac{\delta m C_1(a)^2}{\alpha_1} + \mu_1\right)\left(\frac{\delta m C_2(a)^2}{\alpha_2} + \mu_2\right)}{\sigma_1\sigma_2} + \frac{\left(\frac{\delta m C_2(a)^2}{\alpha_2} + \mu_2\right)^2}{\sigma_2^2} \tag{66}$$

Here μ_1 and μ_2 are the frequency shifts measured in the first and second modes respectively, after the drift terms are accounted for as in equation (60).

Once we have obtained this expression, we can process the experimental data numerically, and convert a frequency jump into a joint PDF for mass and position. We can project this two-dimensional PDF on either the mass or the position axis to determine the distribution of position or mass respectively:

$$\mathrm{PDF}_{\boldsymbol{\delta m}}(\delta \mathrm{m}) = \int_{\mathrm{a}=0}^{\mathrm{a}=0.5} \mathrm{PDF}_{\boldsymbol{\delta m,a}}(\delta \mathrm{m}, \mathrm{a})\, da \tag{67}$$

$$\mathrm{PDF}_{\mathbf{a}}(\mathrm{a}) = \int_{\delta \mathrm{m}=0}^{\delta \mathrm{m}=\infty} \mathrm{PDF}_{\boldsymbol{\delta m,a}}(\delta \mathrm{m}, \mathrm{a})\, dm \tag{68}$$

To give an idea about how this transformation works, we consider the frequency jump event described above in figure Figure 22, with normalized frequency shifts: $\delta f_1 = -2\ 10^{-5}$ and $\delta f_2 = -4\ 10^{-5}$. The variance for the first mode was $3.5\ 10^{-6}$ and the second mode was $2.1\ 10^{-6}$. The mass of the beam in this case was 430fg. Using a single mode estimate, the first mode gives a mass of 4.5 MDa and the second mode gives a mass of 9.5 MDa, for the mass of the particle. Single mode estimates are always lower-bound estimates for mass, because these estimates assume that the particle lands on the most responsive point on the beam. Furthermore the Allan variances gives 0.8 MDa and 0.5 MDa for the uncertainties in the mass for the first and second modes, respectively. This single mode analysis does not give the correct answer but is useful to obtain rough estimates.

The transformation of this event to mass-position coordinates is shown in figure Figure 23 (A). Here, the shape of the JPDF is determined by the form of the mode shapes near that particular position. The mass inferred from the multimode method is 10 MDa and

1σ uncertainty range for the mass is 1 MDa. That is $\Delta m = 10MDa \pm 0.5MDa$ for the event described by the frequency jumps in Figure 22. We can further infer that the position of the particle is about $a = 0.3 \pm 0.03$; or more accurately, the particle lies within the 27% and 33% of the beam away from one of the clamping points, with a confidence level of 68%. In figure Figure 23 (b), we represent the same event in the frequency-frequency domain. The mass and position of the particle can be determined by referring to the constant-mass and constant-position contour lines. This representation can be used to determine the mass of the particle more quickly, and may be more suitable for on-line data processing with limited computation power.

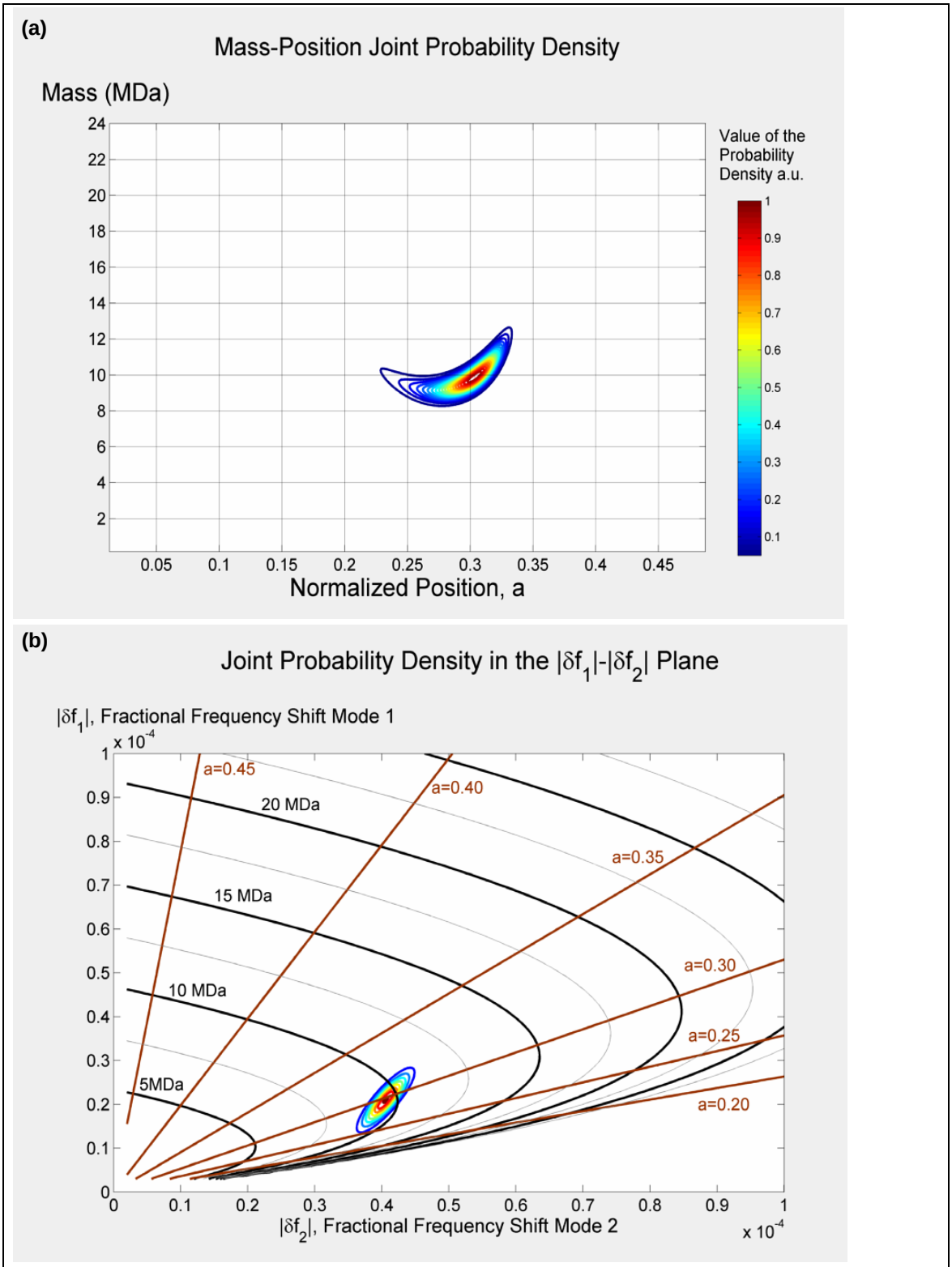

Figure 23: Mass-Position Errors

Uncertainties in the mass and position values inferred for a nano-particle landing event. The shape of the ellipsoid is determined by the correlations between the two modes and also the mode shapes at the projected position through the Jacobian term.

3.7 Further Considerations

3.7.1 Mass Resolution vs. Position in Doubly-Clamped Beam

In this subsection, we will explore the trend in mass resolution for different landing points on the beam. We could have obtained this by integrating the 2-D PDF shown in equation (67); however the analytical form becomes intractable. Therefore, we are going to calculate the numerical value of mass resolution for certain position values and present this trend to determine how the mass resolution changes within the beam.

In Table 3 below, we report the results for different positions at different values of Allan variances and correlation coefficients. The JPDF for the frequency noises are assumed to be Gaussian as before. In Figure 23, mass resolution versus position is plotted for equal Allan variances and different correlations in the two modes. The high-correlation case, with approximately equal Allan variances, has been the most commonly encountered situation in our experiments.

From the table, mass resolution worsens as the correlation coefficient between the modes increase. This is expected, as the independent information contained in the two-mode data decreases as the correlation increases. Another trend we see is that the resolution is almost constant in most cases in the table for $a \geq 0.35$, and in most *practical* cases for $a \geq 0.3$. Therefore we conclude that *about 40% of the beam area is usable for mass spectrometry* without significant decrease in the mass resolution.

Mass Resolution Under the Noise Conditions Stated and at the Position Shown								
Condition			**Position**					
Allan Variance mode 1	**Allan Variance mode 2**	**Correlation coefficient**	**0.2**	**0.25**	**0.30**	**0.35**	**0.40**	**0.45**
$\sigma_1=4\ 10^{-7}$	$\sigma_2=4\ 10^{-7}$	ρ=0.0	$7.2\ 10^{-6}$	$1.0\ 10^{-6}$	$3.2\ 10^{-7}$	$3.2\ 10^{-7}$	$3.2\ 10^{-7}$	$3.2\ 10^{-7}$
$\sigma_1=4\ 10^{-7}$	$\sigma_2=4\ 10^{-7}$	ρ=0.45	$6.5\ 10^{-6}$	$7.9\ 10^{-7}$	$3.8\ 10^{-7}$	$4.1\ 10^{-7}$	$4.1\ 10^{-7}$	$4.1\ 10^{-7}$
$\sigma_1=4\ 10^{-7}$	$\sigma_2=4\ 10^{-7}$	ρ=0.90	$7.9\ 10^{-6}$	$5.6\ 10^{-7}$	$5.6\ 10^{-7}$	$6.8\ 10^{-7}$	$6.5\ 10^{-7}$	$6.2\ 10^{-7}$
$\sigma_1=4\ 10^{-7}$	$\sigma_2=4\ 10^{-6}$	ρ=0.0	$1.6\ 10^{-5}$	$8.2\ 10^{-6}$	$3.3\ 10^{-6}$	$1.9\ 10^{-6}$	$1.4\ 10^{-6}$	$9.1\ 10^{-7}$
$\sigma_1=4\ 10^{-7}$	$\sigma_2=4\ 10^{-6}$	ρ=0.90	$1.8\ 10^{-5}$	$1.0\ 10^{-5}$	$5.1\ 10^{-6}$	$3.3\ 10^{-6}$	$2.3\ 10^{-6}$	$1.6\ 10^{-6}$
$\sigma_1=4\ 10^{-6}$	$\sigma_2=4\ 10^{-7}$	ρ=0.0	$1.0\ 10^{-5}$	$9.8\ 10^{-6}$	$5.7\ 10^{-6}$	$2.6\ 10^{-6}$	$3.1\ 10^{-6}$	$3.1\ 10^{-6}$
$\sigma_1=4\ 10^{-6}$	$\sigma_2=4\ 10^{-7}$	ρ=0.90	$8.8\ 10^{-6}$	$9.0\ 10^{-6}$	$6.7\ 10^{-6}$	$4.3\ 10^{-6}$	$4.7\ 10^{-6}$	$4.9\ 10^{-6}$
$\sigma_1=4\ 10^{-6}$	$\sigma_2=4\ 10^{-6}$	ρ=0.0	$1.1\ 10^{-5}$	$1.1\ 10^{-5}$	$7.1\ 10^{-6}$	$3.4\ 10^{-6}$	$3.3\ 10^{-6}$	$3.2\ 10^{-6}$

Table 3: Mass Resolution vs Position for a DCB

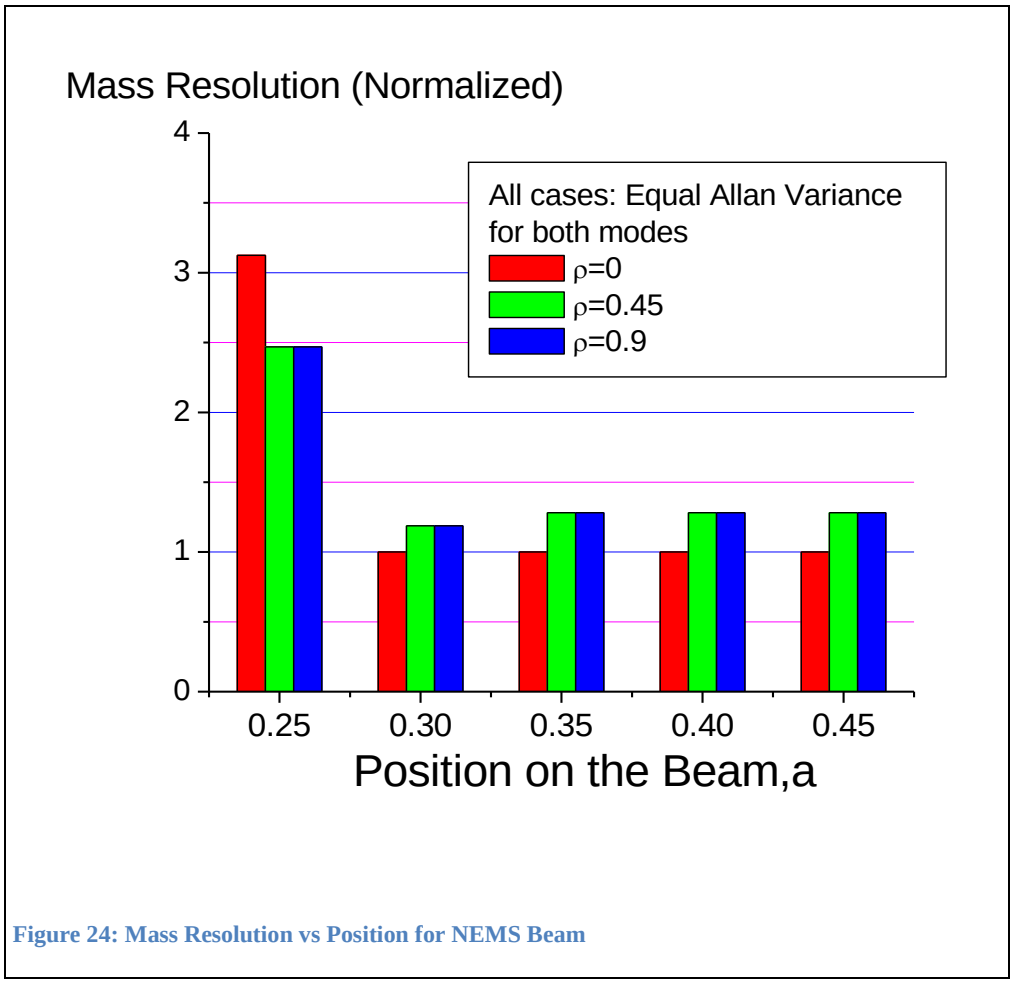

Figure 24: Mass Resolution vs Position for NEMS Beam

3.7.2 Effects of Tension

In our analysis, we neglected the effect of tension, both in single mode and multimode cases. Tension changes the results obtained so far in two ways. First, tension changes the the natural frequency of the resonator and the frequency shift due to mass loading. However, the ratio of these two quantities stays the same, and the mass value obtained from the calculation does not change. Secondly, tension changes the mode shapes, but this change is small enough to be neglected.

When there is a tension on the beam, the natural frequency of the beam is modified. This modification comes about because the tension term contributes to the potential energy of the system, basically modifying the effective spring constant k_{eff}. This change in the effective spring constant will change the natural frequency of the resonator. However, the mass loading mechanism will still be the same, as it originates from the kinetic energy term. Tracing the calculation in chapter 2, we see that the basic equation $\Delta m\, \phi(a)^2 = -2M_{eff}\frac{\Delta\omega}{\omega}$ will still hold. In this equation, the natural frequency and the frequency shift will change due to tension. However, the ratio $\Delta\omega/\omega$ will still correspond to the mass change of the resonator. And since we use this ratio in our calculations, the measured mass is not affected by tension.

The other effect of tension is to modify the mode shapes slightly. It is instructive to think about this in two limiting cases. The first limiting case happens when tension goes to zero. This limit is called *the beam limit* and we have been performing our calculations in the beam limit so far. We saw that the mode shapes are composed of hyperbolic sine, hyperbolic cosine, sine, and cosine functions. In the other limiting case, tension

dominates over the beam flexure. This limit is called *the string limit* and the mode shapes in this limit are sine and cosine functions.

The mode shapes in both cases are not too different from each other, especially in the most sensitive, center region of the beam. When we have comparable strengths of beam flexure and tension, then the mode shape will be a hybrid of the two shapes, the beam-limit mode shape and the string-limit mode shape. We can calculate a worst-case scenario for the position error by calculating the differences we would obtain from the beam-limit and the string-limit for the same data. This difference is shown in Figure 25. Most error happens near the edges, but this region is also the less sensitive region anyways. Near the center of the beam, the difference between the beam and string limits diminishes. We should note that the mass error can be obtained from the positional error obtained and the basic equation for the frequency shift due to point mass loading, and it follows a similar trend.

In a real experiment, the error due to tension would be much smaller than what is depicted here, as the beam flexure is still larger than the tension in our experiments. For any given experimental condition, it is best to determine the relevant mode shapes by finite-element simulations, and use these shapes in the calculations.

Figure 25: Worst Case Error for Position When Neglecting Tension

3.7.3 Effects of Simultaneous Excitation of Multiple Modes

In our analysis we assumed that the frequency shift for a mode is the same whether only that mode is driven or whether other modes are driven simultaneously. We will discuss the influence of multiple modes excited simultaneously.

Two effects modify the results obtained so far. The first effect is termed **kinematical effect** and occurs because the added particle's motion follows a superposition of the modes present. As a result, the kinetic energy contribution of the particle is more than what it would be when the cases are treated separately and summed up. In APPENDIX C: we calculate the correction to the frequency shift due to this effect, and show that it is a second order effect and it is safe to neglect it.

The other effect is termed the **tensing effect** and occurs due to the mode-mode interactions in the beam. When a mode is driven, the DCB stretches as the clamping points are fixed. This stretching (i.e. axial strain) is balanced by an increase in the axial tension of the beam exerted by the clamps. For small amplitude oscillations, this additional tension can be neglected. But when the beam oscillates with large vibrations, this axial tension plays a significant role in the dynamics of the beam.

For a single mode case, this extra tension is the basis of the Duffing nonlinearity and it changes the resonance frequency of that mode [8]. For the multimode case, excitation of one mode will change the resonance frequency of not only that mode but also the other modes as well, since the effective tension on the beam changes [39]. However, when we perform the experiments with PLL, the excitation amplitudes are kept constant and therefore the tension on the beam is kept more or less constant during the experiment. Thus we do not expect a first-order effect to occur in the context of mass sensing.

CHAPTER 4:

MULTIMODE EXPERIMENT

4.1 Introduction and Context

After we finished the single mode experiment, we shifted our attention to perform single-shot mass spectrometry experiments implementing the multimode technique described in the last chapter. We made several changes with respect to the previous experiment. These change relate to the transduction mechanism of NEMS, the types of proteins used and the the experimental setup.

First, we needed to be able to transduce the second mode of a doubly-clamped beam. Excitation of the second mode was not possible with the magnetomotive method, as the generated Lorentz force can only drive the odd-parity modes of the beam. Therefore, we switched to using **the thermoelastic-actuation / piezoresistive-detection method**. This method was developed in the Roukes group mainly by Igor Bargatin and Inna Kozinsky, and has succesfully transduced many modes of a doubly-clamped beam[40]. One drawback of this method is that the size of the beams had to be increased to accommodate for the u-shaped electrodes on the beam, which were not needed in the magnetomotive technique. Therefore the NEMS devices used in this experiment were heavier than the ones used in the single-mode experiment; and as a result they had worse mass resolution. Previously we obtained 10-kDa mass resolution with the magnetomotive transduction; in this experiment, however, we were limited to 100-kDa mass resolution.

Furthermore, at this resolution level (100-kDa), it is not possible to detect the protein species used in the single mode experiment. Therefore, we needed to try larger proteins in this experiment. These larger proteins posed new problems in terms of the creation of protein ions and their efficient transportation to NEMS. These problems are discussed in the last section of this chapter.

We also changed the large cryostat system with a more compact setup employing a flow-based cryostat. We describe this new setup, shown in Figure 26, in detail in the next section.

In this experiment, we first measured 10-nm gold nanoparticles (GNPs) which are detectable easily as they have mean nominal weight 6 MDa. However the mass dispersion of these nanoparticles is quite large; we do not expect to obtain a single peak for the mass value. After obtaining preliminary data with GNPs, we tried to electrospray large biomolecules, mainly a protein named IgM which has a molecular mass of 950 kDa. However we obtained very limited amount of data points so far. We will discuss the possible reasons for this shortcoming in the last section of this chapter.

4.2 Experimental Setup

The experiments were carried out on a table-top vacuum system and the NEMS chip was cooled by the cold finger of a flow cryostat. This setup is cheaper, more compact, and more accessible than the previous NEMS MS setup; and it brings us one step closer to our goal of implementing a practical mass spectrometer (Figure 26).

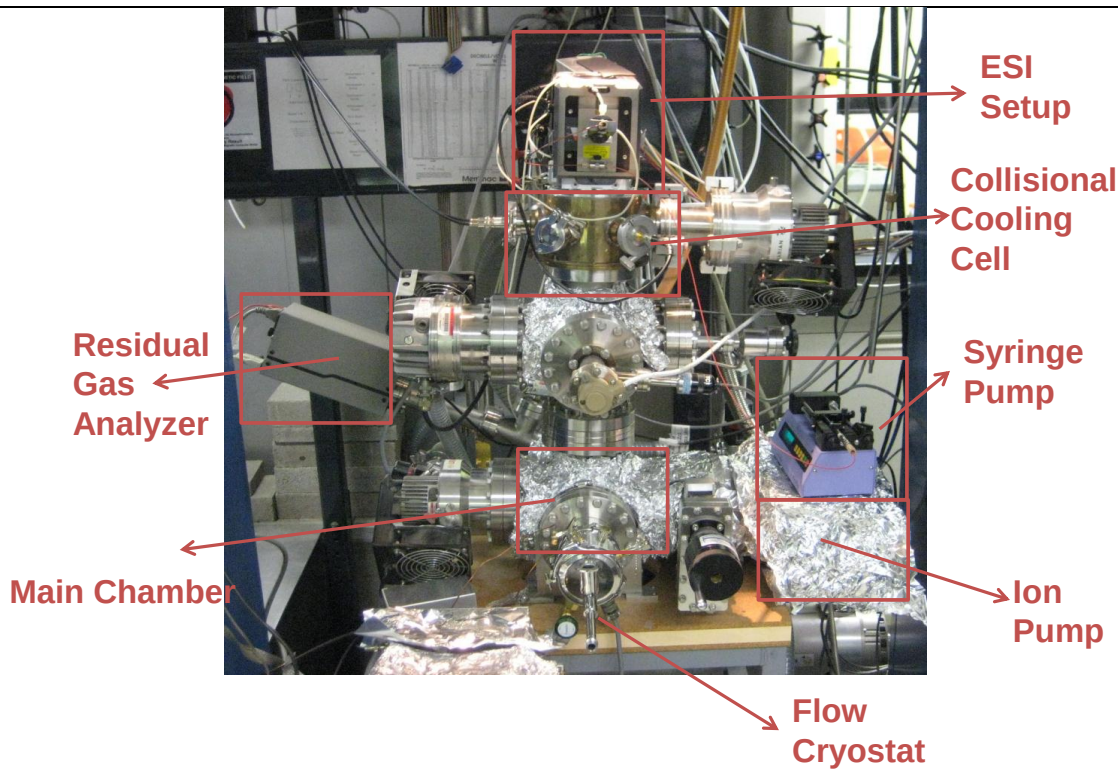

Figure 26: Picture of the Multimode Setup

This picture shows the 4Csetup, described below.
A syringe, filled with the protein solution, is secured to the *syringe pump*, an instrument which plunges the syringe at a set rate. The syringe is connected to the *Electrospray Ionization* (ESI) needle, via fluidic lines. ESI creates protein ions at atmospheric pressure. These ions are then directed into the chamber with free-jet expansion, a process accelerating the ions. These fast ions are slowed down in the *collisional cooling* cell. After this chamber, they are admitted into another chamber with lower pressure. This chamber contains a tilted hexapole, and non-aligned input and output apertures to break the line of sight for neutral ions from the atmosphere. Finally, the ions arrive at the *main chamber*, where the NEMS device is placed. The stage housing the NEMS is cooled down by the *flow cryostat*. The *residual gas analyzer* monitors the partial pressures in the main chamber, to help minimize the drift rate of the NEMS due to physiosorption.

In this experiment, we used two different configurations of the vacuum system. The first configuration was used to detect the heavier species, i.e. 10 nm gold nanoparticles. This setup will be called *the 3C setup,* and it consists of three differentially-pumped chambers, an electrospray ionization system and a hexapole ion guide (Figure 27a). The second configuration was a modified version of the 3C setup and is called *the 4C setup* (Figure 27b). This setup consists of four differentially-pumped chambers, an electrospray ionization system and a hexapole ion guide, partially tilted in one of the chambers. The 4C setup was used to detect the biomolecules.

We used two different configurations because there is a trade-off between how efficiently the ionic beam can be transported to the device and how stable the NEMS frequency is. The ions can be transported more efficiently using three chambers due to the shorter path; however the NEMS frequency drifts strongly due to adsorption of water molecules, as the main chamber is poorly isolated from the outside in terms of base pressure and gas influx. In this case, many background gas molecules will adsorb on the nems per unit time and bury any signal due to a biomolecule adsorption event. Therefore, we used this setup to detect gold nanoparticles as they are heavier.

The 4C setup has four differential vacuum chambers; hence the main chamber is isolated better thanks to the additional chamber. Furthermore, in this setup we broke the line-of-sight path from atmosphere to the NEMS device, by placing the final aperture off-center. We used a tilted hexapole to transport the ions in this tilted path (see Figure 27b). Thus the incoming neutral species most likely end up scattered within the third chamber, whereas ions are transported to the fourth chamber by the tilted hexapole.

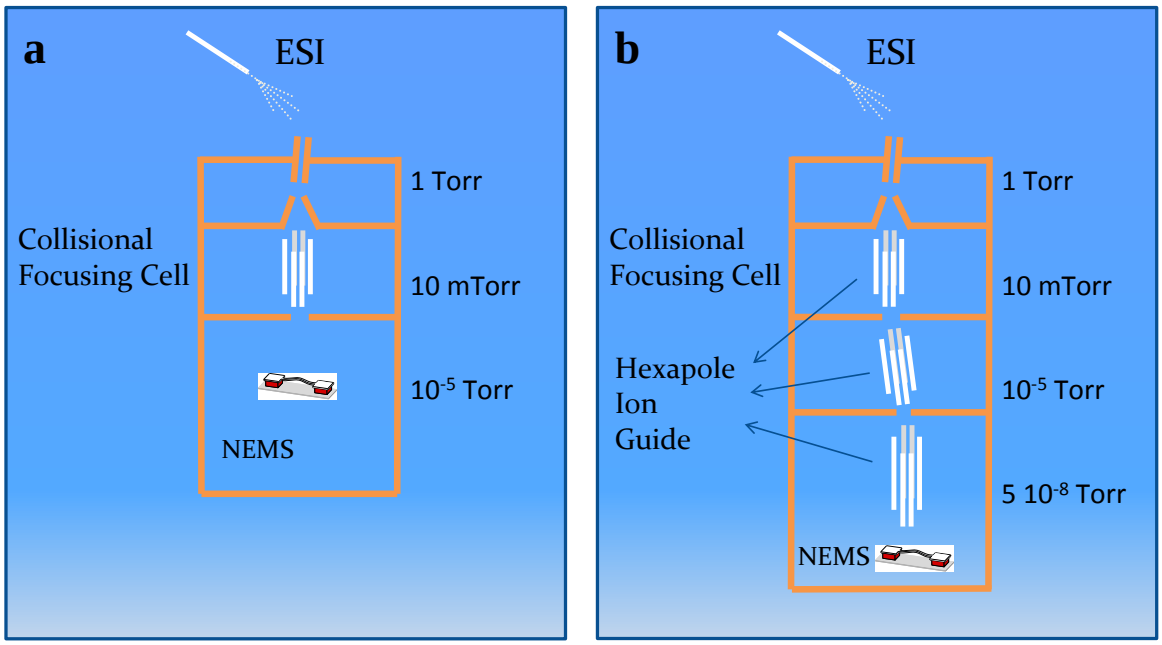

Figure 27: Setups for the Multimode MS Experiment

The pressures shown are room temperature values. When the cryostat is operated with liquid helium, the pressure drop an order of magnitude in the main chamber.

In **(a)** the three chamber setup (**3C Setup)** is depicted. There are only three vacuum stages: nozzle-skimmer stage to create the ionic beam, the collisional focusing setup to slow down and transport the ions and the main experimental chamber where the NEMS is placed. In **(b)** we have added one more chamber added between the collisional cooling chamber and the main chamber. This new chamber facilitates differential pumping so that the main chamber is at a much lower pressure. Furthermore, this chamber contains a tilted hexapole which breaks the line-of-sight path from atmosphere to the main chamber. To compensate for the added path, hexapolar ion guides are installed in this new chamber and the main chamber. This chamber is termed as four chamber setup, i.e. **4C Setup.**

In both setups, the species are ionized by electrospray ionization (ESI) as before. Typical ESI conditions can be found in Table 4 for the GNP and the IgM runs. These ions are transported into the first stage of vacuum system by hydrodynamic flow and electrostatic focusing. Near the entrance of the vacuum system, hot N_2 gas flows counter to the incoming material. This gas dries out the micro-droplets, enhancing Coulombic fissionm and sweeps away neutral molecules. Once entered, the particles travel through a long capillary toward the first stage of the vacuum chamber. At the end of the tube, the incoming gas expands into a low vacuum region and supersonically accelerated ions are sampled by a skimmer structure to obtain a collimated molecular/ionic beam [28]. The

larger particles in this molecular beam are slowed down in the second chamber (at 10 mTorr) through collisions with the background atoms. In the 3C setup, this decelerated beam is focused to the third chamber (main chamber). In the 4C setup, this beam passes through the third chamber that includes a tilted hexapole and an off-center aperture and arrives at the fourth chamber (main chamber).

Parameter	Description	Typical Value for 10-nm GNP runs	Typical Value for biomolecule runs
V_{needle}	Voltage on the electrospray needle	4.4-5.2 kV	4.4 – 5.2 kV
V_{shield}	Voltage on the ESI counter electrode	1 kV	1 kV
$V_{capillary}$	Voltage on the capillary	300V	150V-300V
f_{RF}	RF frequency of AC voltage applied to the hexapole	350 kHz	350 kHz
V_{RF}	Amplitude of the RF voltage applied to the hexapole	360V	360 V
P_{cc}	Pressure of the collisional cooling cell	10 mTorr	10 mTorr
T_{dry}	Temperature of the drying gas	180 ºC	80-120 ºC
P_{dry}	Pressure of the drying gas	30 psi	30 psi
P_{neb}	Pressure of the nebulizing gas	15 psi	15 psi
R	Flow rate of the ESI solution	4 μL/min	4 μL/min
V_{L4}	Voltage on the electrostatic lens after the collision chamber	-20 V	- 20V
$V_{top\text{-}hex}$	DC voltage offset of the collisional chamber hexapole	60V	2V
$V_{bottom\text{-}hex}$	DC voltage offset of the other hexapole(s)[§§]	-40V	-2V

Table 4: Typical parameters used in the multimode mass detection experiment.

4.3 NEMS Device: Fabrication and Transduction

We fabricated the NEMS resonators out of low-stress silicon nitride on a silicon wafer. We used gold for the transduction electrodes on the beam. Typical devices are 5μm long, 100 nm thick and 360 nm wide. The gold electrodes are 45 nm thick, and they are

[§§]For the advanced setup with three sets of hexapole, the two final sets of hexapole were kept at the same DC offset voltage.

U-shaped, with length 550 nm and width 100 nm. The fabrication of NEMS closely follows the paper by Igor Bargain and Inna Kozinsky [40].

To summarize, we started our fabrication process with 100 nm low-stress silicon nitride on silicon wafers, with silicon nitride as the structural material. We fabricated the gold electrodes symmetrically at the two edges of the NEMS beam using e-beam lithography and thermal evaporation. Later, we deposited SrF_2 as an etch mask, again using e-beam lithography and thermal evaporation. We suspended the devices using anisotropic and isotropic plasma etching. We removed the etch mask by dipping the chip into HCl for five seconds, followed by rinsing in H_2O (Figure 28).

We used the gold electrodes on the device to transduce mechanical motion. We used one electrode to drive the mechanical motion through the thermoelastic effect [40] .We measured the piezoresistive change of the other electrode to read out the mechanical motion. Previous work in our group usually employed a frequency down-mixing scheme to read out the resistance change of this electrode, due to the finite RC-bandwidth of the output channel [41]. Since we used gold electrodes with resistances around 50Ω, we realized that we could measure the AC signal change occurring on the electrode directly, without using frequency down mixing. The circuit diagram for the measurement setup is shown in figure Figure 29, with typical parameters in Table 5.

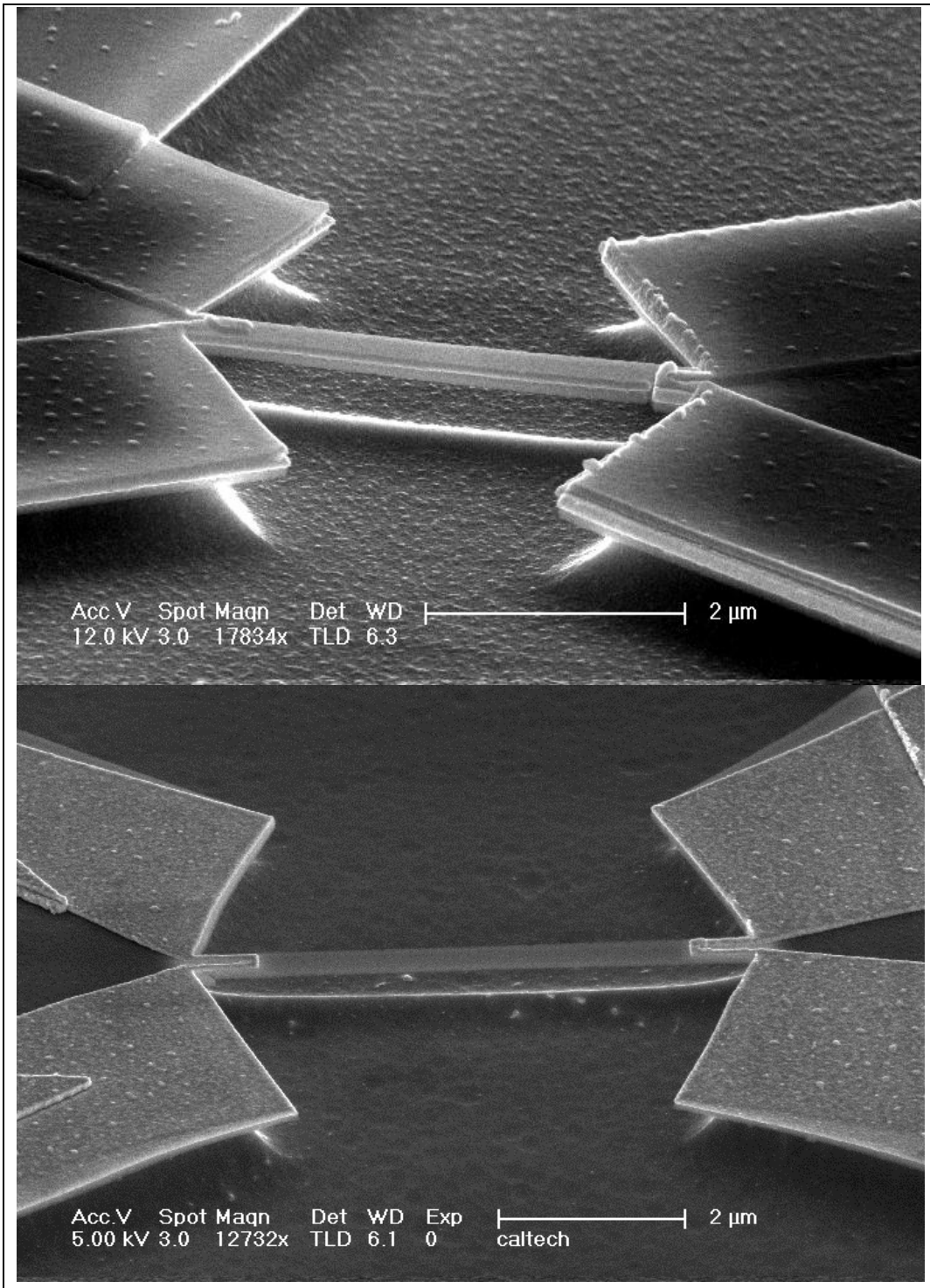

Figure 28: Images of NEMS Devices Used in Multimode Transduction

(a) NEMS device with the etch mask on. (b) Final structure. Here, we have a double-clamped beam with electrodes on both edges of the structure. The electrodes are identical, so that the symmetry of the structure is preserved. One of the electrodes is used to actuate the mechanical motion in the beam, through the thermo-elastic stress caused by the disproportional thermal expansion of the metal electrode with respect to the silicon-nitride beam underneath. The other electrode is used to read out the mechanical motion through the change in its piezo-resistance (i.e. it acts as a local stress-gauge).

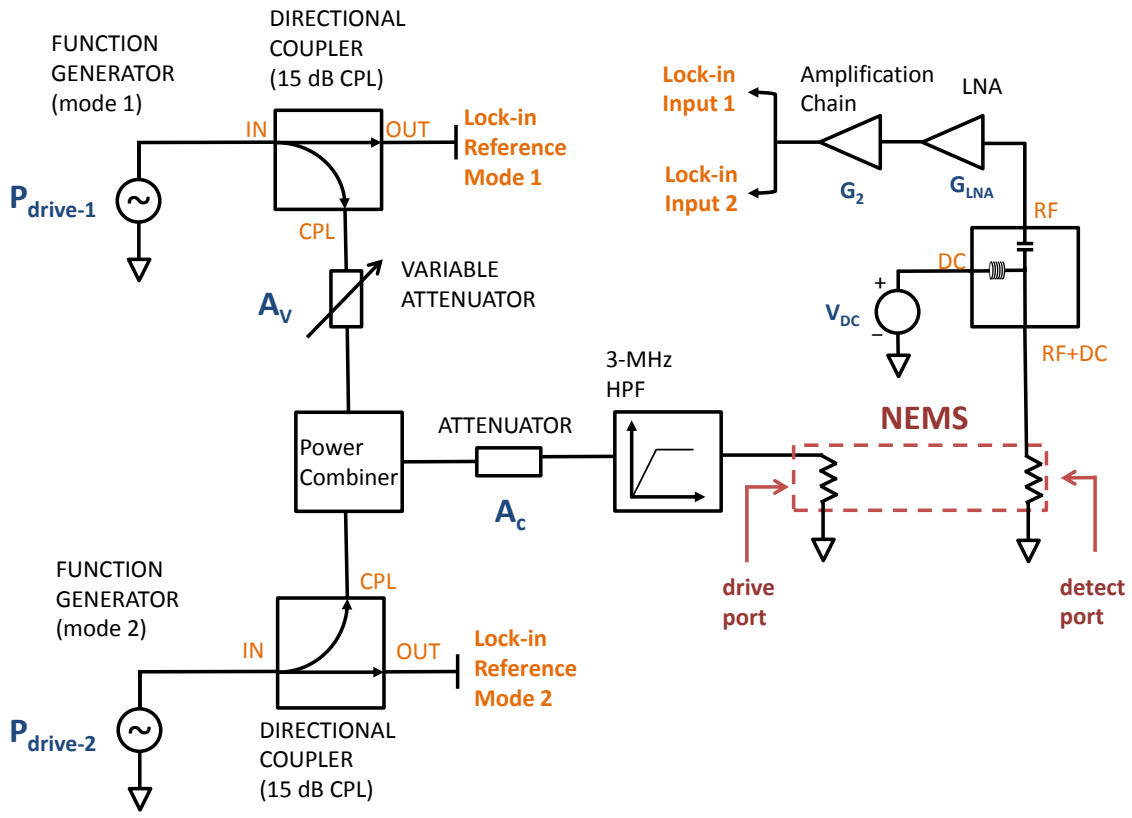

Figure 29: Circuit Diagram for Multimode Transduction

For the explanation of abbreviations and typical values used in the experiment, please refer to Table 5. Various filters are omitted in this diagram for the purpose of clarity. The lock-in amplifiers are operated in the *2f* mode.

Symbol	Description	Typical Value
$P_{drive-1}$	Amplitude of the function generator output driving mode 1	13 dBm
$P_{drive-2}$	Amplitude of the function generator output driving mode 2	13 dBm
A_v	Value of the variable attenuator, affecting mode 1	7 dB
A_c	Value of the attenuator, affecting both modes	17 dB
V_{DC}	DC voltage applied to bias the output electrode	50 mV
G_{LNA}	The gain of the first stage (i.e. that of the low-noise amplifier)	32 dB
G_2	The gain of the amplifiers between the LNA and lock-in input	28 dB

Table 5: Circuit Parameters for Multimode Mass Detection

The mechanical response of the two modes are shown in figure Figure 30.

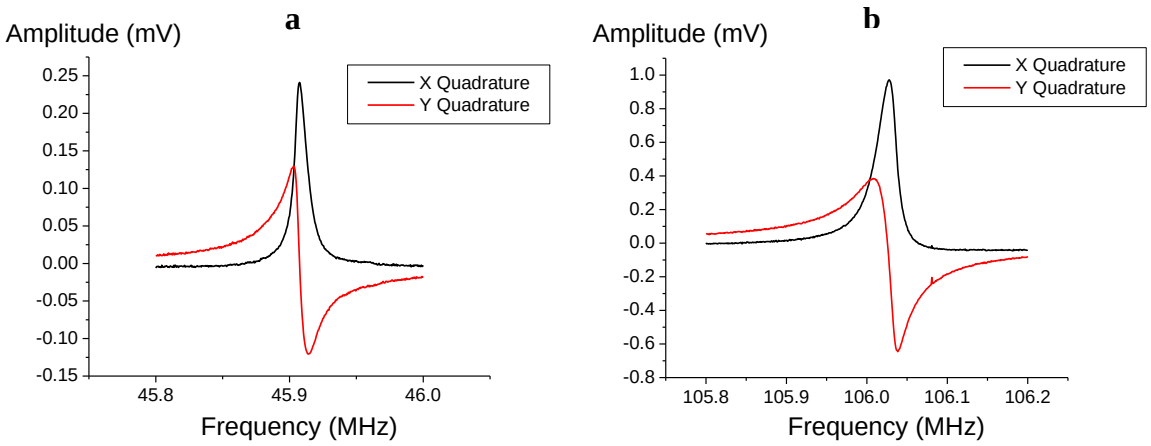

Figure 30 : Frequency sweep plots for the first and second modes.

These plots are recorded at low temperature. Please refer to APPENDIX D:.

4.4 Simultaneous Frequency Tracking of Two Modes

After constructing the two-mode transduction circuitry (Figure 29), we introduced a digital feedback loop into this circuitry to convert it to a phase-locked loop (PLL) and to track the frequencies in real time. First, we wanted to verify the proper operation of the two-mode PLL, before we attempted to detect the molecule landing events. Figure 31a shows one such test. In this case, we used a cantilever beam with the first mode at ~6MHz and the second mode at ~44MHz. In addition to the PLL circuitry, we included electronic elements so that we could apply a custom current pulse to the electrode of the

NEMS, thereby heating up the beam and changing the resonance frequencies of the modes being tracked. In Figure 31a, the red trace shows the three current pulses with different amplitudes applied to the device. In response to the current pulse, both PLLs respond in similar manner, thereby confirming the operation of the two-mode PLL circuitry. Figure 31b shows a close up view of one of the current pulse events. As shown, the first mode PLL responds a little faster than the second mode PLL. The response time of each of the PLL channels can be adjusted independently by adjusting the feedback gains and lock-in time constants.

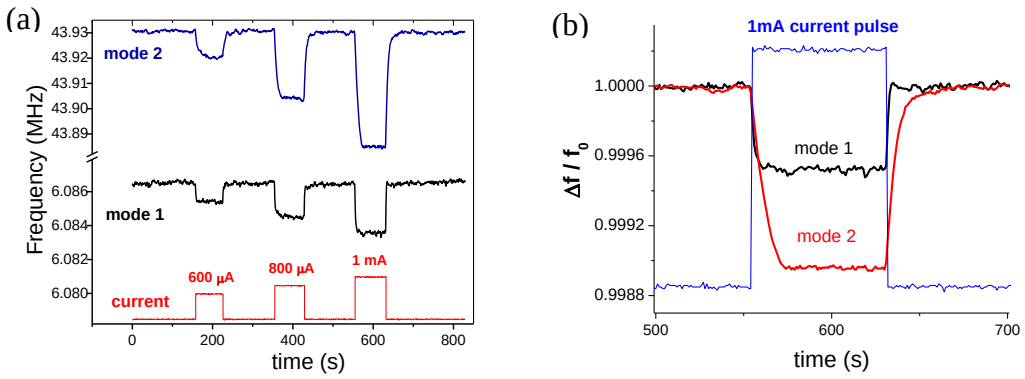

Figure 31: Two Mode PLL Response to Current Pulses

(a) Several current pulses and the response of the two modes.
(b) A closed up of one current pulse to show the temporal response of the two modes. The response of each mode can be adjusted separately by changing the relevant feedback parameters.

4.5 Discussion of Drift Rates, Remedies and Ion Transportation

After we assembled the basic setup (**3C**) shown in Figure 27a along with the measurement setup discussed in the previous section, we attempted to detect biomolecules. However, the NEMS frequency drifted down quickly at a rate of ~50Hz/s;

this drift rate prevented us from measureing any biomolecule landing events. In this configuration the main chamber is only the third chamber of the differential pumping chain and the pressure in this chamber is 10^{-5} Torr at room temperature and 10^{-6} Torr at low temperature. Thus the drift rates we obtained were reasonable, considering the large amount of water molecules desorbing from the chamber walls and adsorbing on the cooler NEMS per unit time. We tried to bake the chamber to lower the water load; but it did not help, as the flux from the second chamber (at 10 mTorr) was large enough that the water molecules on the main chamber constantly got refreshed. As a result we switched to the advanced setup shown in Figure 27b; the ultimate pressure of the main chamber decreased to mid-10^{-8} T at room temperature and mid-10^{-9} T at low temperature. After changing to the **4C** setup, the drift rate was about 3Hz/sec and we were able to measure the mass of the biomolecules[***].

Another aspect of the new design was to break the line of sight flux from the second chamber (at 10 mTorr) to the main chamber. We put a tilted hexapole in the third chamber, which delivers the ions slightly off axis to the final chamber. We checked the transportation of the ions to the main chamber using SIMION, an ion optics simulation program. Also we measured a significant amount of ionic current (~1 pA) reaching the bottom of the setup.

[***] The partial pressure of the water vapor contributes most to the material deposition at the temperatures at which we operate the system.

4.6 Results — 10 nm GNP and Biological Species

In this section we will present some of the data taken during the experimental runs. For the majority of our experimental runs, we tried to measure either the 10-nm GNP or IgM samples (IgM is a protein with MW of 950kDa). The event rates for both samples were quite sporadic; once in a while we would get data more frequently and other times we did not observe any discernable jump in frequency. We believe this inconsistency originates from the lack of feedback about the success of ESI and ion transportation processes, as we lacked an independent mass analyzer on the main chamber.

Figure 32 shows the two-mode PLL run during which we were electrospraying 10-nm gold nanoparticles with the 3C setup. Multiple jumps of different heights are evident. For clarity of presentation we have subtracted a constant drift (due to water adsorption) from the data. The PLL response times in this run were about 10 seconds for both modes. The Allan variance for the first mode was $3.0\,10^{-6}$ and for the second mode was $2.3\,10^{-6}$. The noise between the two modes had a correlation factor of 0.99.

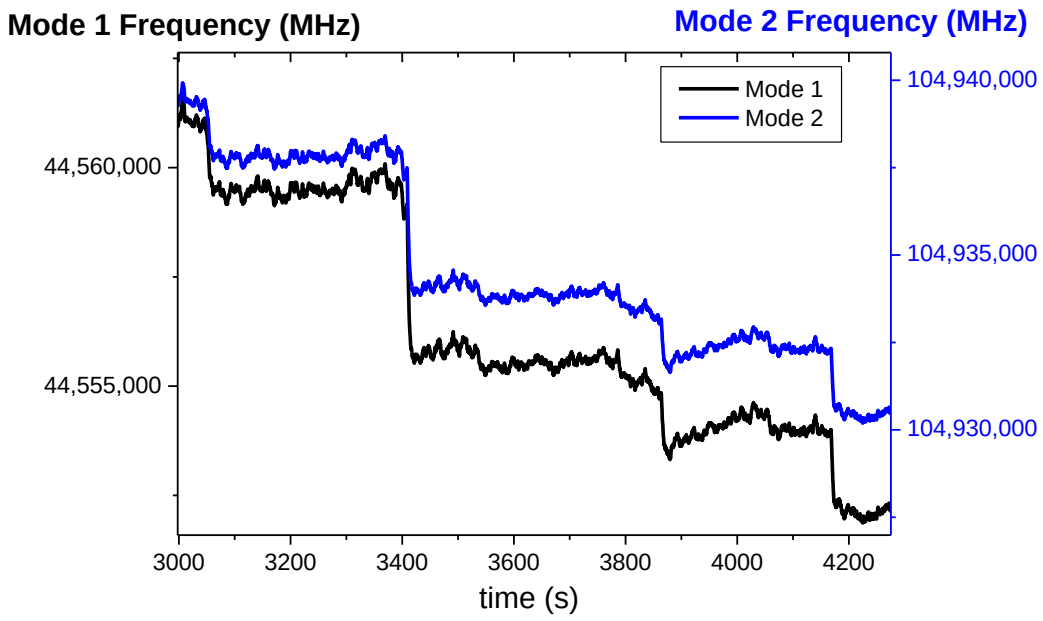

Figure 32: 10-nm GNP run

Figure 33 below shows the two-mode PLL run when we were spraying IgM, a 950-kDa protein, using the 4C setup. In this case the Allan variances were close to $3\ 10^{-7}$ for both of the modes, and the correlation coefficient between the modes was 0.90. We obtained only six frequency jump events with the IgM runs.

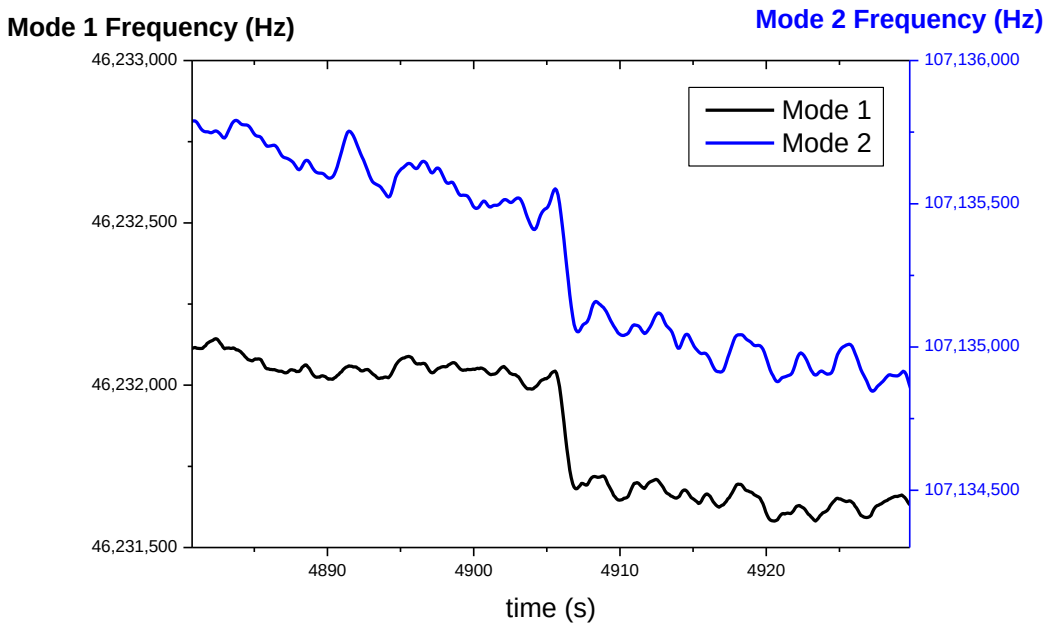

Figure 33: ESI run of IgM molecule

4.7 Data Analysis

Once we obtained the frequency jump data, we used the methods developed in the last chapter to analyze them.

We start by plotting these events in the frequency-frequency plane representation. In Figure 34, we show the 10-nm GNP events and the IgM events on the same plane. The GNP events are scattered along the plane, whereas four of the IgM events are condensed near the same mass contour. (This plot shows only a limited range of GNP events.)

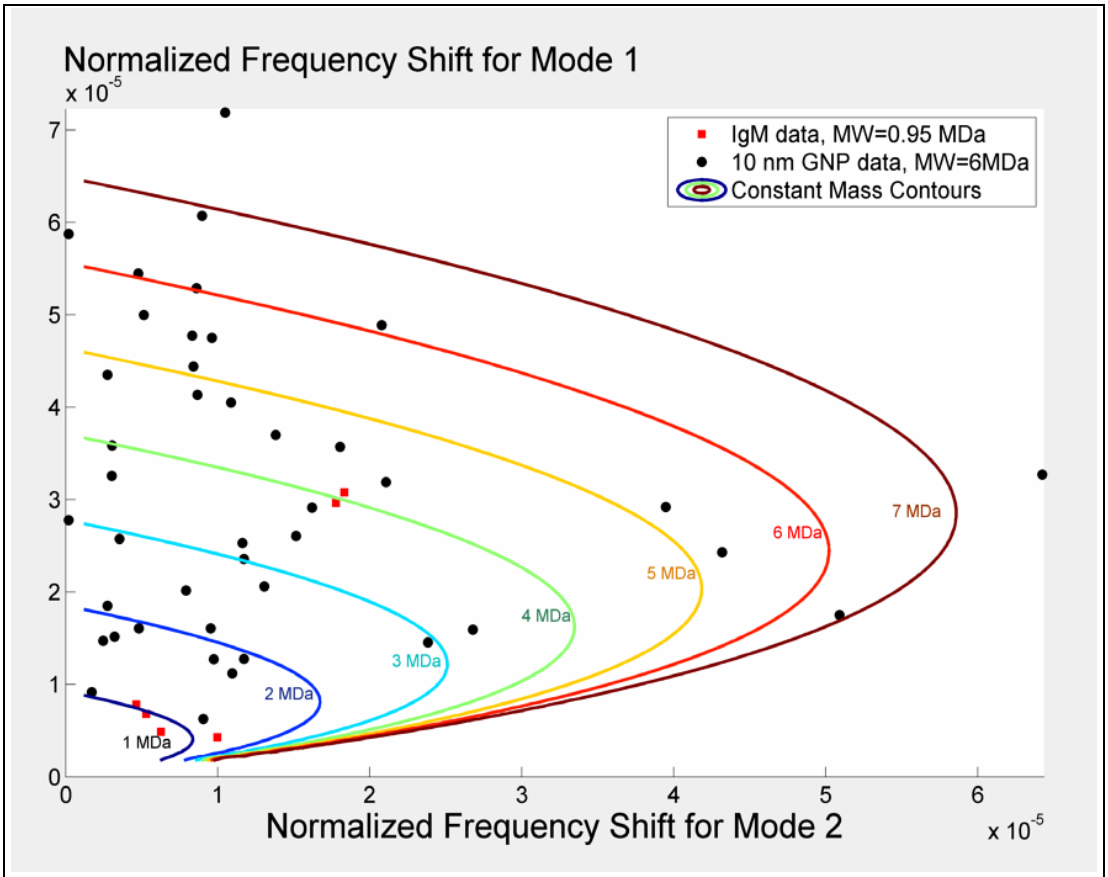

Figure 34: Frequency 1 - Frequency 2 Representation

In this plot, we represent each event as a point in a two-dimensional plane. The y-axis shows the amount of frequency shift for mode 1 and the x-axis shows the amount of frequency shift for mode 2. We also showed the constant-mass contours for clarity.

We can also visualize the data in the mass-position plane by converting the frequency jumpo information to mass-position information(along with the uncertainties). In Figure 35 we show the mass position plane representation for the 10-nm GNP events. In Figure 36 we show the mass-position representation for the IgM events. Once we have these representations, we can integrate along the position coordinate to determine the mass values (i.e. we project the 2-D PDFs onto the mass coordinate to obtain 1-D PDFs for the mass value).

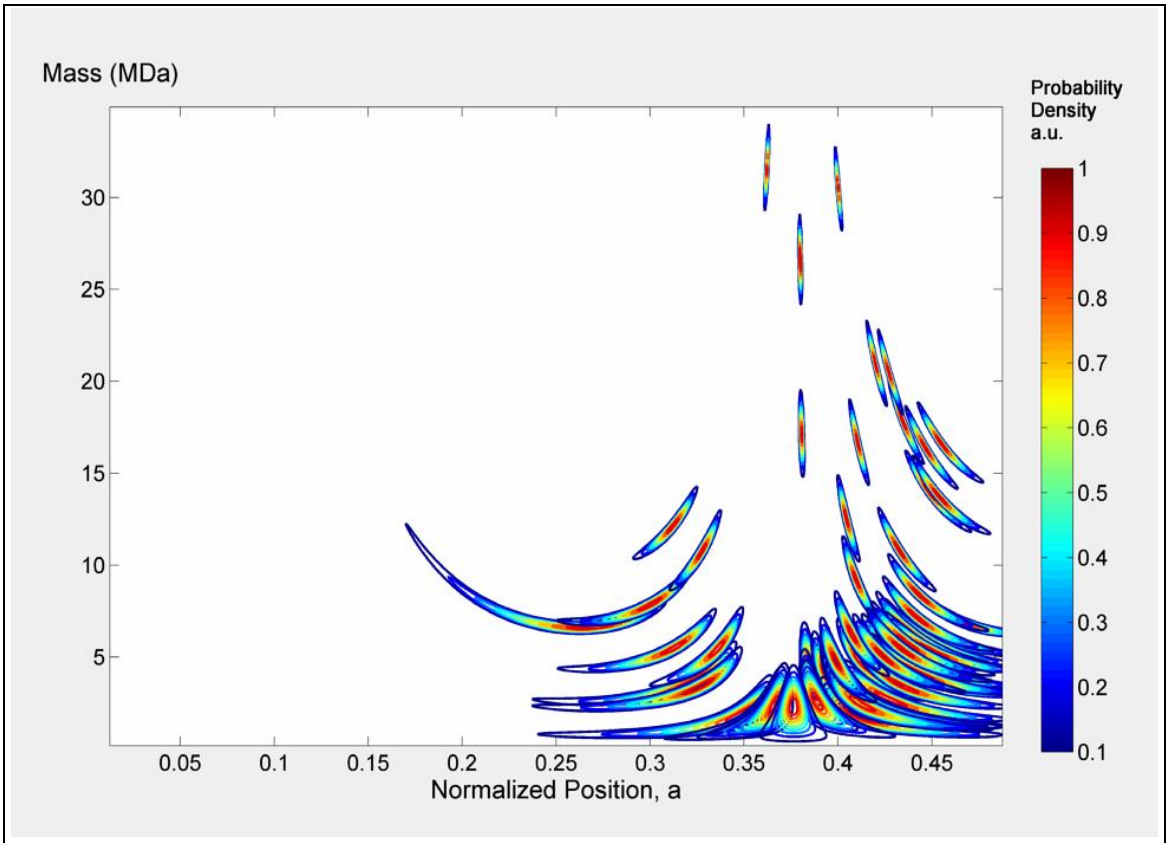

Figure 35: Mass – Position Representation for the 10-nm GNP events.

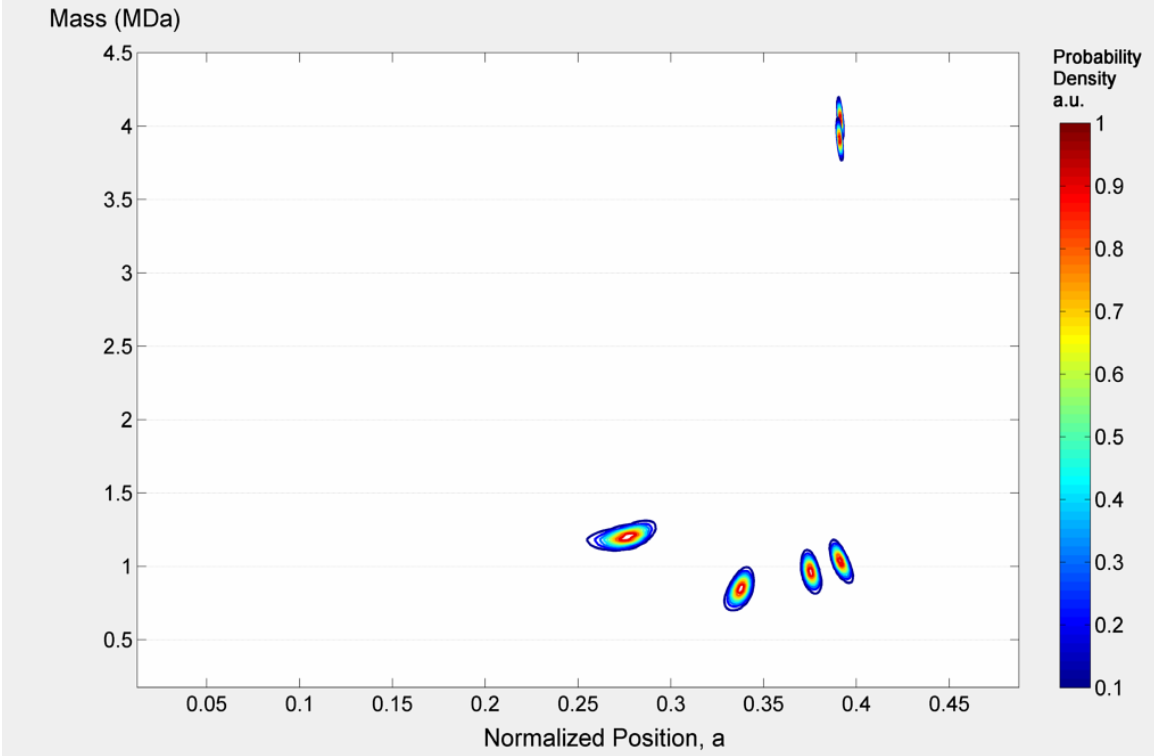

Figure 36: Mass-Position Representation for the IgM (MW=950kda) Events.

Once we have the above mass-position contours we can easily convert them into mass distributions as shown in figure Figure 37. The gold nanoparticle data seems to be compatible with a Gaussian distribution of mass, with a 20% radial dispersion. Although the nominal diameter of the GNPs is 10 nm, the actual value for the diameter seems to be smaller. For the IgM molecule, we have four data points accumulating near the 0.95 MDa region, monomeric mass of IgM. The remaining two jumps overlap at 4 MDa, suggesting the mass of a tetramer. The position distribution for the GNPs is shown in Figure 38 and is concentrated on the most sensitive region.

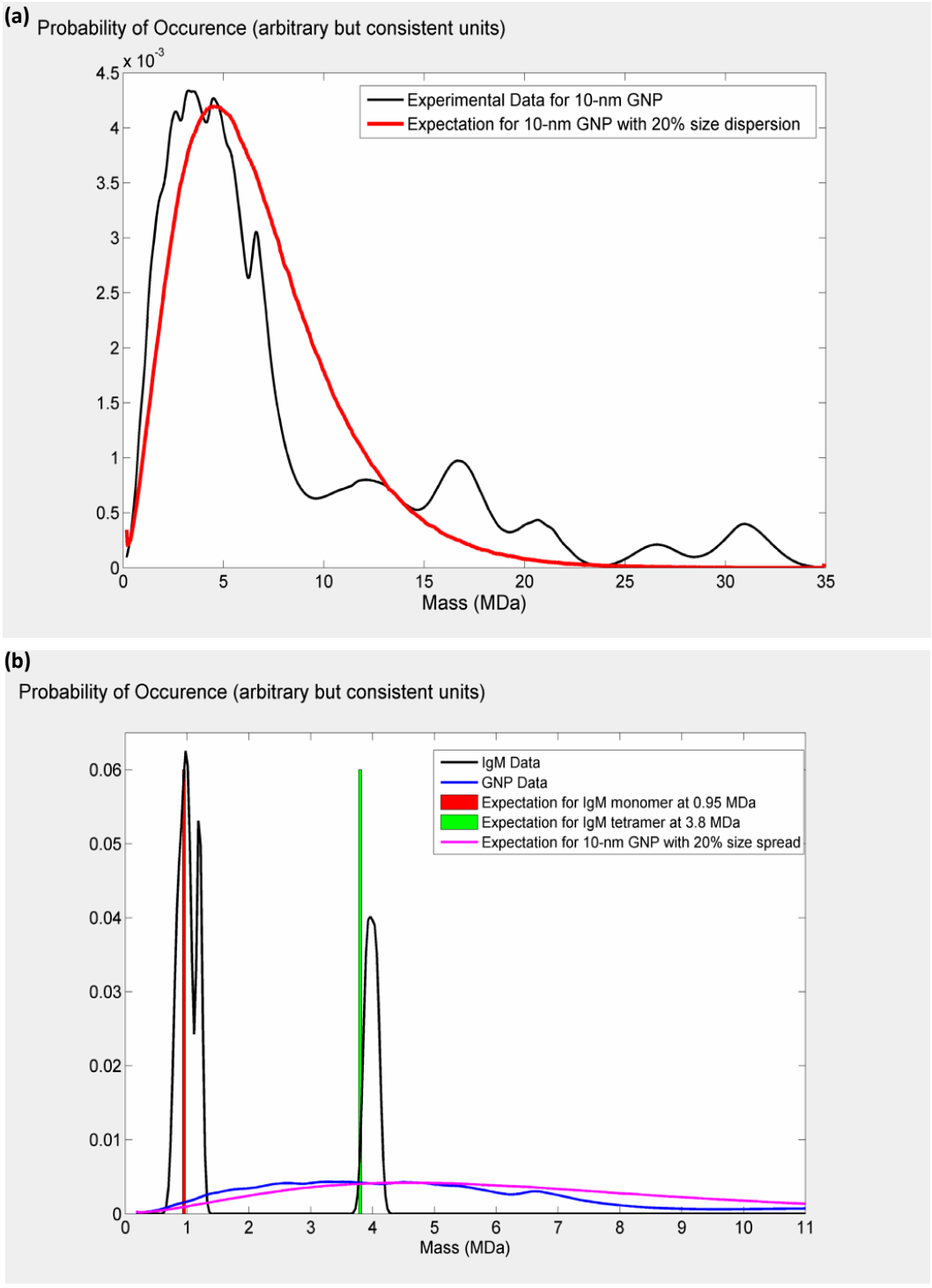

Figure 37: Mass Spectra of 10-nm GNP and IgM

(a) The mass distribution for 10-nm GNP events and theoretical expectations. Obtained distribution seems to be slightly smaller in mass, and equally disperse. The bumps beyond the tail of the expected curves are attributed to agglomerated nanoparticles, i.e. dimers, trimers etc. (b) The mass distribution for IgM events, alongside with the GNP distribution for reference.

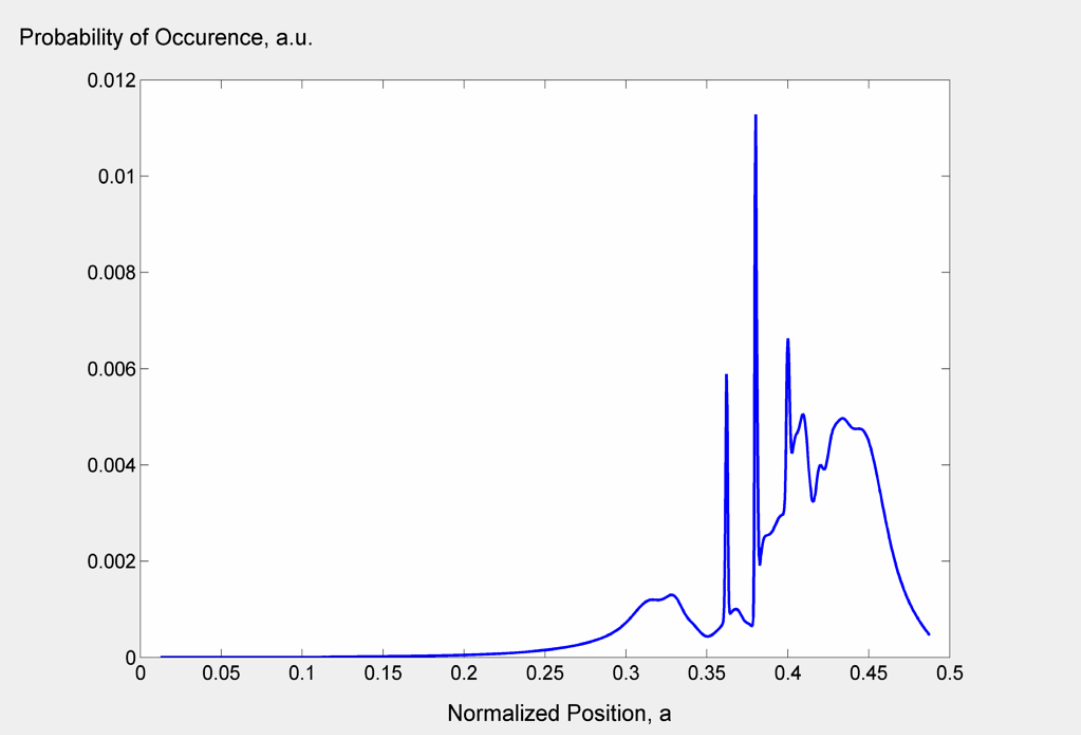

Figure 38: Position Distribution for 10-nm GNP Events

The spike-like features originate from the high-mass particles (GNP agglomerates) landing on the device and causing a strong signal which translates to a well resolved spatial coordinate. The position distribution vanishes near the edge as the sensitivity function is small as shown in 3.7.1 and in Figure 24. The vanishing of the position distribution near the center is attributed to the loss of sensitivity for the second mode at the center. After accounting for the sensitivities, there seems to be a slight bias toward the 0.40-0.45 range.

4.8 Discussion

The results presented so far have been compatible with the expected mass distributions of the species; however they do not provide strong evidence, as there have been only a few events collected with this technique, especially with the IgM molecule. In this section we will discuss the possible factors limiting the rate of event detection. Since we create the

ions by ESI and we refer to the ESI MS literature to prepare our solutions and adjust our ESI and ion optics conditions, the main focus of the discussion will be the ESI of the large proteins.

First few proteins are studied with ESI above 100 kDa and conventional mass spectrometry. The production and transportation of such large ions is not as robust as that for smaller proteins. Most papers in the ESI literature focuses on ionizing these large molecules under native conditions, i.e. under chemical conditions where the three-dimensional structure of the protein is conserved [42, 43]. The most common solution used for native mass spectrometry is ammonium acetate (NH_4Ac) solution in water, with concentrations in the range of 10-500 mM. This solution has pH≈7 and contains two volatile electrolytes, desirable properties for native state ESI. We used this ESI solution to capture proteins in the native state. However, the native state also requires reduced number of charges on the protein. As a result, these large proteins converts into ions with very high mass-to-charge ratios and they are difficult to transport with our existing setup.

One possible solution to this problem may be to acidify the solution, i.e. to move away from the mild conditions of native ESI and to use harsher conditions that place more charges on the proteins. There is not as much literature for the denaturing conditions for the ESI of large protein. Furthermore acidification may fragment the proteins into subunits since the large biomolecules are comprised of many pieces, relatively weakly bound to form the overall structure. Therefore we have not tried this path yet.

In summary the ESI and ion transportation conditions for these biomolecules must be finely tuned. In conventional mass spectrometry, these conditions are optimized by trial

and error, i.e. by monitoring the signal intensity in real time while adjusting the parameters to find a sweet spot of operation. However in our case, we lack an independent detector that would give us instantaneous feedback about the amount and nature of the species created by ESI and transported by the hexapolar ion guide. We can measure the ionic current reaching the end of the system, where our device is situated; however, we do not have a means of determining the composition of this ionic current. Installing an independent mass spectrometer, like a Time-of-Flight analyzer would have complicated the instrumentation further; however, in hindsight, this might have been a better way to approach the problem, as the biggest uncertainty in the experiment is the nature of the ions reaching the main chamber.

CHAPTER 5:

CONCLUDING REMARKS

5.1 Introduction

The projects we attempted so far have been early steps toward a more sophisticated and encompassing goal of creating a truly nanoscale instrument. As mentioned in the previous chapters, the mass resolution of the NEMS MS is still four-to-five orders of magnitude away from the desired single Dalton levels. The capture rates of the NEMS devices are impractically low. The setups housing the NEMS devices are still large and expensive. The NEMS devices need to be cooled down by cryostats and controlled by expensive and bulky electronics. All these concerns should be answered satisfactorily in a successful system.

To address these broad challenges, our research group has been attacking these problems at several fronts. In this chapter we will briefly describe the various efforts in our research group at the moment to give a better perspective about the state of the research. Later, we will describe the envisioned NEMS based mass spectrometry system, as an extrapolation of these efforts. Finally, we will compare the various performance parameters that conventional mass spectrometry has and the NEMS based mass spectrometry needs to have.

5.2 Current Efforts to Improve NEMS-Based Mass Spectrometry

As mentioned in chapter 4, we do not have enough data to establish a strong case for the multimode experiment yet. Dr. Akshay Naik is working on the ESI system to debug this project at the moment by reevaluating the ion transportation system and employing non-native MS conditions.

Poor mass resolution is one of the biggest challenges we are facing at the moment. The phase noise values (i.e. frequency instability) of NEMS devices are larger than the expected values based on theoretical calculations. To resolve the mismatch between the observations and the expectations, Dr. Sébastian Hentz and Dr. Guillermo Villanueva are working to determine the factors limiting the frequency stability.

Another solution to the mass resolution problem -circumventing the phase noise issue altogether- is to use smaller, lighter resonators. In this context, graphene seems to be an ideal material to be used as a mechanical resonator, not only because it is a light material, but also because it can be grown robustly by chemical vapor deposition (CVD) [44]. Controlled growth of graphene by CVD is important as it enables systematic and repeatable fabrication of nanoscale devices, a prerequisite for fabricating multiplexed and complex nanosystems en masse. Peter Hung in our group has been engaged in graphene research and I am also interested in working on graphene for future nanomechanical systems.

In terms of ion transportation efficiency, an experiment, which employs MALDI rather than ESI for the production of protein ions, is underway by Scott Kelber and Dr. Akshay

Naik. The event rates observed in this experiment so far are very promising, as the sample plate containing the proteins can be placed in vacuum and positioned very close to the NEMS chip. The results so far suggest that MALDI may be a more suitable technique to couple with NEMS for the delivery of proteins. More information can be found in Appendix B for comparison of these two techniques.

Another way to increase the event rate for protein detection is to fabricate and control many such NEMS devices in parallel. This kind of large scale integration uses the chip area more efficiently and opens up the way for truly complex systems of NEMS. To this end, our group has been collaborating with LETI (France) under the framework, *the Alliance for Nanosystems VLSI*, to fabricate NEMS devices on wafer scale [45].

Within this collaborative effort, arrays of NEMS devices are being investigated in the context of mass spectrometry by Eric Colinet. He recently showed the simultaneous PLL operation of four NEMS devices, using a compact electronic measurement system specifically designed for the transduction of NEMS devices.

To sum up, several efforts are under way to push the limitations on several fronts, like the mass resolution, protein capture rate and array operation. The insights obtained from these investigations should bring us closer to the ultimate NEMS MS system.

5.3 The Ultimate NEMS-MS System

The ultimate system we envision, as a long term goal, is a table-top instrument that can accept a complex liquid sample and analyze its contents in twenty minutes. This system should encompass a microfluidic front-end with preprocessing and chromatography

functionalities, a novel mechanism to convert the species in the liquid phase into gas phase molecules, and an array of NEMS integrated on-chip with its control electronics.

On the sample delivery side, we want to interface our NEMS MS technique with a microfluidics preprocessing chip. The vision is that, a single cell will be admitted to the microfluidic channel and lysed; its contents filtered, optionally digested and passed through an on-chip liquid chromatography column and finally delivered to the NEMS devices by an on-chip ESI or MALDI mechanism.

The most problematic part in the technique is to get rid of the neutral molecules landing on the nems, while retaining a high ionic flux. As discussed, there is a loose trade-off between the efficiency of ion transportation and the elimination of the neutrals. Increasing the distance between the liquid/gel samples and the NEMS devices improves the elimination of the neutrals, but at the same time degrades the transportation of proteins. One important question is how we can build an on-chip system to deliver proteins within the chip without having the device overwhelmed by neutrals. This issue should be the ultimate limiting factor for the miniaturization of the NEMS MS technique.

One development that may increase the throughput and sample capture efficiency is to use densely-packed NEMS arrays. For a NEMS array to work, the electronic control system should be able to independently address and measure each of the NEMS resonators within the array. The most straightforward way to do this is to fabricate a low-noise amplifier just next to a NEMS resonator on the same chip. Then an interface circuitry should collect the frequency jump data from each of these devices and send this information to an outside computer which translates the frequency shift information into

molecular masses. This molecular mass information then can be used to identify proteins through a molecular mass library.

5.4 Advantages and Disadvantages of NEMS-based Mass Spectrometry

Mass resolution. Mass resolution in current implementations of MS is typically defined as the ratio of the mass/charge (m/z) value and the width of the mass peaks at half maxima. The best mass resolution is obtained with Fourier transform mass spectrometry (FTMS) systems, which attain mass resolutions of the order of 2,000,000 with typical measurement times of about a second. The resolution in FTMS is high at low m/z, but deteriorates with higher m/z. Unlike the current MS systems, which measure the mass-to-charge ratio, NEMS devices measure the mass of the molecule directly. Achieving a mass sensitivity of 1 Da with a NEMS device will provide the ability to distinguish two species differing by a single Da. For a 1 kDa molecule, this would be equivalent to a mass resolution of 1,000; however, NEMS–MS is capable of measuring molecules greatly exceeding 1 MDa, which means state-of-the-art mass resolution is attainable. With longer measurement times the mass sensitivity can be further enhanced.

The upper limit of the mass sensitivity is set by noise sources such as 1/f fluctuations and long-term drifts, which always become predominant at long measurement times. The state-of-the- art of mass sensing with NEMS devices has been improving roughly by about an order of magnitude per year for the last several years; the current record is approaching 100 Da [19] (using Carbon nanotubes).The ultimate limits imposed by thermodynamically driven fluctuation processes have also been theoretically established

to be comfortably below 1 Da [15] for measurement times in the ten millisecond range. However, more works need to be done to verify this prediction is indeed attainable.

Mass accuracy. Mass accuracy is the ability of the instrument to accurately establish the absolute m/z (mass in NEMS–MS) of the species and is usually expressed in parts per million. A NEMS device with single dalton mass sensitivity, calibrated with an appropriate mass standard, will have a mass accuracy of 100 ppm for a 10 kDa molecule. In NEMS–MS the accuracy increases in direct proportion to the mass of the analyte molecule.

Mass or m/z range. NEMS devices have an exceptionally large mass dynamic range. These devices can easily measure biomolecules with masses of tens of MDa and still be sensitive enough to detect mass changes of a single dalton. The upper limit on the mass is set by the mass of the NEMS device itself. Depending upon the details of adsorption, the properties of the NEMS become affected only when the mass accreted becomes comparable to that of the device itself.

This translates into an upper-mass limit of hundreds of MDa for typical devices. The lower mass limit in the case of detection of large biomolecules may ultimately become limited by the spatial extent of the molecule compared to that of the NEMS sensor.

Scan speed. NEMS devices, in principle, are capable of mass sensitivities of a single dalton for measurement (integration) times in the tens of milliseconds range. Additionally, in future NEMS–MS systems, species of all m/z or masses will be measured simultaneously using arrays of NEMS devices.

Efficiency of protein transport from the source to the NEMS detector. NEMS–MS system combines the role of analyzer and detector into a single unit. This enables a significant reduction in the distance between the protein source and the detector, and thus a corresponding improvement in the efficiency of transport and capture. In the so-called nanoESI–MS systems, for instance, efficiencies as high as 10% have been observed [46]. Loss of analyte molecules arises from a combination of factors such as incomplete desolvation, transmission losses through the ion optics and detection inefficiency. We anticipate that future NEMS–MS systems will be based upon arrays of NEMS devices to provide maximal capture efficiency.

Parallel processing of the mass information. In NEMS-based MS systems each NEMS device acts as an individual mass sensor. Here, the capture cross-sectional area has dimensions of approximately 100 nm x 1,000 nm. This small cross-section has implications for the parallel-processing abilities of such a system. In 100 s, a modest NEMS–MS system consisting of 1,000 devices could quantitatively process 1,000 x 100 molecules s^{-1} x 100 s = 10 million molecules. Integration densities that greatly exceed this have already been realized. This throughput should be sufficient for intensive analyses, for example, on individual mammalian cells.

Appendices

APPENDIX A: ESI vs. MALDI

In the past decades, one of the major achievements of chemistry has been the invention of techniques that can convert large molecules into gas phase without denaturing them. There are two techniques that are most widely used:

1) Electrospray Ionization (**ESI**)
2) Matrix-Assisted Laser Desorption Ionization (**MALDI**)

Briefly, in ESI the liquid solution containing the protein solution is flown through a narrow needle and a high voltage is applied to this needle (with respect to a counter electrode). As a result, a spray plume of protein solution consisting of micron-scale charged droplets are formed. These droplets contain charged solvent and protein molecules. As the droplets travel in the air, the solvent evaporates, shrinking the droplets. As the droplets shrink, the charge-to-volume ratio increases and this eventually leads to the fission of the droplet. This cycle repeats itself for the product droplets. Eventually, through a mechanism not completely understood, individual protein molecules are released from the nano-size droplets. Notice that the process described so far needs to take place near atmospheric pressure, so that the solvent evaporation can place. Charged protein molecules and highly-charged, small droplets are admitted into the vacuum system at this point through electrostatic lensing, while the neutral solvent molecules and large droplets are swept away by a reverse-flowing gas.

In the other alternative, MALDI, the protein solution is mixed with another molecule generically named as matrix. The utility of this molecule is to absorb the laser light and transfer charge to the protein molecules. The protein-matrix mix is deposited on a metal

plate, then this plate is placed in a vacuum chamber. A laser pulse hits the metal plate and as a result matrix and protein molecules are desorbed from the surface.

For our experiment, both methods have pros and cons.

The pros of ESI are:

1) When we wanted to change the source conditions (like the protein, solvent, flow rate etc.), we were able to perform the changes quickly as the ESI source is situated at room pressure and temperature, as a separate entity. Whereas in MALDI, the plate is placed inside the vacuum system, and depending on the baking condition, changing the plate would take matter of days.
2) There is not any contamination due to the solvent or electrolytes in ESI, if the conditions are set properly. However in the case of MALDI, matrix molecules are inevitably created, and their deposition may interfere with the actual protein deposition.

The pros of MALDI is:

The MALDI source can be situated very close to the NEMS chip. Thus the molecules leaving the surface needs to travel only a few centimeters, and when the molecular beam arrives on the chip, it has not dispersed yet, i.e. the molecular density of the beam is large. Whereas in ESI case, the proteins molecules are created in atmospheric pressure. Whereas the NEMS works best at high-vacuum and low-temperature. As a result, use of ESI requires a differential pumping setup and ion transportation system. Inevitably, losses happen throughout the system.

As a result, the event rate, the number of protein molecules reaching nems per unit time, is larger for MALDI.

For various reasons ESI has been selected as the protocol to create the ions at atmospheric pressure. Then an RF ion guide and differential vacuum stage was designed by Wayne Hiebert to transport the ions to nems, being at held low temperature.

APPENDIX B: Bayesian Formalism for Frequency Jump Considerations

Notice when we wrote equation (56) above, we simply translated the frequency noise statistics by the amount of the measured frequency jump. We can justify this formally by using the inverse probability (Bayesian) theorem. We want to calculate the best estimate for the PDF of the *ideal frequency shift*, using the *measured frequency shift* and our knowledge about the noise statistics, and Bayesian theorem states that [37] :

$$PDF(f_{ideal} = f \mid f_{meas} = f')\, df = \frac{PDF(f_{meas} = f' \mid f_{ideal} = f) \times PDF(f_{ideal} = f) df}{\int PDF(f_{meas} = f' \mid f_{ideal} = f) \times PDF(f_{ideal} = f) df} \qquad (69)$$

Here ***PDF(condition 1 | condition 2)*** represents the probability density function of condition 1 **given** that condition 2 holds. So the left hand side of the equation reads: "Given that a frequency shift with the value of ***f'*** is measured, the probability that the ideal frequency shift had a value between ***f*** and ***f+df*** is equal to."

In mass spectrometry experiments, by definition we have no prior knowledge about the *actual frequency shifts* due to the analytes, as analytes can assume any value with equal probability. Hence the associated probability density function, $PDF(f_{actual} = f)$, is a uniform one. (That is $PDF(f_{actual} = f) = constant$). Hence, the $PDF(f_{actual} = f)$ term on the denominator, being a constant, gets out of the integral and cancels with the same term on the numerator. The remaining part of the denominator is simply 1, as it is the integral of a PDF over all possible values:

$$PDF(f_{ideal} = f \mid f_{meas} = f')\, df = \frac{PDF(f_{meas} = f' \mid f_{ideal} = f) \times PDF(f_{ideal} = f) df}{\int PDF(f_{meas} = f' \mid f_{ideal} = f) \times PDF(f_{ideal} = f) df} \qquad (70)$$

$$PDF(f_{ideal} = f \mid f_{meas} = f')\, df = \frac{PDF(f_{meas} = f' \mid f_{ideal} = f) \times PDF(f_{ideal} = f) df}{PDF(f_{ideal} = f) \times \int PDF(f_{meas} = f' \mid f_{ideal} = f) df} \quad (71)$$

$$PDF(f_{ideal} = f \mid f_{meas} = f')\, df = \frac{PDF(f_{meas} = f' \mid f_{ideal} = f) \times \cancel{PDF(f_{ideal} = f)} df}{\cancel{PDF(f_{ideal} = f)} \times \underbrace{\int PDF(f_{meas} = f' \mid f_{ideal} = f) df}_{1}} \quad (72)$$

$$PDF(f_{ideal} = f \mid f_{meas} = f') = PDF(f_{meas} = f' \mid f_{ideal} = f) \quad (73)$$

Furthermore we know that $\Delta f_{measured} = \Delta f_{actual} + \tilde{f}_{noise}$ therefore it is easy to see that $PDF(f_{meas} = f' \mid f_{actual} = f) = PDF(f_{noise} = f' - f)$. With these simplifications we end up with:

$$PDF(f_{actual} = f \mid f_{meas} = f'')\, df = \frac{PDF(f_{noise} = f' - f) df}{\int PDF(f_{noise} = f' - f) df} = PDF(f_{noise} = f' - f) df \quad (74)$$

The term on the right hand side is shown graphically in figure 1b.

APPENDIX C: : Kinematical Effect When Two Modes Are Driven

Consider a particle landed on position a on the nanomechanical beam. The beam is driven in a superposition of two modes. The vertical coordinate of the particle at any point in time is going to be:

$$p(t) = \phi_1(a)q_1(t) + \phi_2(a)q_2(t) \tag{75}$$

The velocity of the particle is:

$$\dot{p}(t) = \phi_1(a)\dot{q}_1(t) + \phi_2(a)\dot{q}_2(t)$$

And the kinetic energy is:

$$T_{particle} = \frac{1}{2}\Delta \mathrm{m}\ \dot{\mathrm{p}}^2 = \frac{1}{2}\Delta \mathrm{m}\ (\phi_1(a)\dot{q}_1 + \phi_2(a)\dot{q}_2)^2$$

Meanwhile the dynamics of the beam, without the particle, are described simply by linear addition of the different modes, as the modes are orthogonal.

$$T_{beam} = \frac{1}{2}M_1\dot{q_1}^2 + \frac{1}{2}M_2\dot{q_2}^2$$

$$U_{beam} = \frac{1}{2}k_1q_1^2 + \frac{1}{2}k_2q_2^2$$

Where M_i denotes the effective mass of mode i , and k_i denotes the effective spring constant of mode i.Considering the beam-particle system, we have the kinetic energy:

$$T_{system} = T_{beam} + T_{particle} = \frac{1}{2}(M_1\dot{q_1}^2 + M_2\dot{q_2}^2) + \frac{1}{2}\Delta m\ (\phi_1(a)\dot{q}_1 + \phi_2(a)\dot{q}_2)^2$$

$$T_{system} = \frac{1}{2}(M_1 + \phi_1(a)^2\Delta m)\,\dot{q_1}^2 + \phi_1(a)\phi_2(a)\Delta m\,\dot{q_1}\dot{q_2} + \frac{1}{2}(M_2 + \phi_2(a)^2\Delta m)\dot{q_2}^2$$

and $U_{system} = U_{beam} = \frac{1}{2}k_1q_1^2 + \frac{1}{2}k_2q_2^2$

Writing the Euler-Lagrange equations for this system, $\mathcal{L} = T - U$ and $\frac{d}{dt}\frac{\partial \mathcal{L}}{\partial \dot{q}_i} - \frac{\partial \mathcal{L}}{\partial q_i} = 0$, we have the following equations for the system:

$$(M_1 + \phi_1(a)^2\,\Delta\mathrm{m})\,\ddot{\mathrm{q}}_1 + \phi_1(\mathrm{a})\phi_2(\mathrm{a})\Delta\mathrm{m}\,\ddot{\mathrm{q}}_2 + \mathrm{k}_1\mathrm{q}_1 = 0$$

$$(M_2 + \phi_2(a)^2\,\Delta\mathrm{m})\,\ddot{\mathrm{q}}_2 + \phi_1(\mathrm{a})\phi_2(\mathrm{a})\Delta\mathrm{m}\,\ddot{\mathrm{q}}_1 + \mathrm{k}_2\mathrm{q}_2 = 0$$

If we did not have the mixing terms ($\phi_1(a)\phi_2(a)\Delta m\,\ddot{q}_i$) then we would have obtained the single-mode values for the frequency shift.

Define $N_1 \equiv (M_1 + \phi_1(a)^2\Delta m)$, $N_2 \equiv (M_2 + \phi_2(a)^2\Delta m)$, $\gamma = \phi_1(a)\phi_2(a)\Delta\mathrm{m}$. These new variables have the dimension of mass: $N_1, N_2 \sim M_{nems}$ and $\gamma \sim \Delta m$. Notice that $\gamma \ll N_1, N_2$. The parameter $\frac{\gamma}{N_i}$ will act as a smallness parameter in the following analysis. The frequency shift due to mass loading, in the single mode case is on the order of $\frac{\gamma}{N_i} \sim \frac{\Delta m}{M_{nems}}$.

With these variables, the equation system turns into the following form:

$$N_1\ddot{\mathrm{q}}_1 + \gamma\,\ddot{\mathrm{q}}_2 + \mathrm{k}_1\mathrm{q}_1 = 0$$

$$\mathrm{N}_2\,\ddot{\mathrm{q}}_2 + \gamma\,\ddot{\mathrm{q}}_1 + \mathrm{k}_2\mathrm{q}_2 = 0$$

From the top equation we have, $\ddot{q}_2 = -\frac{N_1\ddot{q}_1+k_1q_1}{\gamma}$ and $\dddot{q}_2 = -\frac{N_1\dddot{q}_1+k_1\ddot{q}_1}{\gamma}$. Taking the derivative of the bottom equation twice we have:

$$\mathrm{N}_2\,\ddddot{\mathrm{q}}_2 + \gamma\,\ddddot{\mathrm{q}}_1 + \mathrm{k}_2\ddot{\mathrm{q}}_2 = 0$$

Now replacing the expressions for $\ddot{q}$ and $\dddot{q}$ above:

$$-\frac{N_2N_1\dddot{q}_1 + N_2k_1\ddot{q}_1}{\gamma} + \gamma\,\ddddot{\mathrm{q}}_1 + -\frac{k_2N_1\ddot{q}_1 + k_2k_1q_1}{\gamma} = 0$$

Rearranging the terms:

$$(N_1N_2 - \gamma^2)\ddddot{\mathrm{q}}_1 + (k_1N_2 + k_2N_1)\ddot{\mathrm{q}}_1 + \mathrm{k}_1\mathrm{k}_2\mathrm{q}_1 = 0$$

Now trying a solution of the form $q = e^{\pm i\sqrt{\lambda}t}$ we have:

$$(N_1N_2 - \gamma^2)\lambda^2 - (k_1N_2 + k_2N_1)\lambda + \mathrm{k}_1\mathrm{k}_2 = 0$$

Define $\varpi_1 = \sqrt{\frac{k_1}{N_1}} = \sqrt{\frac{k_1}{M_1+\phi_1(a)^2\Delta m}}$ and $\varpi_2 = \sqrt{\frac{k_2}{N_2}} = \sqrt{\frac{k_2}{M_2+\phi_2(a)^2\Delta m}}$. <u>These are the frequency shifts obtained when a single mode is driven</u>. Notice that the frequency difference $\omega_{nems,1} - \varpi_1$ is on the order of $\frac{\gamma}{N_1} \sim \left(\frac{\Delta m}{M_{nems}}\right)$. Now divide the equation above by N_1N_2 and using the definitions of ϖ_1 and $\varpi_2$we obtain:

$$\left(1 - \frac{\gamma^2}{N_1N_2}\right)\lambda^2 - (\varpi_1^2 + \varpi_2^2)\lambda + \varpi_1^2\varpi_2^2 = 0$$

The solution of this quadratic equation is:

$$\lambda = \frac{(\varpi_1^2 + \varpi_2^2) \pm \sqrt{(\varpi_1^2 + \varpi_2^2)^2 - 4\varpi_1^2\varpi_2^2\left(1 - \frac{\gamma^2}{N_1N_2}\right)}}{2\left(1 - \frac{\gamma^2}{N_1N_2}\right)}$$

$$\lambda = \frac{(\varpi_1^2 + \varpi_2^2) \pm \sqrt{(\varpi_1^2 - \varpi_2^2)^2 + 4\varpi_1^2\varpi_2^2\frac{\gamma^2}{N_1N_2}}}{2\left(1 - \frac{\gamma^2}{N_1N_2}\right)}$$

$$\lambda = \frac{(\varpi_1^2 + \varpi_2^2) \pm (\varpi_1^2 - \varpi_2^2)\sqrt{1 + 4\frac{\varpi_1^2\varpi_2^2}{(\varpi_1^2 - \varpi_2^2)^2}\frac{\gamma^2}{N_1N_2}}}{2\left(1 - \frac{\gamma^2}{N_1N_2}\right)}$$

Now using the fact that $\gamma \ll N_1, N_2$ and for a DCB $\varpi_1^2\varpi_2^2$ is the same order of magnitude as $(\varpi_1^2 - \varpi_2^2)^2$ we can make a Taylor expansion of terms with γ:

$$\lambda = \frac{(\varpi_1^2 + \varpi_2^2) \pm (\varpi_1^2 - \varpi_2^2)\left(1 + 2\frac{\varpi_1^2\varpi_2^2}{(\varpi_1^2 - \varpi_2^2)^2}\frac{\gamma^2}{N_1N_2}\right)}{2}(1 + \frac{\gamma^2}{N_1N_2})$$

Picking up one of the solutions

$$\lambda_1 = \varpi_1^2 + \frac{\varpi_1^4}{\varpi_1^2 - \varpi_2^2}\frac{\gamma^2}{N_1N_2}$$

And the other solution is:

$$\lambda_2 = \varpi_2^2 + \frac{\varpi_2^4}{\varpi_2^2 - \varpi_1^2}\frac{\gamma^2}{N_1N_2}$$

As the solution has the form $q = e^{\pm i\sqrt{\lambda}t}$ we have all the four solution to the differential equation. The natural frequencies of these solutions are:

$$\omega_1 = \sqrt{\lambda_1} = \varpi_1 + \frac{1}{2}\frac{\varpi_1^3}{\varpi_1^2 - \varpi_2^2}\frac{\gamma^2}{N_1 N_2}$$

And

$$\omega_2 = \varpi_2 + \frac{1}{2}\frac{\varpi_2^3}{\varpi_2^2 - \varpi_1^2}\frac{\gamma^2}{N_1 N_2}$$

The frequency shift of mode 1 due to particle landing is:

$$\Delta\omega = \omega_{nems,1} - \omega_1 = \underbrace{\omega_{\mathrm{nems},1} - \varpi_1}_{\substack{order \sim \frac{\gamma}{N} \\ original\ shift \\ this\ happens\ during\ the \\ monotonic \\ drive\ of\ the\ mode}} + \underbrace{\frac{1}{2}\frac{\varpi_1^3}{\varpi_1^2 - \varpi_2^2}\frac{\gamma^2}{N_1 N_2}}_{\substack{order \sim \gamma^2/N^2 \\ correction\ to\ the\ shift \\ when\ two\ modes\ are \\ driven\ simultaneously}}$$

Simultaneous excitation has an effect on the frequency shift, but this effect is on the order of γ^2/N_1N_2 i.e. $\left(\frac{\Delta m}{M_{nems}}\right)^2$ whereas the original effect is on the order of γ/N_1 i.e. $\frac{\Delta m}{M_{nems}}$. Therefore, the correction to the frequency shift due to simultaneous drive of two modes is a negligible contribution and we have been safe to ignore it in the analysis.

APPENDIX D: : Background Reduction on Cooldown

Here we report the interesting observation that the electronic background level in the multimode transduction scheme suddenly decreases by an order of magnitude upon cooling the stage below 10K. Signal-to-background ratio is a practical figure of merit for NEMS devices, and it is important to know the origin of the background. This observation suggests that the background is caused by a leakage path on the chip. This path conducts the spurious second-harmonic ($at\ 2\omega_{drive} = \omega_{nems}$)at the NEMS input port to the NEMS output port. The 2ω spurious signal arises from the function generator and it gets amplified along with the $2\omega_{drive}$ signal arising from the mechanical response.

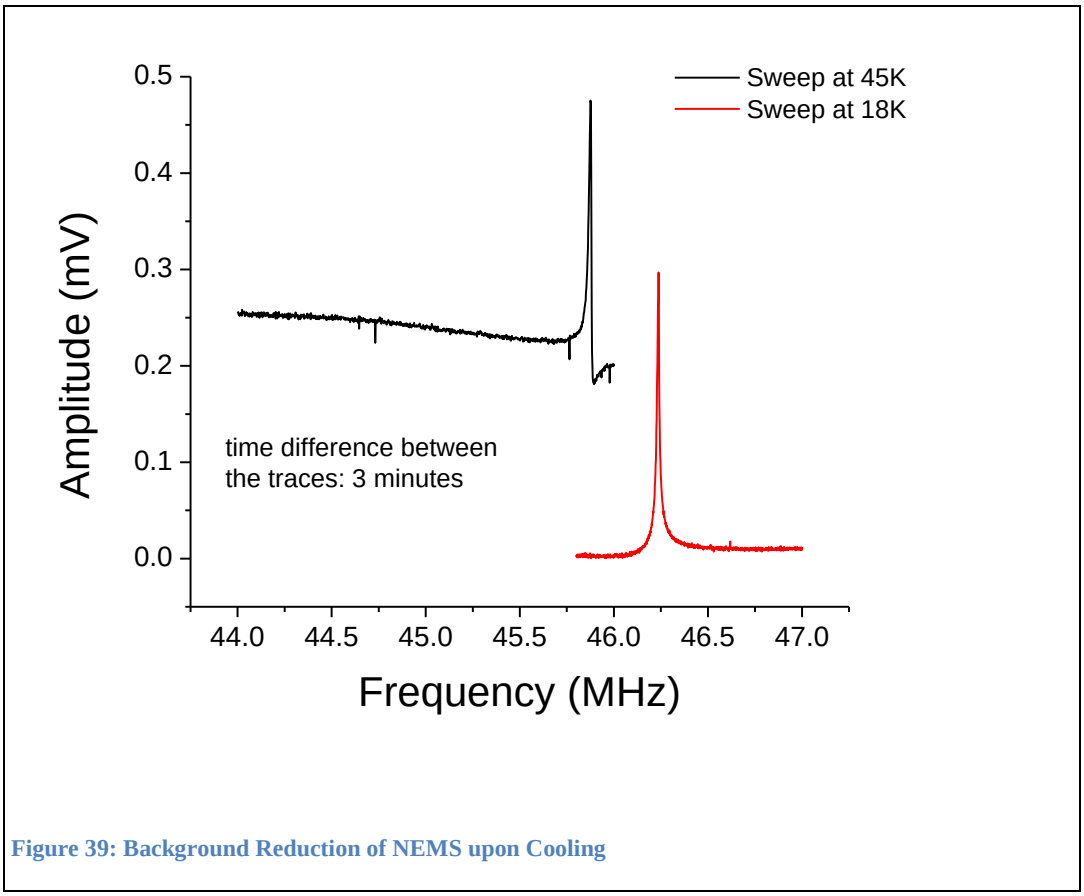

Figure 39: Background Reduction of NEMS upon Cooling

Bibliography

1. Mitchell, P., *In the pursuit of industrial proteomics.* Nat Biotech, 2003. **21**(3): p. 233-237.
2. Siuzdak, G., *The expanding role of mass spectrometry in biotechnology*. 2 ed. 2006, San Diego: MCC Press. 257.
3. *Scripps Center for Metabolomics and Mass Spectrometry Website*. Available from: http://masspec.scripps.edu/mshistory/whatisms_toc.php.
4. Cleland, A.N. and M.L. Roukes, *Fabrication of high frequency nanometer scale mechanical resonators from bulk Si crystals.* Applied Physics Letters, 1996. **69**(18): p. 2653-2655.
5. O'Connell, A.D., et al., *Quantum ground state and single-phonon control of a mechanical resonator.* Nature, 2010. **464**(7289): p. 697-703.
6. Naik, A., et al., *Cooling a nanomechanical resonator with quantum back-action.* Nature, 2006. **443**(7108): p. 193-196.
7. Karabalin, R.B., et al., *Signal Amplification by Sensitive Control of Bifurcation Topology.* Physical Review Letters, 2011. **106**(9): p. 094102.
8. Lifshitz, R. and M.C. Cross, *Nonlinear Dynamics of Nanomechanical and Micromechanical Resonators*. Reviews of Nonlinear Dynamics and Complexity. 2009: Wiley-VCH Verlag GmbH & Co. KGaA. 1-52.
9. Ekinci, K.L., X.M.H. Huang, and M.L. Roukes, *Ultrasensitive nanoelectromechanical mass detection.* Applied Physics Letters, 2004. **84**(22): p. 4469-4471.
10. Ilic, B., et al., *Attogram detection using nanoelectromechanical oscillators.* Journal of Applied Physics, 2004. **95**(7): p. 3694-3703.
11. Yang, Y.T., et al., *Zeptogram-Scale Nanomechanical Mass Sensing.* Nano Letters, 2006. **6**(4): p. 583-586.
12. Li, M., H.X. Tang, and M.L. Roukes, *Ultra-sensitive NEMS-based cantilevers for sensing, scanned probe and very high-frequency applications.* Nat Nano, 2007. **2**(2): p. 114-120.
13. Arlett, J.L., E.B. Myers, and M.L. Roukes, *Comparative advantages of mechanical biosensors.* Nat Nano, 2011. **6**(4): p. 203-215.
14. Cleland, A.N. and M.L. Roukes, *Noise processes in nanomechanical resonators.* Journal of Applied Physics, 2002. **92**(5): p. 2758-2769.
15. Ekinci, K.L., Y.T. Yang, and M.L. Roukes, *Ultimate limits to inertial mass sensing based upon nanoelectromechanical systems.* Journal of Applied Physics, 2004. **95**(5): p. 2682-2689.
16. Roukes, M.L., A. Naik, and M.S. Hanay, *Single Molecule Mass Spectroscopy Enabled By Nanoelectromechanical Systems*, U.S.P. Office, Editor. 2009.
17. Dohn, S., et al., *Mass and position determination of attached particles on cantilever based mass sensors.* Review of Scientific Instruments, 2007. **78**(10): p. 103303.
18. Chiu, H.-Y., et al., *Atomic-Scale Mass Sensing Using Carbon Nanotube Resonators.* Nano Letters, 2008. **8**(12): p. 4342-4346.
19. JensenK, K. Kim, and ZettlA, *An atomic-resolution nanomechanical mass sensor.* Nat Nano, 2008. **3**(9): p. 533-537.
20. Lassagne, B., et al., *Ultrasensitive Mass Sensing with a Nanotube Electromechanical Resonator.* Nano Letters, 2008. **8**(11): p. 3735-3738.

21. Karabacak, D.M., *Resonant Operation of Nanoelectromechanical Systems in Fluid Environments*, in *College of Engineering*. 2008, Boston University: Boston.
22. Cleland, A.N., *Foundations of nanomechanics*. 2002: Springer-Verlag.
23. Feng, X.L., *Ultra high frequency nanoelectromechanical systems with low noise technologies for single molecule mass sensing*. 2006, California Institute of Technology: Pasadena, CA.
24. Feng, X.L., et al., *A self-sustaining ultrahigh-frequency nanoelectromechanical oscillator.* Nat Nano, 2008. **3**(6): p. 342-346.
25. Dass, C., *Fundamentals of Contemporary Mass Spectrometry*. 2007: Wiley-Interscience.
26. Douglas, D.J. and J.B. French, *Collisional Focusing Effects in Radio Frequency Quadrupoles.* Journal of American Society for Mass Spectrometry, 1992. **3**: p. 398-408.
27. Chernushevich, I.V. and B.A. Thomson, *Collisional Cooling of Large Ions in Electrospray Mass Spectrometry.* Analytical Chemistry, 2004. **76**: p. 1754-1760.
28. Kantrowitz, A. and J. Grey, *A High Intensity Source for the Molecular Beam. Part I. Theoretical.* Review of Scientific Instruments, 1951. **22**(5): p. 328-332.
29. Whitehouse, C.M. and e. al., *Electrospray interface for liquid chromotographs and mass spectrometers.* Analytical Chemistry, 1985. **57**(3): p. 675-679.
30. Lebrilla, C.B., I.J. Amster, and R.T. McIver, *External ion source FTMS instrument for analysis of high mass ions.* International Journal of Mass Spectrometry and Ion Processes, 1989. **87**(1): p. R7-R13.
31. Mciver Jr., R.T., *Apparatus and method for injection of ions into an ion cyclotron resonance cell*. 1985: United States.
32. Ronald, M.J. and L.A. Scott, *Simplified radio-frequency generator for driving ion guides, traps, and other capacitive loads.* Review of Scientific Instruments, 2000. **71**(11): p. 4335-4337.
33. Ronald, M.J., G. Dieter, and L.A. Scott, *Simple radio-frequency power source for ion guides and ion traps.* Review of Scientific Instruments, 1997. **68**(9): p. 3357-3362.
34. Zorman, C.A., et al., *Epitaxial growth of 3C--SiC films on 4 in. diam (100) silicon wafers by atmospheric pressure chemical vapor deposition.* Journal of Applied Physics, 1995. **78**(8): p. 5136-5138.
35. Yang, Y.T., et al., *Monocrystalline silicon carbide nanoelectromechanical systems.* Applied Physics Letters, 2001. **78**(2): p. 162-164.
36. Allan, D.W., *Statistics of atomic frequency standards.* Proceedings of the IEEE, 1966. **54**(2): p. 221-230.
37. Roe, B.P., *Probability and statistics in experimental physics*. 1992, New York: Springer-Verlag. 208.
38. Casella, G. and R.L. Berger, *Statistical Inference*. 2 ed. 2001: Duxbury Press. 700.
39. Matheny, M.H., et al., *Strain transduced mechanics for the measurement of VHF nonlinear nanomechanical systems*, in *To be Published*. 2011.
40. Bargatin, I., I. Kozinsky, and M.L. Roukes, *Efficient electrothermal actuation of multiple modes of high-frequency nanoelectromechanical resonators.* Applied Physics Letters, 2007. **90**(9): p. 093116-3.
41. Bargatin, I., et al., *Sensitive detection of nanomechanical motion using piezoresistive signal downmixing.* Applied Physics Letters, 2005. **86**(13): p. 133109.
42. Uetrecht, C., et al., *Ion mobility mass spectrometry of proteins and protein assemblies.* Chemical Society Reviews, 2010. **39**(5): p. 1633-1655.
43. Heck, A.J.R., *Native mass spectrometry: a bridge between interactomics and structural biology.* Nat Meth, 2008. **5**(11): p. 927-933.
44. Li, X., et al., *Large-Area Synthesis of High-Quality and Uniform Graphene Films on Copper Foils.* Science, 2009. **324**(5932): p. 1312-1314.

45. *Website for the Alliance for Nanosystems VLSI*. Available from: http://www.nanovlsi.com/.
46. El-Faramawy, A., K.W.M. Siu, and B.A. Thomson, *Efficiency of nanoelectrospray ionization.* Journal of American Society for Mass Spectrometry, 2005. **16**: p. 1702-1707.